Non-linear Interactions in Single and Dual Component Bose Einstein Condensates

Patrick J. Everitt

A thesis submitted for the degree of **Doctor of Philosophy** of the Australian National University

March, 2020

Australian National University

Non-linear Interactions in Single and Dual Component Bose Einstein Condensates

Patrick J. Everitt

Department of Quantum Science,
Australian National University, Canberra, Australia.

Supervisory committee: Assoc. Prof. N. P. Robins
Prof. J. Close
Dr. S. S. Szigeti

Declaration

To the best of my knowledge and except where acknowledged in the customary manner, the material presented in this thesis is original and has not been submitted in whole or part for a degree in any university. Where work has been performed in collaboration with others, I have acknowledged the contributions of all authors.

Patrick Everitt _____

Date _____

Abstract

Non-linear systems give rise to a rich array of phenomena including chaos, turbulence, solitons, and dynamical instabilities. The great degree of experimental control over Bose Einstein condensates (BECs) makes them a unique tool to study these ubiquitous processes. Although single isotope BECs offer an ideal system for the study of simple non-linear physics, dual-component condensates allow the study of even richer coupled non-linear systems.

This thesis presents experimental results utilising a newly built dual-species ^{85}Rb/^{87}Rb BEC system where the precise manipulation of non-linear interactions is achieved through a Feshbach resonance. An overview of the experimental apparatus is given, with a focus on particular improvements and new features in comparison to previous designs. The BEC machine is capable of creating 2×10^5 and 2×10^6 condensates of ^{85}Rb and ^{87}Rb, respectively, as well as isotope mixtures, with a duty cycle of 13 s. The minimalist design of the apparatus, focusing on increased optical access combined with accurate control over the interaction parameters of ^{85}Rb, will open many avenues for future work.

Utilising the ^{85}Rb system, the behaviour of single component BECs in an optical waveguide is investigated. Focusing on the propagation of BECs with negative scattering lengths, we observe the formation of soliton trains. Using the nonpolynomial Schrodinger equation, it is shown that the formation of these trains can be understood as a manifestation of a modulational instability (MI). A non destructive imaging system, called shadowgraph imaging, allows multiple images of the stochastically forming soliton trains in a single run. Subsequently, we make the first real time observation of MI in a BEC.

Considering the full dual component ^{85}Rb and ^{87}Rb system, a wider variety of coupled non-linear phenomena can be investigated. Crucial to accessing applicable regimes is the reliable preparation of mixed groundstates in different configurations. We present a detailed experimental study of phase separated groundstates for the ^{85}Rb/^{87}Rb BEC

system. It is shown that sensitively tuning the energy scales of the system allows the creation of a wide variety of immiscible (non-mixed) groundstates to be created. We demonstrate control over the shape of the interface between immiscible condensates for a wide range of interaction parameters and isotopes ratios. This work lays a foundation for future dual-component instability studies.

Acknowledgements

I would like to acknowledge the Australian Government for their support in funding the majority of this research through the Australian Postgraduate Award and Australian Government Research Training Program.

The contents of this thesis could not possibly cover the breadth of experiences I have had over the course of this PhD. The constant support and encouragement of my supervisor Nick Robins allowed me freedom to work on and develop a familiarity with a wide range of ideas. Your attitude and approach to experimental physics is one I admire, and surprisingly often your mentor-ship ends up influencing my decision making.

To my good friend Carlos, thank you for introducing me to the BEC lab. Your tireless energy kept things going on many occasions, although it was also helped by the mate. Stuart, thank you for inexplicably helping another nearly finished PhD student polish off the remainder. I have learned many things from my fellow experimentalists: Gordon, Paul, Kyle, Sam, Chris, David; from "it's only temporary if it breaks" to "everything is easy", the lessons were always some combination of incredibly useful and hilariously useless. The wider research group including John, Craig, Joe, Johnny, Angela, Simon, Michael and more, have always been there to answer the easy and hard questions, let me win at table tennis, and tell me to just get it done. To the many fellow students I have shared my time with: Ciaron, Gordon, Jess, Kyle, Mahasen, Manju, Paul, Richard, Yosri,... and the list goes on; thanks for the life giving unmentionable chats.

To the events of 2020: bushfires, smoke, hail-storms and COVID-19; that'll do now, please stop.

My new colleague and house-mate Luke, thanks for the mutual understanding of the range of thesis writing emotions; I look forward to working with you for the next few months.

Alice, your belief in me as I worked towards the finish was of incalculable help. I hope this thesis contains enough adjectives.

To my parents, no one comes close to the amount of support you have given me at every stage of life. You've given me the tools to be where I am and want to be.

To everyone else, wash your hands.

Contents

List of Figures

List of Publications

The following publications are the result of research and collaborations undertaken during the course of this thesis:

[1] P. B. Wigley, K. S. Hardman, C. Freier, P. J. Everitt, S. Legge, P. Manju, J. D. Close, and N. P. Robins. *Readout-delay-free Bragg atom interferometry using overlapped spatial fringes*. Physical Review A **99**, 023615 (2019). DOI: 10.1103/PhysRevA.99.023615. [p 100]

[2] P. J. Everitt, M. A. Sooriyabandara, M. Guasoni, P. B. Wigley, C. H. Wei, G. D. McDonald, K. S. Hardman, P. Manju, J. D. Close, C. C. N. Kuhn, S. S. Szigeti, Y. S. Kivshar, and N. P. Robins. *Observation of a modulational instability in Bose-Einstein condensates*. Physical Review A **96**, 041601 (2017). DOI: 10.1103/PhysRevA.96.041601. [pp 4, 83, and 103]

[3] G. D. McDonald, C. C. N. Kuhn, K. S. Hardman, S. Bennetts, P. J. Everitt, P. A. Altin, J. E. Debs, J. D. Close, and N. P. Robins. *Erratum: Bright Solitonic Matter-Wave Interferometer [Phys. Rev. Lett. 113, 013002 (2014)]*. Physical Review Letters **118**, 219903 (2017). DOI: 10.1103/PhysRevLett.118.219903.

[4] P. B. Wigley, P. J. Everitt, K. S. Hardman, M. R. Hush, C. H. Wei, M. A. Sooriyabandara, P. Manju, J. D. Close, N. P. Robins, and C. C. N. Kuhn. *Non-destructive shadowgraph imaging of ultra-cold atoms*. Optics Letters **41**, 4795 (2016). ISSN 1539-4794. DOI: 10.1364/OL.41.004795. [pp 21, 45, 71, and 87]

[5] K. Hardman, P. Everitt, G. McDonald, P. Manju, P. Wigley, M. Sooriyabandara, C. Kuhn, J. Debs, J. Close, and N. Robins. *Simultaneous Precision Gravimetry and Magnetic Gradiometry with a Bose-Einstein Condensate: A High Precision, Quantum Sensor*. Physical Review Letters **117**, 138501 (2016). DOI: 10.1103/PhysRevLett.117.138501. [p 3]

[6] K. S. Hardman, P. B. Wigley, P. J. Everitt, P. Manju, C. C. N. Kuhn, and N. P. Robins. *Time-of-flight detection of ultra-cold atoms using resonant frequency modulation imaging*. Optics Letters **41**, 2505 (2016). ISSN 1539-4794. DOI: 10.1364/OL.41.002505.

[7] P. B. Wigley, P. J. Everitt, A. v. d. Hengel, J. W. Bastian, M. A. Sooriyabandara, G. D. McDonald, K. S. Hardman, C. D. Quinlivan, P. Manju, C. C. N. Kuhn, I. R. Petersen, A. N. Luiten, J. J. Hope, N. P. Robins, and M. R. Hush. *Fast machine-learning online*

optimization of ultra-cold-atom experiments. Scientific Reports **6**, 25890 (2016). ISSN 2045-2322. DOI: 10.1038/srep25890.

Chapter 1

Introduction

THE beautiful simplicity of linear systems, underpinned by the principle of superposition, is dethroned by one disruption: nature is non-linear. However, the disproportionate response of the over-excitable physical world in which we live is no inconvenience; rather it is a feature, producing a lavish array of behaviour to be perceived and comprehended. Even those restricted systems with linearity at their heart can exhibit non-linear phenomena, with complexity giving rise to non-linear equations of motion. The subject of this thesis, Bose-Einstein condensates, is one of the most fantastic manifestations of this. Formulated in the linear world of quantum mechanics, the assumption of a bulk description for the evolution of many individual atoms produces a non-linear dynamical system for a macroscopic quantum object.

The same dynamics which give rise to rich behaviour also create substantial mathematical difficulties. While the non-linear realm often submits to approximation and linearisation, it is exactly the cases where this approach fails which elicit seemingly unpredictable and counter-intuitive results; with an accompanying desire to understand them.

The foundation of non-linear theory began to be developed by Henri Poincaré in the late 1800s concerning the three body problem in celestial mechanics [1]. One of the first people to identify that deterministic systems could exhibit chaotic behaviour, his work was seminal in the creation of the now extensive chaos theory framework. Independently, Aleksandr Lyapunov developed a new framework for the study of the stability of non-linear dynamical systems, not reliant on a reductionist linearisation approach [2].

With continual advancement of computational infrastructure, numerical methods became a tractable approach to the study of non-linear systems. Notably, the work of meteorologist Edward Lorenz in atmospheric modelling showed that even simple systems could have limits on their predictability [3]. The sensitivity to initial conditions of a dynamical system became known as "the butterfly effect", a term now ubiquitous

enough to spawn a Hollywood film franchise [4]. The treatment of non-linear systems at a higher global level, often utilising statistical methods, led to the development of an array of new results in a breadth of areas such as fluid physics, materials science, particle physics, astrophysics, fibre optics and condensed matter physics.

Despite these new techniques, non-linear systems still remain some of the most difficult to study, with many open questions. These still fruitful areas are broad reaching, from the transition from laminar flow to turbulence in fluids [5], the emergence of chaos in quantum systems [6] and the behaviour of soliton like structures in dissipative systems [7]. Further afield in chemistry and biology, molecular simulation [8] and biochemical reactions [9], remain difficult with current methods. Even the mere existence of solutions to the Navier-Stokes equations, those that govern the flow of viscous fluids, is still an open question. Deemed so important, it is the subject of one of the Clay Mathematics Institute Millennium Problems attracting a one million dollar prize for its solution [10].

1.1 Bose-Einstein condensation

Bose-Einstein condensates (BECs) present a unique platform to investigate the nature of common non-linear processes. Their theoretical inception by Einstein in 1924 [11], following the work of Bose [12], brought about a fervour for an experimental observation of this new state of matter. Combining the de Broglie matter wave with particle statistics, the creation of such a state occurs when a Bose gas is cooled until a large fraction of atoms fall into the lowest quantum state. The critical temperature of this transition for dilute gases [13]:

$$T_c = 3.31 \frac{\hbar^2 n^{2/3}}{m k_B}, \tag{1.1}$$

where n is the particle density, k_B is the Boltzmann constant, and m is the atomic mass, is very near absolute zero. It would not be until significant new cooling and trapping techniques for neutral atoms were developed that the search would be satiated in 1995. First produced in a dilute gas of ^{87}Rb atoms cooled to 170 nK [14], the technological developments led to the awarding of two related Nobel prizes [15–17]. BEC production relies heavily on laser cooling, and the increasing availability of various laser wavelengths has made the cooling of a large number of atomic species possible. All alkali metals except radio-active Francium [14, 18–23], two alkali earth metals (^{40}Ca and ^{84}Sr) [24, 25], as well as ^{174}Yb [26], ^{52}Cr [27], ^{164}Dy [28], ^{168}Er [29], ^{1}H [30] and He* [31], have all been cooled to BEC.

More importantly, the field of BEC now contains a myriad of different applications. Having demonstrated macroscopic interference [32] and quantum superposition over 0.5 m [33], BECs have been proposed as a mechanism to test wavefunction collapse [34]. They have also been used to investigate quantum tunnelling and reflection [35–38], with the possibility to create the matter wave equivalent of Fabry-Perot cavities [39]. With BECs recently demonstrated in microgravity [40], their ability to make high precision inertial measurements [41, 42] has prompted great interest in future tests of the weak equivalent principle [43], quantum gravity [44], and gravitational wave detection [45].

The governing equations behind the behaviour of BECs, combined with the highly configurable nature of experimental BEC apparatus, give them the ability to mimic the behaviour of often inaccessible or unmeasurable dynamics, making them a unique tool to create analogue systems. Proposed BEC models include gravitational effects such as relativity and wormholes [46–48], quantum gravity [49, 50] and have even led to the first experimental observation of analogue Hawking radiation [51]. The potential for quantum simulations of many body states to be simulated on timescales much faster than current numerical methods [52] is of great interest to condensed matter physics and is an exciting future area of research.

1.2 Atom interactions and the non-linear Schrödinger equation

The interactions due to atomic scattering in a BEC manifest themselves as a non-linear term in the dynamical equation, forming the well known non-linear Schrödinger equation (NLSE). Given in its simplest 1D form:

$$i\frac{\partial\psi}{\partial t} = -\frac{1}{2}\frac{\partial^2\psi}{\partial x^2} + \kappa|\psi|^2\psi, \tag{1.2}$$

with the non-linearity parameter κ, the NLSE describes the evolution of many systems including fibre optics, plasma oscillations, water waves and ionosphere waveguides [53–56]. The associated non-linear phenomena of the NLSE are global in nature, with exotic objects such as solitons, breathers, rogue waves, shock waves, chaos and instabilities existing across a range of systems [57–65]. BECs possess several unique aspects that make them ideal candidates for the study of these. Firstly, unlike fibre systems where the non-linearity parameter is fixed, both the strength and sign of the non-linearity can be dynamically altered in a BEC through a magnetic Feshbach resonance [23]. Secondly, highly configurable confinement can be applied with relative ease. Finally, non-destructive imaging methods make real time observation of dynamical processes possible, giving the ability to study stochastic events.

Bose-Einstein condensates have thus far been used to observe bright and dark solitons as well as their excited breathing states [66–69], several dynamical instabilities including modulational instability (work presented in Chapter 5) [70–72], shock waves [73] and the onset of turbulence [74–76].

Two-component mixtures of condensates, comprised of coupled NLSEs, offer an even richer system and there has been significant recent interest in a wide variety of coupled non-linear phenomena: quantum turbulence and superflow [77–80], capillary instabilities [81], dark soliton decay [82], the onset of quantum chaos [83] and skyrmion collisions [84]. These experiments require accurate control of the initial ground state condition and the boundary between components, a prime motivating factor of the work presented in Chapter 6.

1.3 Outline of this thesis

This thesis is written with a focus on experimental work in the creation of an entirely new dual-species ^{85}Rb/^{87}Rb BEC apparatus and the use of atom interactions to investigate non-linear effects. The following chapters of this thesis are divided into three parts:

Part I: "The theory of light and atoms" presents an introduction to the background material necessary for experimental work in the following two parts. Chapter 2 introduces the two level atom and builds relevant concepts for the control, trapping and imaging of atom ensembles. Chapter 3 introduces the theoretical BEC with a focus on the tools necessary to control atom-atom interactions and create exotic non-linear processes.

Part II: "Making a Dual-Species Bose-Einstein Condensate" details the experimental work comprising the creation of the dual-species ^{85}Rb and ^{87}Rb apparatus. This unique machine was purpose designed to be highly configurable and act as an indispensable test bed for future experiments in dual component condensates, non-linear stability, optically guided atoms, and non-destructive observation of quantum tunnelling. The chapter presents a detailed experimental view of the improvements, difficulties and subtleties of this particular apparatus compared to previous works. This part is concluded with an outlook on the versatility and future of the machine.

Part III: "Controlling Atom Interactions" presents experimental results utilising the control of atom interactions present in the dual-species ^{85}Rb/^{87}Rb system. Chapter 5

presents the first real time observation of the non-linear process known as modulational instability in a BEC. Utilising a new non-destructive imaging technique, called shadowgraph imaging, we demonstrate that the breakup of soliton-like BECs in an optical waveguide into several spatial components can be understood in the framework of the nonpolynomial Schrödinger equation (NPSE). The statistics of the stochastic nature of this system are used to show that the underlying mechanism is modulational instability. Chapter 6 presents a detailed experimental study of phase separated groundstates in a ^{85}Rb /^{87}Rb mixture. We demonstrate the ability to reliably produce a range of groundstate configurations by controlling the intraspecies scattering length of ^{85}Rb, together with the isotope ratio. The curvature of the phase boundary between isotopes is shown to be a good categorisation of these states, with good agreement to accompanying numerical simulations. The dependence of this new measure on the scattering length and isotope ratios is shown to obey a power law which does not agree with simple energetic comparisons. This chapter concludes with an outlook of how these reproducible and well categorised groundstates enable experimental access to a range of theoretical results.

The thesis concludes in Chapter 7 with a summary of the presented work, and an outlook for the future directions of research.

Part I

The Theory of Light and Atoms

Chapter 2

Atom Light Interactions

Atom-light interactions provide a high degree of control over atomic ensembles. This chapter presents a brief introduction to atom-light interactions through the simple model of a two-level atom interacting with a classical light field. From this model the optical Bloch equations are generated, including the affects of spontaneous emission. We then use this model to elucidate concepts related to the trapping of ultra-cold atoms, focusing on the optical dipole force generated inside Gaussian and non-diffracting Bessel laser beams. The same equations are then used to develop the framework needed to image these trapped and cooled clouds, including a non-destructive shadowgraph imaging technique used subsequently in Chapter 5. Finally, the effects of external magnetic fields on atomic spectra are discussed, a feature used to precisely calibrate magnetic fields applied to the atoms in later chapters.

2.1 Two-level atom

The predominant use of alkali metals in BEC physics comes as no surprise; having only a single valence electron in the outer shell gives rise to a relatively simple level structure. With almost closed optical cycles they are well modelled by a simple two-level atom, with a small number of necessary repumping lasers treated as a technical detail. The coupling of this two-level atom to a radiative field is the foundation for the experimental detail behind optical cooling, trapping and imaging. The ubiquitous nature of this system has resulted in a plethora of detailed texts, with some of the writers' favourites given for the interested reader [85, 86].

2.1.1 Semi-Classical Approach

For most applications to ultra-cold atoms the radiative driving field is strong in comparison to its depletion by the atomic field. The semi-classical approach treats the radiative field as a classical wave, with the atom treated quantum mechanically.

We treat the two-level atom as having two eigenstates $|g\rangle$ and $|e\rangle$ (ground and excited

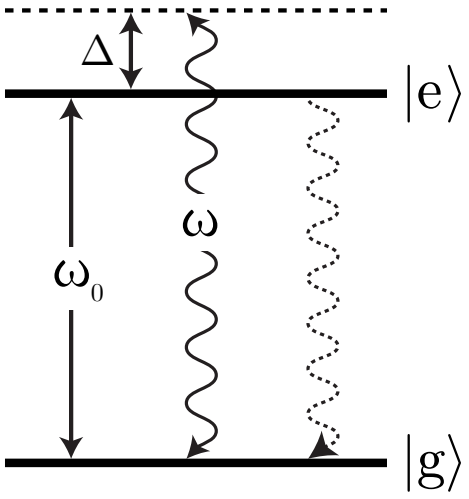

Figure 2.1: Level diagram of a two level atom with resonance ω_0, coupling to a radiative driving field of frequency ω with detuning Δ. Also shown is the spontaneous decay pathway from $|e\rangle$ to $|g\rangle$.

states, respectively), with the level separation equal to $\hbar\omega_0$ as in Figure 2.1. The atomic Hamiltonian is:

$$\hat{H}_{atom} = \frac{1}{2}\omega_0\hbar\left(|e\rangle\langle e| - |g\rangle\langle g|\right). \tag{2.1}$$

The radiative driving field, detuned Δ from the atomic resonance, is given by:

$$\mathbf{E}(t) = \mathbf{E}_0\cos\left(\omega t + \phi\right), \tag{2.2}$$

where $\omega = \omega_0 + \Delta$ and $\mathbf{E_0}$ is the amplitude vector of the field. The interaction Hamiltonian is given by:

$$\hat{H}_{\text{int}} = \hat{\mathbf{d}}\cdot\mathbf{E}(t), \tag{2.3}$$

where $\hat{\mathbf{d}} = e\hat{\mathbf{r}}$ is the dipole operator. Assuming the two-level atom has no permanent dipole moment, the interaction can be purely described by the off-diagonal entries of $\mathbf{d}_{ij} = \langle i|\,\hat{\mathbf{d}}\,|j\rangle$:

$$\hat{H}_{\text{int}} = \hbar\Omega\cos(\omega t + \phi)\left(|g\rangle\langle e| + |e\rangle\langle g|\right), \tag{2.4}$$

with the Rabi frequency defined as $\Omega = \frac{1}{\hbar}\mathbf{d}_{ge}\cdot\mathbf{E}_0$ giving the rate at which the system cycles between the two states with resonant driving. For the linearly polarised case, the Rabi frequency reduces to $\Omega = \frac{1}{\hbar}eX_{ge}|\mathbf{E}_0|$, with $X_{ge} = \langle g|\,\hat{x}\,|e\rangle$. The Schrödinger equation then describes the evolution of this system:

$$i\hbar\frac{\partial|\Psi(t)\rangle}{\partial t} = \hat{H}\,|\Psi(t)\rangle\,, \tag{2.5}$$

with the Hamiltonian $\hat{H} = \hat{H}_{atom} + \hat{H}_{int}$. To simplify the solution we make a transformation to the interaction picture, first writing $\hat{H}$ in its time dependent and independent

parts:

$$\hat{H} = \underbrace{\frac{\hbar\omega}{2}\left(|e\rangle\langle e| - |g\rangle\langle g|\right)}_{\hat{H}_0} + \underbrace{\frac{\hbar\Delta}{2}\left(|g\rangle\langle g| - |e\rangle\langle e|\right) + \frac{\hbar\Omega}{2}\left(e^{i(\omega t-\phi)} + e^{-i(\omega t-\phi)}\right)\left(|e\rangle\langle g| + |g\rangle\langle e|\right)}_{\hat{V}} \tag{2.6}$$

The transformation into the rotating frame of the interaction picture is completed with the unitary operator, $\hat{V}_1 = e^{i\hat{H}_0 t/\hbar}\hat{V}e^{-i\hat{H}_0 t/\hbar}$, giving the interaction picture Hamiltonian (in matrix form):

$$\hat{V}_1 = \frac{\hbar}{2}\begin{pmatrix} \Delta & \Omega e^{i\phi}\left(1 + e^{-2i(\omega t+\phi)}\right) \\ \Omega e^{-i\phi}\left(1 + e^{2i(\omega t+\phi)}\right) & -\Delta \end{pmatrix} \tag{2.7}$$

The rapidly oscillating terms will average quickly over any appreciable timescale and so we can make the rotating wave approximation where $e^{2i\omega t} \to 0$:

$$\hat{V}_1 = \frac{\hbar}{2}\begin{pmatrix} \Delta & \Omega e^{i\phi} \\ \Omega e^{-i\phi} & -\Delta \end{pmatrix}. \tag{2.8}$$

The Schrödinger equation in the interaction picture $i\hbar\frac{\partial|\Psi\rangle}{\partial t} = \hat{V}_1|\Psi\rangle$ allows us to write down the evolution of a general state $|\Psi_I\rangle = c_g(t)|g\rangle + c_e(t)|e\rangle$:

$$2i\frac{\partial c_g(t)}{\partial t} = \Delta c_g(t) + \Omega e^{-i\phi}c_e(t) \tag{2.9}$$

$$2i\frac{\partial c_e(t)}{\partial t} = \Omega e^{i\phi}c_g(t) - \Delta c_e(t) \tag{2.10}$$

The solution to these coupled differential equations for the population in the excited state, given an initial ground state occupation, is:

$$|c_e(t)|^2 = \frac{\Omega^2}{\tilde{\Omega}^2}\sin\left(\frac{\tilde{\Omega}t}{2}\right), \tag{2.11}$$

where $\tilde{\Omega}^2 = \Omega^2 + \Delta^2$ is the generalised Rabi frequency at which the system undergoes Rabi flopping; a full oscillation between the excited and ground states.

2.1.2 The optical Bloch equations

Thus far we have ignored the effects of spontaneous emission in the two level atom. The optical Bloch equations allow a succinct way of including this damping of the classical

dipole. To derive these equations we start from the density matrix for our two level system:

$$|\Psi_I\rangle\langle\Psi_I| = \begin{pmatrix} |c_g|^2 & c_g c_e^* \\ c_e c_g^* & |c_e|^2 \end{pmatrix} = \begin{pmatrix} \rho_{gg} & \rho_{ge} \\ \rho_{eg} & \rho_{ee} \end{pmatrix}, \tag{2.12}$$

then make a change of variable such that $\tilde{\rho}_{ge} = \rho_{ge} e^{-i\Delta t}$ and $\tilde{\rho}_{eg} = \rho_{eg} e^{i\Delta t}$. The Heisenberg equations of motion gives:

$$\begin{aligned} \dot{\rho}_{gg} &= \frac{i}{2}\left(\Omega^* \tilde{\rho}_{eg} - \Omega \tilde{\rho}_{ge}\right), \\ \dot{\rho}_{ee} &= -\frac{i}{2}\left(\Omega^* \tilde{\rho}_{eg} - \Omega \tilde{\rho}_{ge}\right), \\ \dot{\tilde{\rho}}_{ge} &= -i\Delta\tilde{\rho}_{ge} + \frac{i}{2}\Omega^*\left(\rho_{ee} - \rho_{gg}\right), \\ \dot{\tilde{\rho}}_{eg} &= i\Delta\tilde{\rho}_{eg} - \frac{i}{2}\Omega\left(\rho_{ee} - \rho_{gg}\right), \end{aligned} \tag{2.13}$$

where we note that $\dot{\rho}_{gg} = -\dot{\rho}_{ee}$ and $\dot{\tilde{\rho}}_{ge} = \dot{\tilde{\rho}}_{eg}^*$. Taking advantage of these symmetries, we can define the parameters of the familiar Bloch vector $\mathbf{a} = (u, v, w)$:

$$u = \tilde{\rho}_{ge} + \tilde{\rho}_{eg}, \tag{2.14}$$

$$iv = \tilde{\rho}_{ge} - \tilde{\rho}_{eg}, \tag{2.15}$$

$$w = \rho_{gg} - \rho_{ee}. \tag{2.16}$$

The simplified set of equations in terms of these parameters give us the undamped optical Bloch equations (also known as the Maxwell-Bloch equations):

$$\dot{u} = \Delta v, \tag{2.17}$$

$$\dot{v} = -\Delta v + \Omega w, \tag{2.18}$$

$$\dot{w} = -\Omega v. \tag{2.19}$$

The inclusion of spontaneous decay into these equations is achieved with the phenomenological inclusion of a damping term with decay rate Γ into Equation (2.13):

$$\begin{aligned}
\dot{\rho}_{gg} &= \frac{i}{2}\left(\Omega^*\tilde{\rho}_{eg} - \Omega\tilde{\rho}_{ge}\right) + \Gamma\rho_{ee}, \\
\dot{\rho}_{ee} &= -\frac{i}{2}\left(\Omega^*\tilde{\rho}_{eg} - \Omega\tilde{\rho}_{ge}\right) - \Gamma\rho_{ee}, \\
\dot{\tilde{\rho}}_{ge} &= -i\Delta\tilde{\rho}_{ge} + \frac{i}{2}\Omega^*\left(\rho_{ee} - \rho_{gg}\right) - \frac{\Gamma}{2}\rho_{eg}, \\
\dot{\tilde{\rho}}_{eg} &= i\Delta\tilde{\rho}_{eg} - \frac{i}{2}\Omega\left(\rho_{ee} - \rho_{gg}\right) + \frac{\Gamma}{2}\rho_{eg},
\end{aligned} \tag{2.20}$$

giving the complete optical Bloch equations:

$$\dot{u} = \Delta v - \frac{\Gamma}{2}u, \tag{2.21}$$

$$\dot{v} = -\Delta v + \Omega w - \frac{\Gamma}{2}v, \tag{2.22}$$

$$\dot{w} = -\Omega v - \Gamma(w-1). \tag{2.23}$$

After a driving field is switched on and transient behaviour (a timescale on the order of $1/\Gamma$) has decreased, the time derivatives approach $\dot{u} = \dot{v} = \dot{w} = 0$. Solving the resulting linear system of equations gives the steady state solution:

$$\begin{pmatrix} u \\ v \\ w \end{pmatrix} = \frac{1}{\Delta^2 + \frac{\Omega^2}{2} + \frac{\Gamma^2}{4}} \begin{pmatrix} \Omega\Delta \\ \frac{\Omega\Gamma}{2} \\ \Delta^2 + \frac{\Gamma^2}{4} \end{pmatrix} \tag{2.24}$$

2.2 Forces on the Atom

The dipole moment induced on an atom by an electric field is given by:

$$\mathbf{p} = \alpha\mathbf{E} \tag{2.25}$$

where $\alpha = \epsilon_0\chi_a$ is the polarisability. The dipole moment can be written down in terms of the Bloch vector variables u and v (Equation (2.14) and 2.15), giving in-phase and in quadrature components for the rotating frame, which assuming an electric field polarised in the $\hat{x}$ direction gives:

$$\mathbf{p} = -eX_{ge}\left(u\cos(\omega t) - v\sin(\omega t)\right)\hat{\mathbf{x}}. \tag{2.26}$$

The potential $U(\mathbf{r})$ formed from the interaction of this dipole with the driving field allows the force on the atom to be calculated:

$$U(\mathbf{r}) = -\frac{1}{2}e\mathbf{r}\cdot\mathbf{E} \tag{2.27}$$

$$\mathbf{F}(\mathbf{r}) = -\nabla U(\mathbf{r}), \tag{2.28}$$

with the z component of the force given by:

$$F_z = -ex\left(\frac{\partial E_0}{\partial z}\cos(\omega t - kz) + kE_0\sin(\omega t - kz)\right). \tag{2.29}$$

The timescale of the electric field oscillations is fast compared to the physical response of the atom for typical field magnitudes, so we may take a time average over one driving field cycle:

$$\bar{F_z} = -\frac{eX_{ge}}{2}\left(u\frac{\partial E_0}{\partial z} - vE_0k\right) \tag{2.30}$$

$$= \underbrace{\frac{\hbar k\Gamma\Omega^2}{4}\frac{1}{\Delta^2 + \frac{\Omega^2}{2} + \frac{\Gamma^2}{4}}}_{F_{\text{dipole}}} + \underbrace{\frac{\hbar\Delta\Omega}{2}\frac{1}{\Delta^2 + \frac{\Omega^2}{2} + \frac{\Gamma^2}{4}}\frac{\partial\Omega}{\partial z}}_{F_{\text{scatt}}} \tag{2.31}$$

where we have labelled the force from the in-phase component of the dipole as the dipole force, and the quadrature component as the scattering force.

2.2.1 Dipole Force

The potential that gives rise to the dipole force is proportional to the intensity of light and can be written neatly in terms of experimental quantities [87]:

$$U_{\text{dipole}}(\mathbf{r}) = -\frac{3\Gamma\lambda^2\lambda_0^4}{16c^2\pi^3(\lambda^2 - \lambda_0^2)}I(\mathbf{r}) \tag{2.32}$$

with the scattering rate found by dividing F_{scatt} by the photon momentum $\hbar k$:

$$\Gamma_{\text{scatt}}(\mathbf{r}) = -\frac{3\Gamma^2\lambda\lambda_0^8}{16c^3\hbar\pi^4(\lambda^2 - \lambda_0^2)^2}I(\mathbf{r}) \tag{2.33}$$

For cases where the laser detuning from the atomic resonance is large, such that the scattering rate drops towards zero, then a purely conservative potential is formed. This potential is the basis for optical dipole traps (also known as optical tweezers). Current cooling techniques require high optical powers to form deep traps with large volumes for atomic samples. The development of relatively high power fibre amplified laser systems, such as those used in manufacturing, has made optical dipole trapping ubiquitous with cold atom and BEC physics. Typically these traps are formed by combining more than

one Gaussian laser beam into a crossed dipole trap.

Gaussian Beams

The ease with which Gaussian beams can be focused makes them an obvious choice for the formation of optical traps. For lasers with a high M^2 value, most of the optical power will be utilised to form the trap.

The electric field of a Gaussian laser beam propagating along the $\hat{z}$ direction and polarised in the $\hat{x}$ direction is:

$$\hat{E}(r,z) = \hat{x}\sqrt{\frac{2Pw_0}{\pi}}\frac{1}{w(z)}\mathrm{Re}\left[\exp\left(\frac{-r^2}{w(z)^2} + ikz + \frac{ikr^2}{2R(z)} + i\zeta(z)\right)\right] \tag{2.34}$$

With $r^2 = x^2 + y^2$, $w(z) = w_0\sqrt{1+(z/z_R)}$ (beam width), $R(z) = z\left(1+(z_R/z)^2\right)$ (wavefront curvature), $\zeta(z) = \tan^{-1}(z/z_R)$ (Gouy phase). Here z and r are the axial and radial distance from the waist respectively, P is the beam power, w_0 is the beam waist, k is the wavenumber and z_R is the Rayleigh length.

For a single beam the optical potential is proportional to the intensity of light (Equation (2.32)). When combining multiple beams the interference effects in the electric field are important to consider, such as the case for optical lattices. These small scale variations in the intensity fields are undesirable for voluminous optical traps but can be mitigated in two ways. Firstly, lasers with a broad linewidth can be used such that high frequency spatial variations average out. Secondly, lasers with significantly differing wavelengths can be used, creating a fast moving travelling wave that becomes time averaged away for the slow moving atoms. Keeping these considerations in mind, the intensity field of a Gaussian beam can be used to model the potential:

$$I_{\mathrm{Gaus}}(x,y,z) = \frac{2P}{\pi w(z)^2}\exp\left(-\frac{2\left(x^2+y^2\right)}{w(z)^2}\right). \tag{2.35}$$

Let us consider the form of the resulting trap by making a series expansion around the centre along the x direction:

$$\begin{aligned} U_{\mathrm{dipole}}(x) &= C_d I_{\mathrm{Gaus}}(x,0,0) && (2.36)\\ &= C_d\frac{2P}{\pi w_0^2}\exp\left(\frac{-2x^2}{w_0^2}\right) && (2.37)\\ &= C_d\frac{2P}{\pi w_0^2}\left(1-\frac{2}{w_0^2}x^2+\mathcal{O}(x^4)\right), && (2.38)\end{aligned}$$

where C_d is the constant in Equation (2.32). Up to third order the trap is well approximated by a harmonic potential of the form:

$$V(x) = \frac{1}{2} m\omega_x^2 x^2, \tag{2.39}$$

where m is the mass of the atom and ω_x is the harmonic trapping frequency in the x direction. Solving gives a trapping frequency of:

$$\omega_x = 2\sqrt{\frac{C_d 2P}{\pi m w_0^4}}. \tag{2.40}$$

This approximation assumes the centre of the trap is formed at the centre of the optical potential. The introduction of a gravitational term to a harmonic trapping potential creates a sag in the trap:

$$V(y) = \frac{1}{2} m\omega_y^2 y^2 - mgy \tag{2.41}$$

$$= \frac{1}{2} m\omega_y^2 \left(y - \frac{g}{\omega_y^2} \right)^2 - \frac{1}{2} m \frac{g^2}{\omega_y^2}, \tag{2.42}$$

where $y_0 = \frac{g}{\omega_y^2}$. Now consider a dipole beam placed horizontal with gravity in the $\hat{y}$ direction. We make an expansion around y_0 in the $\hat{y}$ direction:

$$U(x,y,z) = C_d I_{Gaus}(x,y,z) - mgy \tag{2.43}$$

$$= gmy_0 + gm(y - y_0) + \left(C_d \frac{2P}{\pi w_0^2} e^{\frac{-2y_0^2}{w_0}} \right) \left(1 - \frac{4y_0}{w_0^2}(y - y_0) - \frac{2}{w_0^4}\left(w_0^2 - 4y_0\right)(y - y_0)^2 \right) + O(y)^3. \tag{2.44}$$

Taking the quadratic term we can find the adjusted trapping frequency by setting it equal to Equation (2.39):

$$\omega_y^* = 2\sqrt{\frac{C_d 2P}{\pi m w_0^4}} e^{-y_0^2/w_0^2} \sqrt{1 - 4y_0^2/w_0^2}. \tag{2.45}$$

For deep traps, the sag is much less than the width of the laser beam $y_0 \ll w_0$, so

making a series expansion around y_0/w_0 the adjusted trapping frequency reduces to:

$$\omega_y^* = 2\sqrt{\frac{C_d 2P}{\pi m w_0^4}}\left(1 - 3\frac{y_0^2}{w_0^2} + O(\frac{y_0}{w_0})^4\right) \tag{2.46}$$

$$\omega_y^* \approx \omega_y\left(1 - 3\frac{g^2}{\omega_y^4 w_0^2}\right). \tag{2.47}$$

Bessel Beams

Although using Gaussian beams is optically simple when creating dipole traps, their use for the optical guiding of atoms is limited by the Rayleigh length, $z_R = \frac{\pi w_0^2}{\lambda}$. Beyond this length, the intensity of the central peak rapidly drops, and the waist increases. An alternative option is to use a non-diffracting Bessel beam. Consider the electromagnetic wave equation:

$$\left(\nabla^2 - \frac{1}{c^2}\frac{\partial^2}{\partial t^2}\right) E(\mathbf{r}, t) = 0, \tag{2.48}$$

with the corresponding solution propagating in the $\hat{z}$ direction [88]:

$$E(x, y, z > 0, t) = e^{i(\beta z - \omega t)} \int_0^{2\pi} A(\phi) \exp\left(i\alpha(x\cos\phi + y\sin\phi)\, d\phi, \right. \tag{2.49}$$

where $\beta^2 + \alpha^2 = (\omega/c)^2$ and $A(\phi)$ is a complex function. When β is real, it represents a wave vector parallel to the propagation direction and the time averaged intensity (found by integrating over) becomes a function of only x and y:

$$I(x, y, z > 0) = \frac{\varepsilon_0}{2}|E(x, y, z > 0, t)|^2 \tag{2.50}$$

$$= \frac{\varepsilon_0}{2}\left|\int_0^{2\pi} A(\phi) \exp\left(i\alpha(x\cos\phi + y\sin\phi)\, d\phi\right|^2\right. \tag{2.51}$$

$$= I(x, y, z = 0). \tag{2.52}$$

Thus our solution is a non-diffracting field along $\hat{z}$. The case where we also have azimuthal symmetry, where $A(\phi)$ is a constant, reduces to:

$$E(x, y, z > 0, t) = e^{i(\beta z - \omega t)} J_0\left(\alpha(x^2 + y^2)\right), \tag{2.53}$$

where J_0 is the zeroth-order Bessel function of the first kind. A beam of this kind would require infinite power to generate all the lobes in the Bessel function. However, an approximately non-diffracting beam can be created by passing a Gaussian beam through a conical lens called an axicon. Figure 2.2 shows a Gaussian beam passing through an

axicon with conical angle α. The intensity of the resulting beam in the near field ($z < f_2$ and $r' < D/2$) is given by [89]:

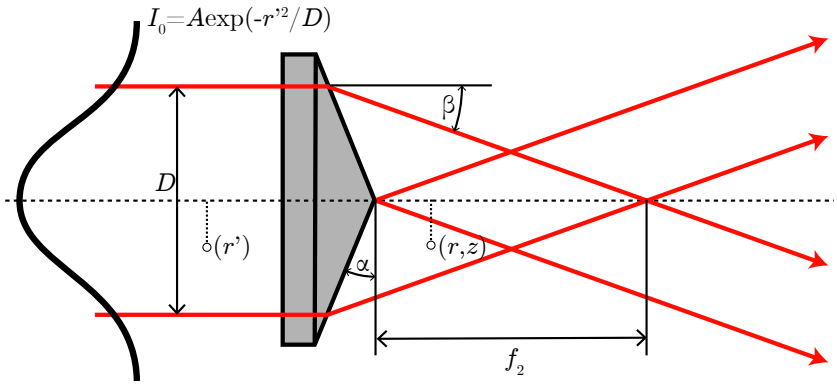

Figure 2.2: A Gaussian beam passes through an axicon with refractive index n and conical angle α. In the region $0 < z < f_2$ a non-diffracting Bessel beam is created.

$$I(r,z) = I_0(r')r'\frac{2\pi k \sin\beta}{\cos^2\beta} J_0(kr\sin\beta)^2, \tag{2.54}$$

where $\beta = \arcsin(n\sin(\alpha) - \alpha)$ is the divergence angle of the generated conical rays and $I_0(r')$ is the intensity of the incoming beam at $r' = z\tan(\beta) + r$. For a Gaussian beam with diameter D we take $I_0 = Ae^{-2r'^2/D}$. The depth of field where the beam remains non-diffracting is $f_2 = \frac{1}{2}D\cot(\beta)$. This beam generates a trapping potential in the central Bessel lobe with an unchanging width, ideal for the optical guiding of cold atoms (Figure 2.3).

2.3 Imaging

As we will see in Chapter 3, the density of a BEC gives a direct method by which to measure the magnitude of a macroscopic wavefunction. Spatially resolved detection of the density is straightforward due to the polarisability of the atoms. The interaction of the atomic clouds with a probe beam can be described by the refractive index [86]:

$$n = \sqrt{1 + 4\pi\chi_a} \approx 1 + 2\pi N\alpha. \tag{2.55}$$

Ideally, a closed two-level transition would be used to image the atom cloud; this can be approximated by keeping the exposure time short. The refractive index can then be described by the cross-section with corresponding real and imaginary parts:

$$n(\mathbf{r}) = 1 + \frac{\sigma_0\lambda\rho(\mathbf{r})}{4\pi}\left(\frac{i}{1+(2\Delta/\Gamma)^2} - \frac{2\Delta/\Gamma}{1+(2\Delta/\Gamma)^2}\right) \tag{2.56}$$

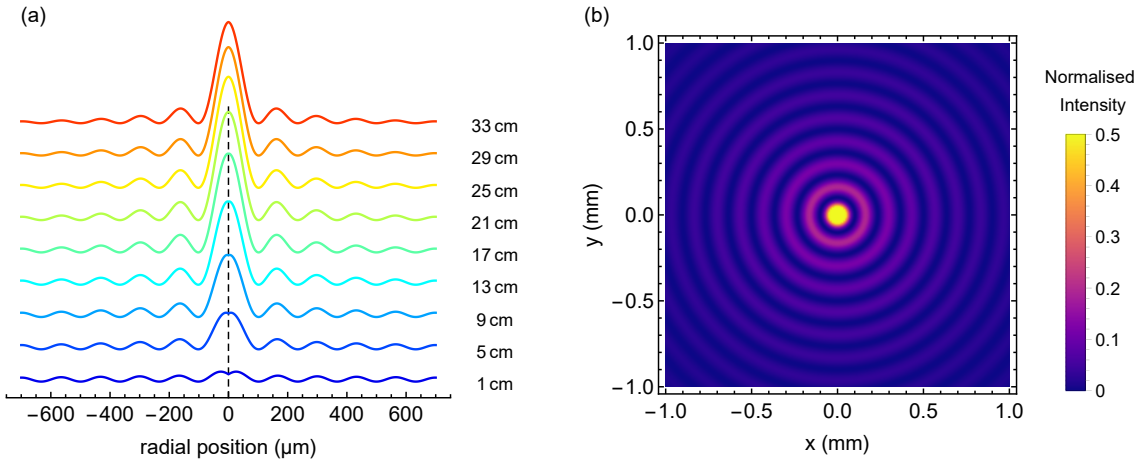

Figure 2.3: Theoretical Bessel beam for parameters D =1 mm, $k = 2\pi \times 1064$ nm, $n = 1.458$ and α =0.5°. a) Radial intensity (mirrored around $r = 0$) of the Bessel beam as a function of distance from the axicon. b) Image of Bessel beam intensity at $z = f_2$.

where $\rho(\mathbf{r})$ is the atomic density and $\sigma_0 = 3^*\lambda^2/(2\pi)$. The factor of Three-Star (3*) is dependent on the polarisation of light and must be chosen carefully [90]. For a probe beam traveling in the $\hat{z}$ direction and an optically thin sample such that we can approximate the refractive index from the column densities of the sample ($\bar{\rho}(x,y) = \int \rho(x,y,z)dz$), the electric field after interaction with the atoms is:

$$E(x,y) = E_0 \exp\left(\frac{2\pi}{\lambda}(n(x,y)-1)\right) \tag{2.57}$$

$$= E_0 t(x,y) e^{i\phi(x,y)}, \tag{2.58}$$

with:

$$t(x,y) = \exp\left(-\frac{\sigma_0 \bar{\rho}(x,y)}{2(1+(2\Delta/\Gamma)^2)}\right) \tag{2.59}$$

$$\phi(x,y) = \frac{\sigma_0 2\Delta \bar{\rho}(x,y)}{2\Gamma(1+(2\Delta/\Gamma)^2)}. \tag{2.60}$$

$t(x,y)$, and $\phi(x,y)$ are the transmission and phase shift of the probe beam, respectively.

2.3.1 Absorption Imaging

Absorption imaging relies only on the absorption of a probe beam as it passes through the atoms. Due to the Beer-Lambert law and assuming near resonant operation, the transmitted intensity becomes:

$$I(x,y) = I_0(x,y) \exp\left(-\frac{\sigma_0 \bar{\rho}(x,y)}{2(1+(2\Delta/\Gamma)^2)}\right). \tag{2.61}$$

Rearranging:

$$\bar{\rho}(x,y) = \frac{2(1+(2\Delta/\Gamma)^2)}{\sigma_0} \ln\left(\frac{I_0(x,y)}{I(x,y)}\right). \tag{2.62}$$

The atomic column density is thus found by taking two images, one with the absorption from the atoms, and another background image. Absorption imaging is particularly robust for atom counting since it is independent of the incoming light intensity. This method, however, is completely destructive due to the large number of scattering events. After each image, an entirely new atomic sample must be prepared.

2.3.2 Dispersive Imaging

Utilising the dispersive element ($\phi(x,y)$) of the refractive index allows the destructive nature of absorption to be minimised, while still extracting reliable spatial information of the density. Moving the probe beam away from resonance, the scattering rate (Equation (2.33)) reduces to zero faster than the dispersive signal (Figure 2.4).

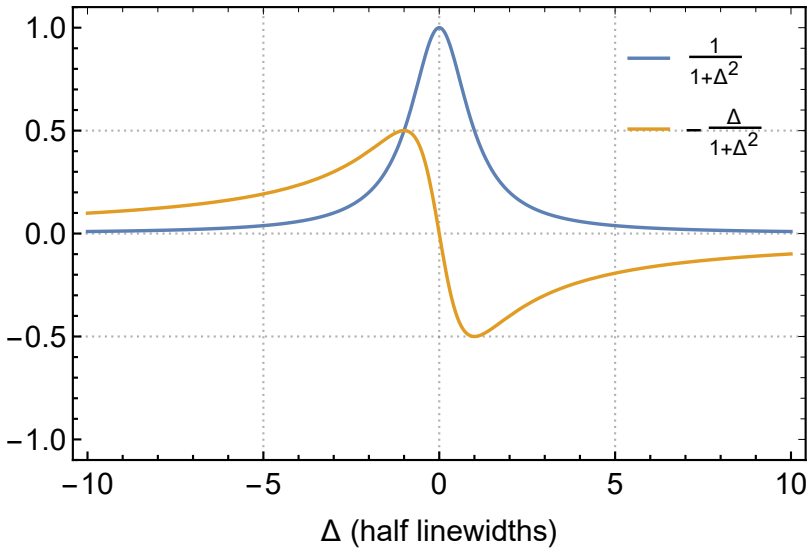

Figure 2.4: Complex and imaginary contributions to the atomic refractive index. The dispersive component has a slower scaling with Δ, leading to viable signals at larger detunings where the destructive transmissive signal drops towards zero.

A number of non-destructive dispersive imaging techniques have been developed for BECs. Dark ground imaging, where the non-diffracted beam of light is blocked by a spatial Fourier filter, was one of the first implementations [91–93]. A small improvement on the imaging signal is achieved with phase contrast imaging, where a phase dot is used to interfere the diffracted and non-diffracted signals [94, 95]. Each of these techniques require precise alignment of the Fourier filters, necessitating specialised beam paths if these methods are used. Faraday imaging utilises the vector part of the

atom-light interaction where birefringence in the atoms induces a phase shift on only one polarisation [96–98]. This method requires an applied magnetic field, which may already be limited by accessing a Feshbach resonance. Off-axis holography is a relatively new technique exploiting heterodyne gain to increase the signal, however this requires the use of an additional reference beam [99].

A simple alternative to these approaches is shadowgraph imaging. Typically applied to flow visualisation in gas or liquids, it can be achieved with few materials such as a smartphone and a bright torch [100]. Applied to cold atoms, no alterations to an existing absorption setup are required, allowing the dual use of imaging paths [101]. In Chapter 5 we utilise this new non-destructive technique to make the first observation of modulational instability in a BEC.

Assuming that we have an optically thin sample with sufficient detuning that the absorption is flat across the extent of the image, then the propagation of light after the sample is given by Fresnel propagation:

$$I_z(\mathbf{r}) = \left| e^{i\phi(\mathbf{r})} * P_z(\mathbf{r}) \right|^2, \tag{2.63}$$

with the Fresnel propagator:

$$P_z(\mathbf{r}) = -\frac{i}{\lambda z} e^{i\pi(|\mathbf{r}|^2)/(\lambda z)}, \tag{2.64}$$

where z is the distance from the sample and $*$ is the linear 2D convolution. The form of this propagation is simplified in Fourier space where:

$$\mathcal{F}[P_z](\mathbf{k_r}) = e^{i\pi\lambda z(|\mathbf{k_r}|^2)}, \tag{2.65}$$

with $\mathbf{k_r}$ the spatial frequency. Equation (2.63) then becomes:

$$\mathcal{F}[I_z](\mathbf{k_r}) = \int d\mathbf{r} \left| e^{i\phi\left(\mathbf{r} - \frac{\lambda z \mathbf{k_r}}{2}\right)} \right|^2 e^{-2\pi i \mathbf{r}\cdot\mathbf{k_r}} \tag{2.66}$$

For small z as in the case of near field imaging, we may linearise Equation (2.66) function around $z = 0$ and then transform back to spatial co-ordinates:

$$I_z(\mathbf{r}) = I_0(\mathbf{r}) - \frac{\lambda z}{2\pi} \nabla \left(I_0(\mathbf{r}) \nabla \phi(\mathbf{r}) \right) \tag{2.67}$$

Again we can make an approximation using near field imaging whereby $I_z(\mathbf{r}) - I_0(\mathbf{r}) \approxeq$

$z\frac{\partial I_0(\mathbf{r})}{\partial z}$ to arrive at the transport of intensity equation:

$$\frac{-2\pi}{\lambda}\frac{\partial I_0(\mathbf{r})}{\partial z} = \nabla \cdot I_0(\mathbf{r})\nabla\phi(\mathbf{r}). \tag{2.68}$$

In practice, as a camera cannot be place in the near field, the image is re-imaged with an additional lens external to the vacuum. In the limit of large detunings, where the absorption signal drops towards zero, an expression for the density can be recovered:

$$\bar{\rho}(\mathbf{r}) = -\frac{4\pi\Gamma(1+(2\Delta/\Gamma)^2)}{2\sigma_0\Delta}\frac{1}{\lambda z}\nabla^{-2}\left(\frac{I_z(\mathbf{r})}{I_0(\mathbf{r})}-1\right) \tag{2.69}$$

Although the solution to the inverse Laplacian is ill-posed with only a single image at z, it can be solved with a Fourier method assuming appropriate boundary conditions:

$$\nabla^{-2}f(\mathbb{R}^2 \to \mathbb{R}) = \frac{1}{4\pi}\mathcal{F}^{-1}\left[\frac{1}{|\mathbf{k_r}|^2+\varepsilon}\mathcal{F}[f]\right], \tag{2.70}$$

where ε is a regularisation parameter in order to avoid the complex pole at the origin.

2.4 Hyperfine Splitting

Hyperfine structure in atomic spectra arises from the coupling of an electron's total angular momentum **J** and the total nuclear angular momentum **I**. **J** is given by the sum of the orbital and spin angular momentum (**L** and **S** respectively). The total atomic angular momentum is:

$$\mathbf{F} = \mathbf{J} + \mathbf{I}; \qquad \text{where} \quad |J-I| \leq F \leq J+I. \tag{2.71}$$

The resulting hyperfine structure Hamiltonian is:

$$H_{\text{hfs}} = A_{\text{hfs}}\mathbf{I}\cdot\mathbf{J} + B_{\text{hfs}}\frac{3(\mathbf{I}\cdot\mathbf{J})^2+\frac{3}{2}(\mathbf{I}\cdot\mathbf{J})-I(I+1)J(J+1)}{2I(2I-1)J(2J-1)} + C_{\text{hfs}}f(\mathbf{I},\mathbf{J}) \tag{2.72}$$

Where A_{hfs}, B_{hfs} and C_{hfs} are the magnetic dipole, electric quadrupole and magnetic octopole constants. The function $f(\mathbf{I},\mathbf{J})$ can be found in [102]. Considering only the magnetic dipole contribution, as is the case with $J = 1/2$ levels, the energy shift due to this interaction is:

$$\Delta E_{\text{hfs}} = \frac{1}{2}A_{\text{hfs}}F(F+1) - I(I+1) - J(J+1). \tag{2.73}$$

Each of the hyperfine levels with total atomic angular momentum F are composed of $2F+1$ degenerate magnetic sublevels. The degeneracy can be lifted by the application of a magnetic field. Taken along the $\hat{z}$ direction, the Hamiltonian describing the interaction

of the atom with this field is:

$$H_B = \frac{\mu_B}{\hbar} \left(g_S S_z + g_L L_z + g_I I_z \right) B_z, \tag{2.74}$$

where g_s is the electron spin, g_L is the electron orbital and g_I is the nuclear Landé factor. In cases where the splitting due to the magnetic field is much smaller than the fine structure, the total electron angular momentum is still a good quantum number (**J** remains an eigenvalue of the system). The Hamiltonian reduces to:

$$H_B = \frac{\mu_B}{\hbar} (g_J J_z + g_I I_z) B_z \tag{2.75}$$

where g_J is the fine structure Landé factor. Although approximate solutions are available for splittings much smaller than the hyperfine levels, the intermediate regime requires numerical diagonalisation of the total Hamiltonian $H_{\text{hfs}} + H_B$. For the special case of $J = 1/2$ (as in the case of the groundstate manifold of the D transition in ^{85}Rb and ^{87}Rb) an exact solution is given by the Breit-Rabi equation:

$$E_{|J=1/2,m_J,I,m_I\rangle}(B) = \frac{\Delta E_{hfs}}{2(2I+1)} + \mu_B g_I m B \pm \frac{E_{hfs}}{2} \sqrt{1 + \frac{4mx}{2I+1} + x^2}, \tag{2.76}$$

with

$$x = \frac{(g_J - g_I)\mu_B B}{\Delta E_{hfs}} \qquad \text{and} \qquad \Delta E_{hfs} = A_{hfs}(I + 1/2).$$

In practice, numerically solving the full Hamiltonian avoids the sign ambiguity in the ΔH_{hfs} term.

Chapter 3

Background: Bose-Einstein Condensates

The state of matter known as a Bose-Einstein condensate is perhaps one of the most widely recognised manifestations of quantum mechanics in a macroscopic object. Consisting of a dilute gas of bosons existing at close to absolute zero, where a large number of individual particles occupy the lowest energy state, their behaviour becomes governed by a single effective wavefunction (the order parameter). In this chapter we give a *condensed* theoretical overview of interactions in a BEC. Starting with the Gross-Pitaesvskii equation (GPE), the governing equation for the behaviour of interacting BECs, we then introduce the fundamental tool used in later chapters to control the non-linear behaviour of condensates: the Feshbach resonance. Next, the GPE is transformed into it's hydrodynamic form to analyse the collective oscillation modes of trapped BECs. Experimentally exciting these modes is used as an accurate method to probe the shape of the optical potentials confining the atoms in Chapter 4. The non-linear object known as a soliton is also introduced through an energy functional analysis. Then, an explanation of a non-linear process, and the subject of Chapter 5, modulational instability, is given. Finally, the coupled GPE for two component BEC systems is presented and a simple derivation is given for the miscibility criteria of such mixed condensates, which is the starting point for the experimental work in Chapter 6. The reader would be well served by [13] as a starting point for further study.

3.1 Gross Pitaesvskii Equation

A non-interacting Bose gas, with all atoms in the single particle ground state (ϕ_0), can be described by the product of these states:

$$\Psi(..., \mathbf{r}_i, ...) = \prod_i \phi_0(\mathbf{r}_i), \tag{3.1}$$

where $\int d\mathbf{r}_i |\phi(\mathbf{r}_i)|^2 = 1$. When considering the inclusion of an inter-particle interaction, the diluteness (low-densities) and low temperature of the system, allows a two body

contact potential to be assumed:

$$V_{\text{scatt}}(\mathbf{r}_i - \mathbf{r}_j) = g\delta(\mathbf{r}_i - \mathbf{r}_j), \tag{3.2}$$

where $g = 4\pi\hbar^2 a_s/m$ is the interaction strength with a_s the inter-particle s-wave scattering length. The effective Hamiltonian of this system is then:

$$H = \sum_i \left(\frac{\mathbf{p}_i^2}{2m} + V(\mathbf{r}_i) \right) + g \sum_{i<j} \delta\left(\mathbf{r}_i - \mathbf{r}_j\right), \tag{3.3}$$

where $V(\mathbf{r}, t)$ is the trapping potential. The energy of Equation (3.1) can be written by finding the expectation value of this Hamiltonian, and with the introduction of the wavefunction for the condensed state $\psi(\mathbf{r}) = N^{1/2}\phi(\mathbf{r})$, this becomes:

$$E(\psi) = \int \left(\frac{\hbar^2}{2m} |\nabla\psi(\mathbf{r})|^2 + \frac{g}{2}|\psi(\mathbf{r})|^4 + V(\mathbf{r})|\psi(\mathbf{r})|^2 \right), \tag{3.4}$$

Minimizing this subject to the constraint that the total number of particles is constant with $N = \int d\mathbf{r}|\psi(\mathbf{r})|^2$, gives the GPE [103]:

$$i\hbar \frac{\partial \Psi(\mathbf{r}, t)}{\partial t} = \left(-\frac{\hbar^2}{2m}\nabla^2 + V(\mathbf{r}, t) + g|\Psi(\mathbf{r}, t)|^2 \right) \Psi(\mathbf{r}, t) \tag{3.5}$$

Under this framework the condensate density is simply $\rho(\mathbf{r}, t) = |\Psi(\mathbf{r}, t)|^2$, allowing direct measurements of the magnitude of the condensate wavefunction with relatively simple imaging techniques. Being a particular form of the ubiquitous non-linear Schrödinger equation (NLSE), combined with well developed experimental control over the trapping potential and scattering length, BECs have become a powerful tool in the quantum workshop.

3.2 Feshbach Resonance

The non-linear parameter in the GPE, $g \propto a_s$, governs the behaviour of the BEC due to repulsive ($g > 0$), attractive ($g < 0$) or vanishing ($g = 0$) inter-atomic interactions. Although different atomic elements and species allow us access to varying scattering lengths, it is difficult to swap sources in a BEC apparatus. Furthermore, it is challenging to create an ultra cold atomic source without favourable scattering properties. Instead, the scattering properties, arising from the atom's internal structure, can be controlled with an external field through a Feshbach resonance.

A Feshbach resonance occurs during atom scattering events when the incoming col-

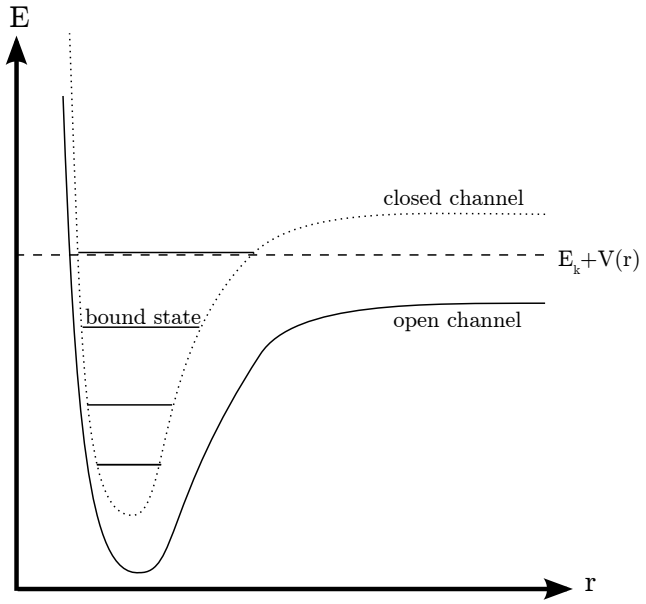

Figure 3.1: Diagram of a Feshbach resonance showing the energy of different states (E) with atom separation (r). An open channel collision (where all bound states exist below the scattering energy) and a nearby closed channel bound state can drastically alter the scattering cross section. Tuning the energetic separation of these two states with an external field can allow direct control over the s-wave scattering length.

lision energy is close to that of a bound state in another channel (usually an electronic internal state) as in Figure 3.1. Temporary coupling to this 'closed' channel causes the collision dynamics to be drastically altered and hence the scattering length can be manipulated. Feshbach resonances typically utilise magnetic fields to alter the energy of the internal bound state, however optical resonances have also been previously used [104, 105]. The variation of a_s due to a magnetic Feshbach resonance is given by:

$$a_s = a_{\mathrm{bg}}\left(1 - \frac{\Delta}{B - B_0}\right), \tag{3.6}$$

where the background scattering length (a_{bg}), width (Δ) and centre (B_0) are usually experimentally constrained values.

In the case of ^{85}Rb, a Feshbach resonance exists for atoms in the $|F = 2, m_F = -2\rangle$ hyperfine state. Figure 3.2 shows the variation of scattering length with applied DC magnetic field. With parameters $a_{bg} = -443a_0$, $\Delta = 10.7$G and $B_0 = 155.04$G [106], the zero crossing magnetic field (165G) is easily accessible and the width makes accurate control ($< 0.1a_0$) over the scattering length feasible.

3.3 Collective Oscillations

Low energy excitations manifest themselves as collective oscillations of the condensate wavefunction around equilibrium. A number of theoretical approaches have been developed [103, 107–109] —here we discuss the hydrodynamic theory.

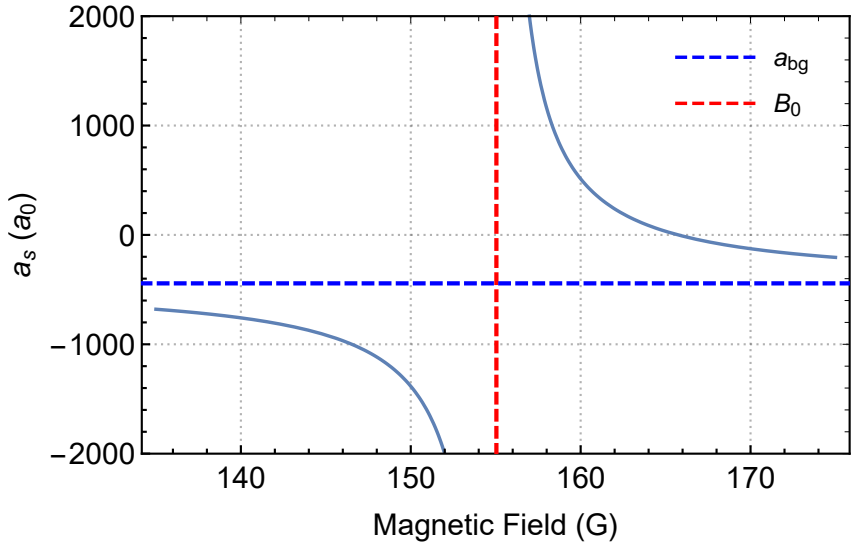

Figure 3.2: Response of the ^{85}Rb self scattering length across the Feshbach resonance at 155G. A convenient zero-crossing is found at 165.7G.

The GPE can be rewritten in a hydrodynamic form in terms of density and velocity fields [109]:

$$\frac{\partial \rho(\mathbf{r},t)}{\partial t} + \nabla \mathbf{v} \rho(\mathbf{r},t) = 0, \tag{3.7}$$

$$m\frac{\partial \mathbf{v}(\mathbf{r},t)}{\partial t} + \nabla\left(\delta\mu + \frac{1}{2}m\mathbf{v}(\mathbf{r},t)^2\right) = 0, \tag{3.8}$$

where the velocity field is given by $\mathbf{v}(\mathbf{r},t) = 1/(2mi\rho)\left(\Psi^*\nabla\Psi - \nabla\Psi^*\Psi\right)$ from Equation (3.5). The difference in chemical potential relative to the ground state is given by:

$$\delta\mu = V(\mathbf{r}) + g\rho - \frac{\hbar^2}{2m\sqrt{\rho}}\nabla^2\sqrt{\rho} - \mu. \tag{3.9}$$

In the case of a ground state of this system, $\mathbf{v} = 0$ and $\delta\mu = 0$. Additionally, in the hydrodynamic limit the kinetic energy pressure is small compared to the interaction and external potential energies. Equation (3.9) then becomes:

$$\rho_0 = \frac{1}{g}\left(\mu - V(\mathbf{r})\right), \tag{3.10}$$

which is the well know Thomas-Fermi ground state for strongly interacting condensates. Given we prepare BECs in a cigar-shaped optical trap (as discussed in following chapters), we can assume a harmonic potential of the following form:

$$V(\mathbf{r}) = \frac{1}{2}m\left(\omega_\perp^2(x^2+y^2) + \omega_z^2 z^2\right). \tag{3.11}$$

Linearising the equations of motion (Equation (3.7) and Equation (3.8)) around this Thomas-Fermi groundstate gives a reduced eigenvalue system:

$$\omega^2 \delta\rho = -\frac{1}{2}\nabla \cdot \left(2\mu/m - \left(\omega_\perp^2 s^2 + \omega_z^2 z^2\right)\right) \nabla\delta\rho, \tag{3.12}$$

where $s^2 = x^2 + y^2$ and $\delta\rho = e^{i\omega t}\left(\rho - \rho_0\right)$. Solutions to this equation of the form $\delta\rho = r^l Y_{l,m}(\theta, \phi)$ (Y_{lm} are the spherical harmonics) give the lowest order dispersion laws (and hence their frequencies):

$$\omega^2(m = \pm l) = l\omega_\perp^2, \tag{3.13}$$

$$\omega^2(m = \pm(l-1)) = (l-1)\omega_\perp^2 + \omega_z^2. \tag{3.14}$$

For the axial quadrupole mode ($m = 0$, $l = \pm 2$), extra care must be taken to diagonalise the degeneracy formed with the monopole excitation. Nonetheless, the excitation eigenvalues can be found [109]:

$$\omega^2(m = 0) = \omega_\perp^2 \left(2 + \frac{3}{2}\lambda^2 \mp \frac{1}{2}\sqrt{9\lambda^4 - 16\lambda^2 + 16}\right), \tag{3.15}$$

where $\lambda = \omega_z/\omega_\perp$. For cigar-shaped geometries where $\omega_z \ll \omega_\perp$, we can linearise around $\lambda = 0$ to get the simplified expressions $\omega \approx \sqrt{5/2}\omega_z$ and $\omega \approx 2\omega_\perp$.

3.3.1 Principal Component Analysis

The collective modes in a BEC are not only a useful tool in understanding excitations, but can also be used to make measurements of the trapping frequencies of the potential. The most obvious method of measuring trapping frequencies is to excite a centre-of-mass (COM) oscillation in each of the three axes. COM oscillations have the benefit that the three axes are completely uncoupled, unlike collective compressional modes, and that the measured oscillation frequency exactly matches the trapping potential. However, the excitation of these COM modes requires some broken symmetry across the trap, such as an offset potential or the ability to kick the atoms (such as a Bragg transition). Equation (3.15) allows us to use the collective quadrupole mode to make the same measurement, and conveniently this excitation is trivial to create with the already present trapping hardware.

Typical experimental runs would involve exciting the BEC, and then taking time-of-flight images at different hold times in the trap, in order to measure the excitation as a sequence of column density images. The frequency of any excitation can be extracted by fitting widths to each image. There are two drawbacks to this method. Firstly, simply

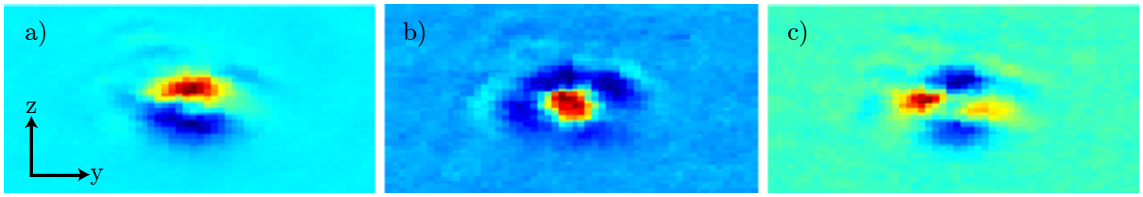

Figure 3.3: Example of PCs resulting from PCA applied to absorption images. a) Center of mass mode. b) Monopole excitation. c) Quadrupole excitation

fitting widths does not make use of all the information present in the images. Secondly, it elicits no information about which modes may have been excited. Principal component analysis (PCA) is a model free analysis method which solves both of these issues [110].

PCA begins with a set of N measurements, each a vector with dimension P. The mean of all measures is subtracted from P and the total data set is $B = N \times (P - \bar{P})$. The covariance matrix of B is given by:

$$S = \frac{B^T B}{N - 1}. \tag{3.16}$$

This is a $P \times P$ matrix where the diagonal entries are the variances of P and the off-diagonals contain the correlations between each dimension in P. The diagonalisation of this matrix results in a basis of eigenvectors, called principal components (PCs) with associated eigenvalues. The eigenvalues give a measure of how much variance in the data set each PC accounts for. Since the basis spans B, we can reconstruct the original data in this uncorrelated space.

In the case of cold atom absorption images, each P vector is of length $m \times n$ where m and n are the pixel widths of the images. The PC basis allows the original images to be reconstructed with a set of coefficients weighting each PC. Including only the PCs with the largest eigenvalues allows smaller contributions such as noise to be filtered out.

Figure 3.3 shows typical PCs extracted from images of an excited BEC. Choosing the correct excitation and projecting across the original images allows only the contribution of that PC to be extracted. Fitting the resulting coefficients accurately measures the frequency of a known oscillation, and hence the trap frequency can be calculated as in Section 4.5.

3.4 Solitons

Solitons, a phenomenon of non-linear wave equations, are localised wave packets which propagate without dispersion. Originally found in shallow water waves, they have since become a well known and useful tool in fibre optics [53]. Solitons in BECs are formed when there exists a balance between kinetic dispersion and attractive interactions.

In the 1D case, the time independent GPE in the absence of any trapping potential ($V(z,t) = 0$) is given by:

$$\mu\Psi(z,t) = \left(-\frac{\hbar^2}{2m}\frac{\partial^2}{\partial z^2} + g|\Psi(z,t)|^2\right)\Psi(z,t). \tag{3.17}$$

This has a stationary soliton solution of the form:

$$\Psi(z,t) = \frac{1}{\sqrt{2l_z}}e^{\left(-\frac{i\mu t}{\hbar}\right)}\operatorname{sech}\left(\frac{z}{l}\right), \tag{3.18}$$

where $l_z = 2\hbar^2/(m\,|g|)$ and $\mu = g^2 m/(8\hbar^2)$.

In 3D, there exist no stable soliton solutions in free space ($V(\mathbf{r},t) = 0$). However, a quasi-1D system can be created with a strong transverse confining potential (as in the case of an optical waveguide where $|\omega_z| \ll \omega_\perp$). Following [111], the stability of soliton solutions in this system can be analysed by a variational method.

The energy functional for the GPE can be found by integrating the contributions of the kinetic, potential and interaction terms:

$$E(\Psi) = \int\left(\frac{\hbar^2}{2m}|\nabla\Psi(\mathbf{r})|^2 + \frac{gN}{2}|\Psi(\mathbf{r})|^4 + V(\mathbf{r})|\Psi(\mathbf{r})|^2\right), \tag{3.19}$$

where $V(\mathbf{r})$ is the potential given in Equation (3.11). Assuming a sech like trial wave-function, with a Gaussian transverse profile:

$$\psi_a(r,z) = \frac{1}{\sqrt{2\pi l_\perp^2 l_z}}\exp\left(-\frac{r^2}{2l_\perp^2}\right)\operatorname{sech}\left(\frac{z}{l_z}\right), \tag{3.20}$$

the integrated energy is then [111]:

$$\epsilon = \frac{1}{2\gamma_\perp^2} + \frac{\gamma_\perp^2}{2} + \frac{1}{6\gamma_z^2} + \frac{\pi^2\lambda^2\gamma_z^2}{24} + \frac{\alpha}{3\gamma_\perp^2\gamma_z}, \tag{3.21}$$

where $\gamma_\perp = l_\perp/\sqrt{\hbar/(m\omega_\perp)}$, $\gamma_z = l_z/\sqrt{\hbar/(m\omega_z)}$ and $\alpha = Na_s/\sqrt{\hbar/(m\omega_\perp)}$.

A stationary point on this energy surface indicates the existence of a soliton solution. However, this does not guarantee the found soliton is stable under perturbations of its size. To find the stability, the Hessian containing the second partial derivatives of the energy surface must be inspected. Figure 3.4 plots Equation (3.21) for parameters typical of the apparatus discussed in this thesis: $\omega_z = 2\pi \times 3i$ Hz (where the imaginary frequency indicates an anti-trapping potential), $\omega_\perp = 2\pi \times 70$ Hz, $N = 2 \times 10^4$ and $a_s = -0.8a_0$. Two stationary points exist, with a stable point found at $\gamma_\perp = 0.9$ and $\gamma_z = 1.26$ corresponding to a soliton in the trap of radial and axial size $l_\perp = 1.2$ µm and $l_z = 8$ µm, respectively.

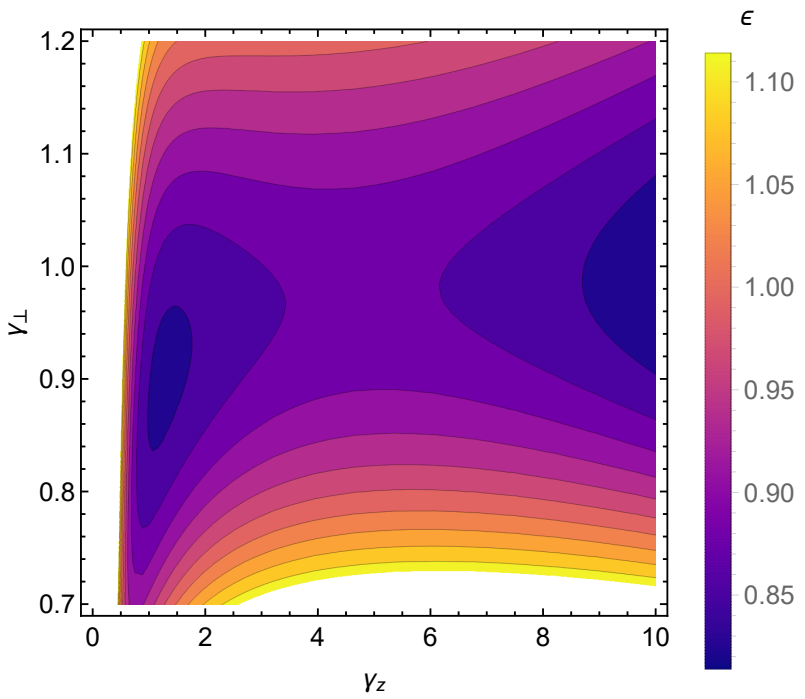

Figure 3.4: Energy surface for experimental parameters in Chapter 5. $\omega_z = 2\pi \times 3i$, $\omega_\perp = 2\pi \times 70$, $N = 2 \times 10^4$ and $a_s = -0.8a_0$. A stable soliton solution exists at $\gamma_\perp = 0.9$ and $\gamma_z = 1.26$ which corresponds to $l_\perp = 1.2$µm and $l_z = 8$µm

3.5 Modulational Instability

The existence of stable solitons as above does not preclude instability from a different mechanism. The energy surface analysis requires only stability in the condensate widths around an equilibrium point, ignoring the effect of any spatial modulations across the BEC. Under certain conditions, these modulations can undergo exponential amplification due to the self focusing nature of attractive interactions, in a process known as modulational instability (MI). Modulational instability can be understood by analysis of the gain

spectrum in the 1D nonlinear Schrödinger equation as in [112]:

$$\frac{\partial A}{\partial z} + \frac{i}{2}\beta_2 \frac{\partial^2 A}{\partial t^2} = i\gamma |A|^2. \tag{3.22}$$

One solution to this equation is a periodic waveform of the form:

$$A(z) = \sqrt{P_0} e^{i\gamma P_0 z}. \tag{3.23}$$

To analyse the stability of this solution to small periodic perturbations, we add a small term where $|a(z,t)|^2 \ll P_0^2$:

$$A(z,t) = \left(\sqrt{P_0} + a(z,t)\right) e^{i\gamma P_0 z}. \tag{3.24}$$

Substituting into Equation (3.22) and linearising the result around A we get:

$$\frac{\partial a}{\partial z} + \frac{i}{2}\beta_2 \frac{\partial^2 a}{\partial t^2} = i\gamma P_0 (a + a^*), \tag{3.25}$$

with corresponding solution:

$$a(z,t) = a_1 \cos(Kz - \Omega t) + a_2^* \sin(Kz - \Omega t), \tag{3.26}$$

where Ω is the frequency of the perturbation with wavenumber K:

$$K(\Omega) = \pm \frac{1}{2}|\beta_2||\Omega| \sqrt{\Omega^2 + \frac{4\gamma P_0}{\beta_2}}. \tag{3.27}$$

The dispersion relation for K identifies the regions where growth is exponential (i.e. the wavenumber K is complex):

$$\Omega^2 < -\frac{4\gamma P_0}{\beta_2}. \tag{3.28}$$

The gain spectrum of the perturbation is given by the imaginary part of K [112]:

$$\Im\left[K\left(\Omega^2 < -\frac{4\gamma P_0}{\beta_2}\right)\right] = \frac{1}{2}|\beta_2||\Omega| \sqrt{-\Omega^2 - \frac{4\gamma P_0}{\beta_2}}, \tag{3.29}$$

which reaches a maximum at $\Omega^2 = \frac{2\gamma P_0}{\beta_2}$ as we can see in Figure 3.5.

The analysis here refers to the treatment of light propagation in optical fibres, whereby the breakup occurs in time. As we show in Chapter 5, guided BECs undergo a modulational instability breaking up into spatially resolved components.

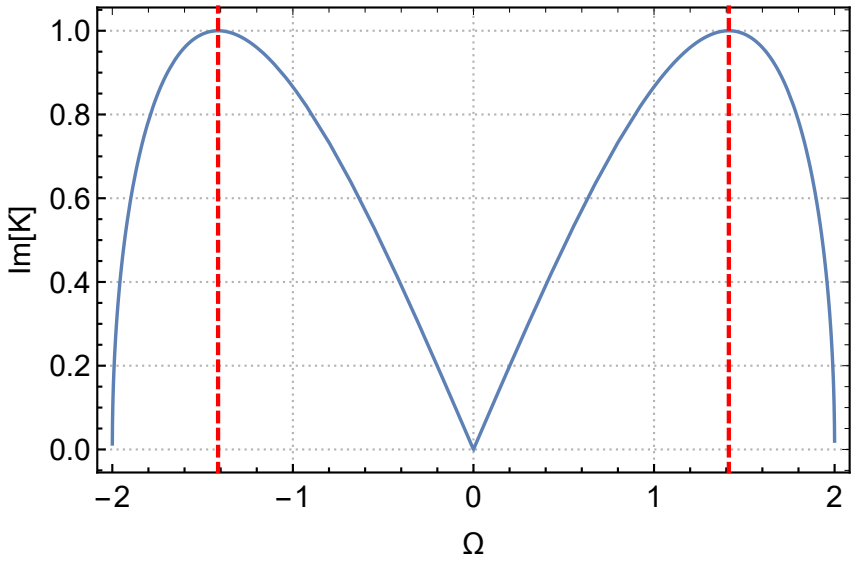

Figure 3.5: Gain spectrum of MI for Equation (3.22) with $\beta_2 = 1$, $\gamma = -1$ and $P_0 = 1$. The maximum growth rate is achieved at $\sqrt{2}$.

3.6 Miscible and Immiscible Mixtures

Single component BECs offer a plethora of phenomena to investigate, but this richness is increased when two component systems are considered. These mixed condensates can be described by coupled GPEs which, neglecting terms due to three-body recombination and electromagnetic coupling, are given as [113]:

$$i\hbar\frac{\partial\Psi_1}{\partial t} = \left(-\frac{\hbar^2}{2m}\nabla^2 + V_1 + g_{11}|\Psi_1|^2 + g_{12}|\Psi_2|^2\right)\Psi_1, \tag{3.30}$$

$$i\hbar\frac{\partial\Psi_2}{\partial t} = \left(-\frac{\hbar^2}{2m}\nabla^2 + V_2 + g_{22}|\Psi_2|^2 + g_{12}|\Psi_1|^2\right)\Psi_2, \tag{3.31}$$

where $g_{ij} = 4\pi\hbar^2 a_{ij}/m$ is the interaction term, with a_{11} and a_{22} the intra-species scattering lengths and a_{12} is the inter-species scattering length. V_1 and V_2 are the trapping potentials for the components 1 and 2, respectively. The corresponding time independent form is:

$$\mu_1\Psi_1 = \left(-\frac{\hbar^2}{2m}\nabla^2 + V_1 + g_{11}|\Psi_1|^2 + g_{12}|\Psi_2|^2\right)\Psi_1, \tag{3.32}$$

$$\mu_2\Psi_2 = \left(-\frac{\hbar^2}{2m}\nabla^2 + V_2 + g_{22}|\Psi_2|^2 + g_{12}|\Psi_1|^2\right)\Psi_2. \tag{3.33}$$

An important property of this system is the components' miscibility. This is a measure of the inclination of the components' to either homogeneously mix or remain separated.

The distinction between these states is driven by the competing interaction terms g_{11}, g_{22}, and g_{12}. Following [114] but additionally including atom number differences for the two components, we can derive a miscibility criterion using the interaction energy density:

$$E_{\text{int}}(r) = \frac{1}{2}\left(g_1 n_1^2(r) + g_2 n_2^2(r) + 2g_{12} n_1(r) n_2(r)\right). \tag{3.34}$$

Consider a condensate containing N_1 and N_2 atoms confined to a box of volume V. For a homogeneously mixed condensate, the interaction energy is found by integrating over the volume:

$$E_{\text{mix}} = \frac{1}{2V}\left(N_1^2 g_{11} + 2N_1 N_2 g_{12} + N_2^2 g_{22}\right). \tag{3.35}$$

If instead the components are completely phase separated, then they will occupy volumes V_1 and V_2, with the total interaction energy:

$$E_{\text{sep}} = \frac{N_1^2 g_{11}}{2V_1} + \frac{N_2^2 g_{22}}{2V_2}. \tag{3.36}$$

Solving for the stationary case where $\frac{\partial E_{\text{sep}}}{\partial V_1} = 0$, the interaction energy becomes:

$$E_{\text{sep}} = \frac{1}{2V}\left(N_1^2 g_{11} + 2N_1 N_2 \sqrt{g_{11} g_{22}} + N_2^2 g_{22}\right). \tag{3.37}$$

Inspecting Equation (3.35) and Equation (3.37) we recover the usual miscibility criterion $g_{12} > \sqrt{g_{11} g_{22}}$ (assuming $g_{11}, g_{12}, g_{22} > 0$). We note that under this analysis the atom number difference between the components is inconsequential.

Part II

Making A Dual-Species Bose-Einstein Condensate

Chapter 4

Experimental Apparatus

4.1 Apparatus Overview

A careful choice of atom is crucial to achieving the phase space densities required to experimentally achieve Bose-Einstein condensation. ^{85}Rb poses an ideal candidate for the work of this thesis, having an easily accessible Feshbach resonance (165G) for control over its interactions. The difficulties in creating pure ^{85}Rb condensates, due to the large natural negative scattering length, are offset by the *relative* ease with which large ^{87}Rb condensates can be created. Here we present a dual-species BEC machine capable of creating 2×10^5 and 2×10^6 condensates of ^{85}Rb and ^{87}Rb, respectively, as well as isotope mixtures, with a duty cycle of 13 s. This apparatus was used to perform the detailed experimental study of phase separated groundstates reported in Chapter 6.

The apparatus described here is a significant improvement on previous iterations of the dual-species BEC machine at the ANU [114–116], and this chapter will focus on the key differences, both in design and implementation, when compared to previous builds. Specifically: the newly designed vacuum system and optics layout greatly increases the optical access; a state-of-the-art ultra-stable current driver combined with magnetic shielding improves the fine scattering length control around the ^{85}Rb Feshbach resonance; a well characterised crossed optical dipole trap produced with a non-diffracting Bessel beam allows stable, reproducible condensate groundstates and the potential for greatly increased atom guiding lengths. Further details on experimental procedures not covered here, such as magneto optical traps (MOT), can be found in [114–116].

The building and characterisation of this apparatus represents a large component of the independent experimental work conducted in this thesis. Vacuum system design and construction (including manufacture of custom internal mounts), optical system layout and construction, as well as the design and implementation of the tuned H-bridge and magnetic shielding system were led by P.J. Everitt. All data and calibrations shown in this chapter were also taken and analysed by P.J. Everitt.

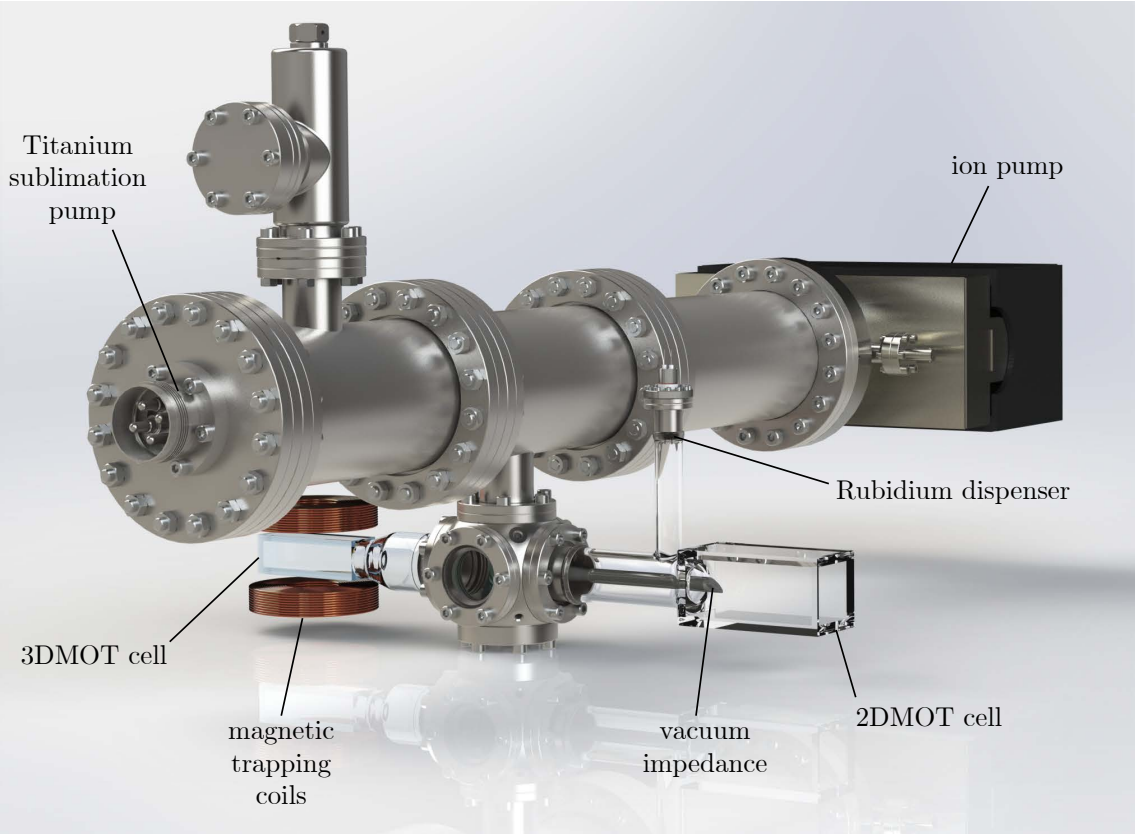

Figure 4.1: Render of the dual-species vacuum system

4.2 Vacuum System

Bose-Einstein condensates of alkali atoms are created at low pressures, necessitating extremely low temperatures in order to achieve transition phase space densities. Without adequate isolation from the room temperature environment (300K), collisions with high kinetic energy particles would limit the efficiency of evaporative cooling and cause heating in the resultant BEC. For this reason an ultra-high vacuum (UHV) system is used, with the atoms isolated from the chamber walls through a combination of magnetic and optical trapping.

The vacuum system is based on a previous 2D+3D MOT design [115]. A render of the system is shown in Figure 4.1. The main science cell geometry is lowered from the main pumping compartments to improve optical access to the trapped atoms. After undergoing vacuum baking, the titanium sublimation pump was used to bring the system down to UHV (1×10^{-10}Torr). Two Alvatec dispensers generate a vapour of rubidium in the 2D MOT cell, separated by a 0.8 mm diameter impedance to the UHV 3D MOT side. The ion pump provides a sufficient pump rate to maintain the UHV while running the dispenser.

4.2.1 Internal Mirror Mount

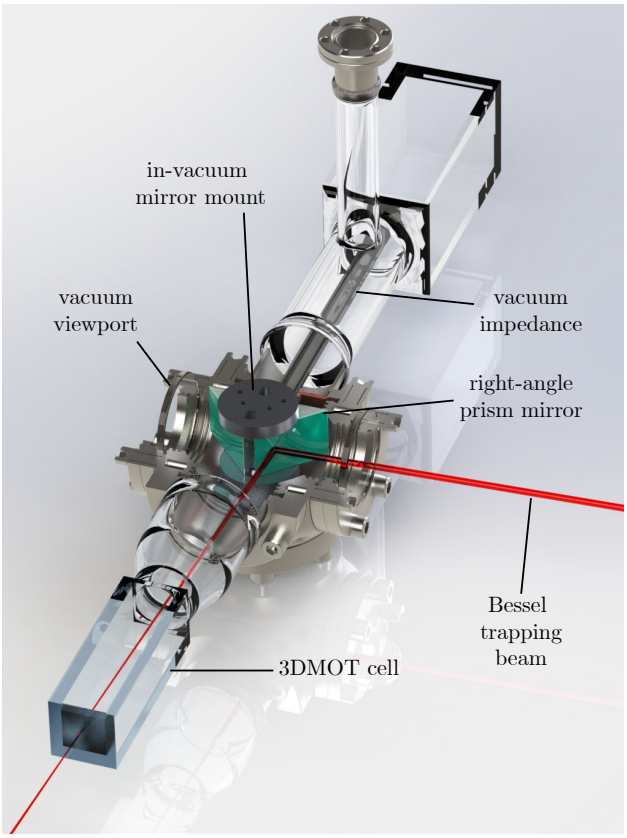

Figure 4.2: Cutaway of the 2D+3DMOT vacuum system. Atoms pass through the impedance and into the 3DMOT cell. Two internally mounted EO3 right-angle prism mirrors are carefully positioned either side of the atom beam. Shown is the path of the optical trapping Bessel beam, utilising an internal mirror to dump to high power outside the vacuum system.

Two internal mirrors are located inside the centre cube between the 2D MOT and 3D MOT glass cells (Figure 4.2). These are placed in a custom designed aluminium mount giving two extra possible beam paths aligned axially along the cell. The mirrors allow high power trapping beams to be dumped outside the system, avoiding internal heating problems inside the vacuum, while the laser cooled atoms from the 2D MOT pass between them through to the 3D trap. Additionally, the on-axis beam path may be used to image clouds axially along the waveguide (Subsection 4.5.3), achieving high optical densities. These extremely high OD clouds would be ideal for the implementation of quantum memory schemes such as electromagnetically induced transparency [117–119].

4.3 Laser System

The laser frequencies required for ^{87}Rb and ^{85}Rb magneto optical trapping on the D2 line are easily accessible with 780nm external cavity diode lasers (ECDL). The laser system consists of a combination of home-built Littrow configuration lasers and Moglabs cateye diode lasers [120], using one laser for each of the trapping and repump transitions for each isotope. All lasers are frequency locked using saturated absorption spectroscopy (SAS) with a combination of current or Zeeman modulation used to generate an error

Isotope	Laser Lock Point	Purpose	Transition	Detuning (mHz)	Power (mW)
^{87}Rb	$F = 2 \rightarrow F = 1, 3$ c.o.	2D trapping	$F = 2 \rightarrow F' = 3$	-15	115
		3D trapping		$[-76, 0]$	80
		Imaging		$[-12, +12]$	2
		Push Beam		-9	0.6
^{85}Rb	$F = 3 \rightarrow F = 3, 4$ c.o. (115MHz detuned)	2D trapping	$F = 3 \rightarrow F' = 4$	-15	80
		3D trapping		$[-76, 0]$	50
		Imaging		$[-12, +12]$	1
		Push Beam		-9	0.4
^{87}Rb	$F = 1 \rightarrow F = 1, 2$ c.o.	2D repump	$F = 1 \rightarrow F' = 2$	0	8
		3D repump		$[-8, +0]$	7
^{85}Rb	$F = 2 \rightarrow F = 1, 2$ c.o.	2D repump	$F = 2 \rightarrow F' = 3$	0	6
		3D repump		$[-3, 0]$	6

Table 4.1: Locking points and detunings for the magneto optical and imaging laser system. All lasers are locked to SAS crossover peaks (c.o.). The ^{85}Rb trapping laser light is frequency shifted by 115 MHz with an AOM before being locked to the $F = 3 \rightarrow F = 3, 4$ c.o. peak. This gives both isotopes trapping lasers to the same detuning from their respective transitions.

signal. Individual lasers and their lock points are shown in Table 4.1.

The two repumping lasers are frequency shifted from their lock point onto resonance by passing through an acousto-optic modulator. This allows control over both the amplitude and detuning of the laser light, required for efficient polarisation gradient cooling. The ^{85}Rb and ^{87}Rb light is combined together with a polarising beam splitter (PBS). The combined beam is then split and coupled to the main optical table through two polarisation maintaining (PM) fibres for the 2D and 3D MOTs, respectively. As the BEC is formed into the lower hyper-fine states, a small number of resonant repumping photons will destroy the sample. An inline fibre switch[1] is used to fully attenuate any remaining photons passing through the PM fibre when the AOM is off.

The MOT trapping laser light production setup for ^{85}Rb and ^{87}Rb is shown in Figure 4.3. The output of two SAS locked ECDLs is passed through two tapered amplifiers, raising the power to approximately 2 W. A small amount of light is split off for both imaging and the push beam, both of which are shifted towards resonance with a double-pass AOM (DPAOM) setup before being coupled to the main table. Careful choice of the ^{85}Rb locking point, shifted 115MHz further off resonance with an AOM inside the locking loop, gives identical detunings from both isotopes' trapping transitions. The remaining light is combined on a non-polarising beam splitter to create coincident trapping light for both isotopes. This is split into two double pass AOM setups for the 2D and 3D MOTs, respectively, which are then coupled to the main science

[1] Agiltron 780nm NS 1x1 Switch.

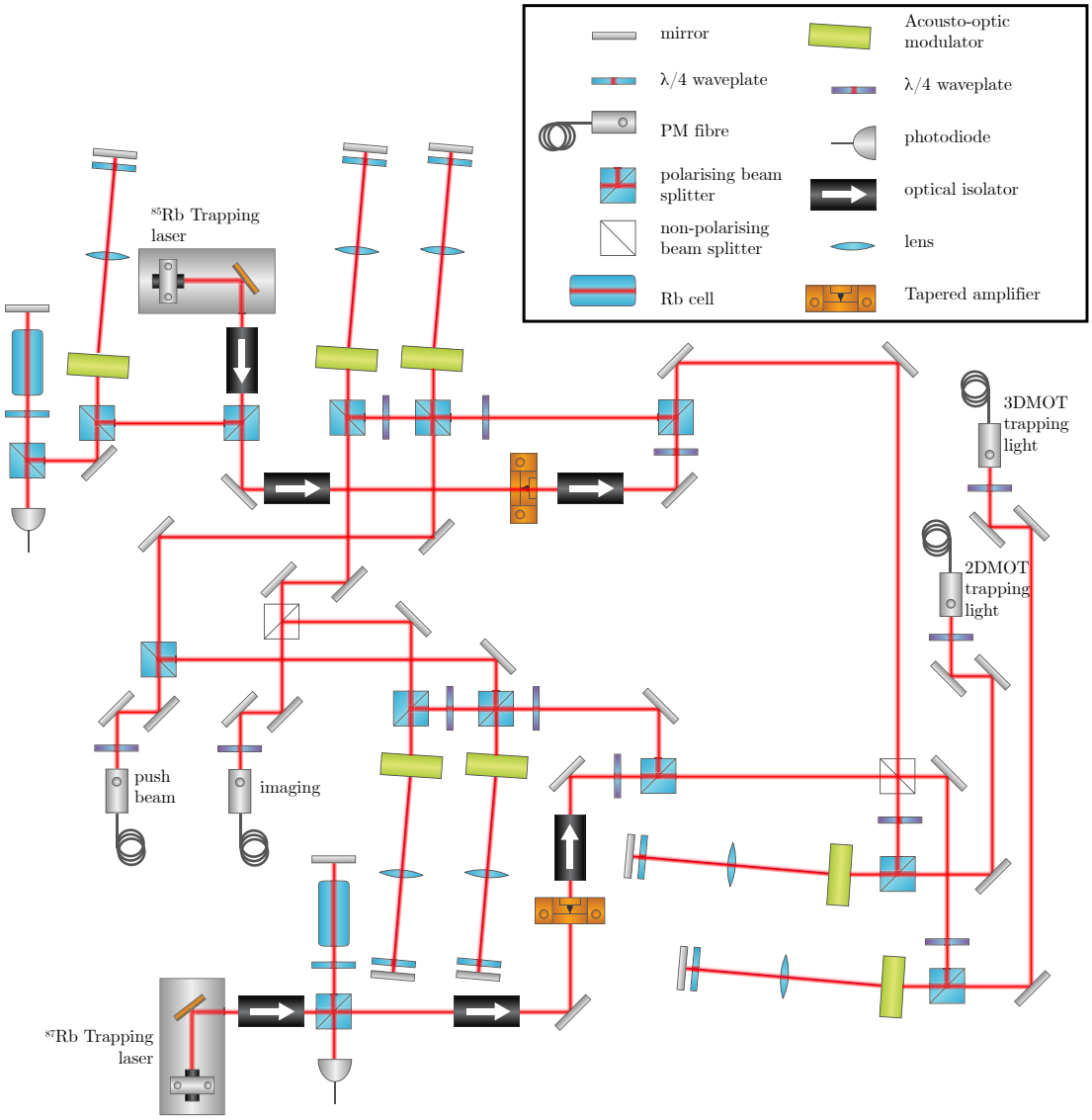

Figure 4.3: The optical table setup for the MOT trapping, push beam and imaging light. Separate ECDLs, locked with saturated absorption spectroscopy, are used for ^{85}Rb and ^{87}Rb. Each is amplified by passing through a tapered amplifier after which light is split off for imaging and the 2D MOT push beam. The split off light passes through four independent DPAOM setups before being recombined and coupled into PM fibre. The remaining ^{85}Rb and ^{87}Rb light is combined and split with a non-polarising beam splitter. Each output port is passed through DPAOM setups, before being coupled into the 2D and 3D trapping fibres.

table.

A full schematic of the vacuum chamber optical layout is shown in Figure 4.4. MOT trapping and repump light from the laser source table is out-coupled and combined for both the 2D and 3D setups. 2D MOT light passes through a telescope increasing the size to a two inch beam diameter. This light is recycled for both the vertical and horizontal 2D MOT beams before being retro-reflected. The push beam is aligned through the

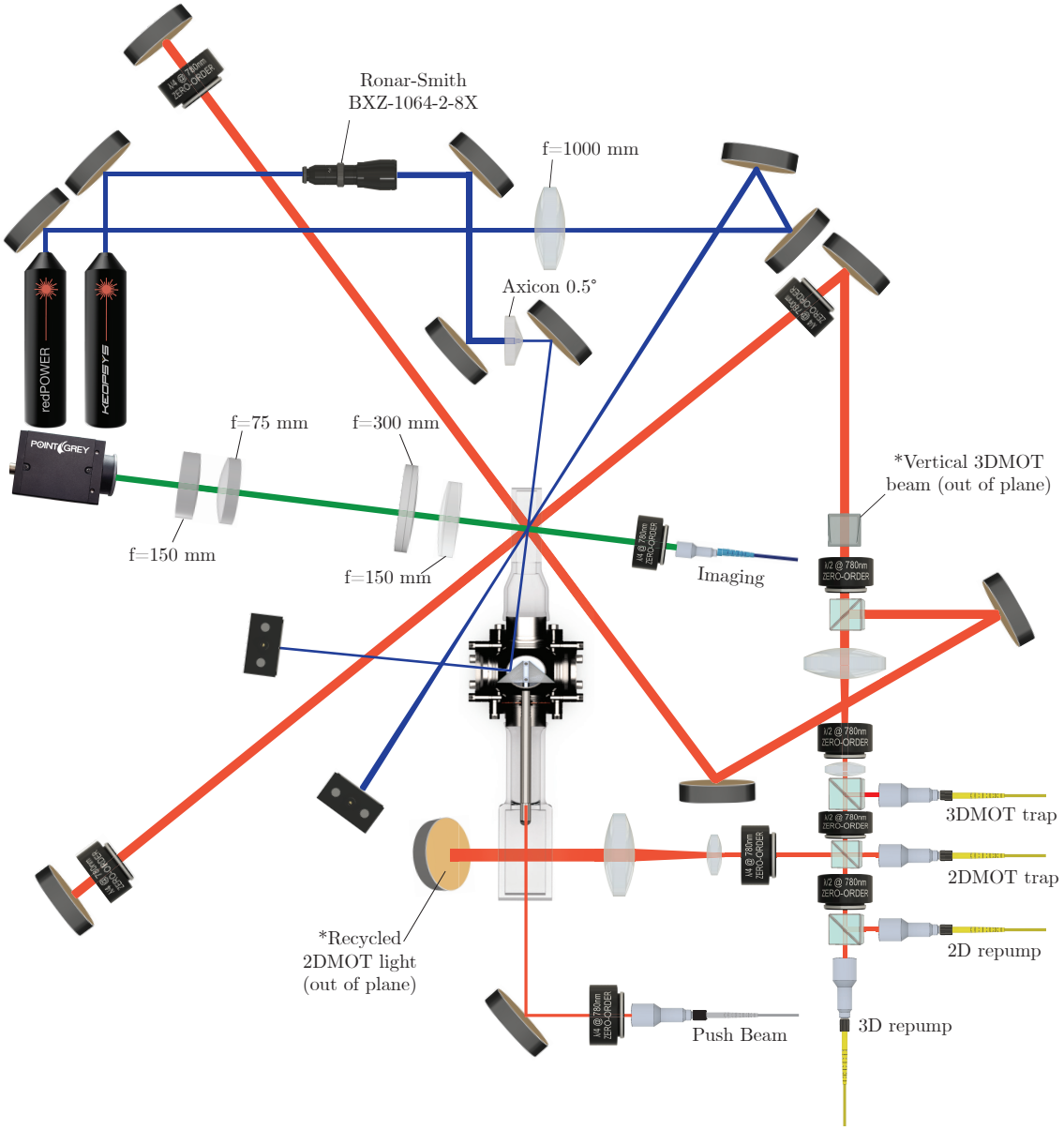

Figure 4.4: Optical layout for the vacuum system table. Beam colors are used as a guide only and are not indicative of laser wavelength. The repump and trapping MOT light (Red) for ^{85}Rb and ^{87}Rb is combined on the laser source table and coupled to the main table via polarisation maintaining fiber. The 2DMOT is formed from a single, slightly focusing, 2 inch beam which is recycled to create both the horizontal and vertical MOT beams with the maximum possible optical power. The 3DMOT is formed from 1 inch beams, with optics placed far from the cell the maximise available optical access. The optical dipole trap is formed from two intersecting high power lasers (Blue). A 30 W Keopsys 1064 nm laser is first passed through a Ronar-Smith BXZ-1064-2-8X beam expander before passing through a 0.5° axicon to form a Bessel beam. This is crossed at 30° by a 30 W redPower 1090 nm fiber laser focused with a $f = 1000$ mm lens. An imaging system (Green) with 3.3× magnification is placed orthogonal to the Bessel beam and is incident on a Pointgrey Grasshopper3 camera.

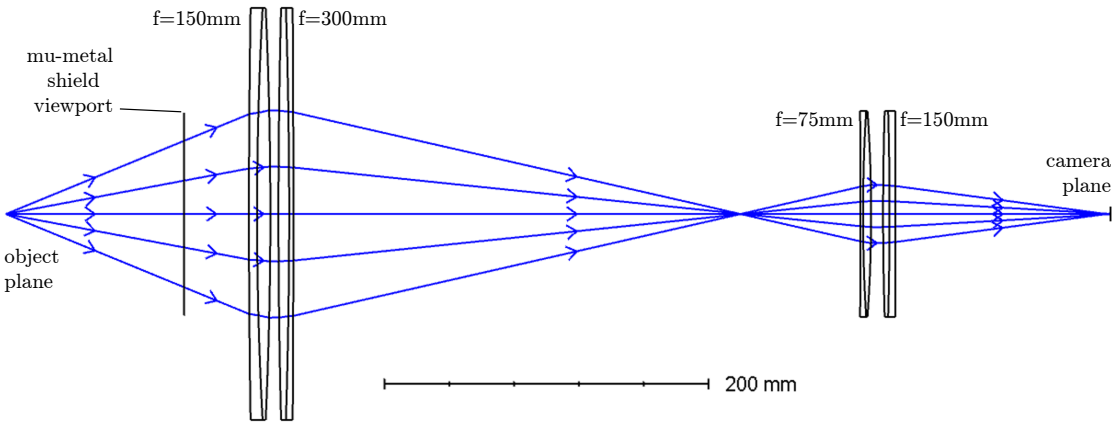

Figure 4.5: Schematic of the imaging system, consisting of two sets of achromatic doublet pairs. Shown is the aperture from the optical access hole in the mu-metal shield. The magnification of the system is 3.3×.

vacuum impedance, which a slight divergence in order to minimise the density in the cold vapor beam as it impacts the 3D MOT. A standard retro-reflected three beam setup is used to create the 3D MOT. The initial beam is enlarged to one inch before being split. A slight convergence in the beam is used to counteract power loss from optics, giving similar intensities in the forward and retro-reflected beams. Optics for the 3D MOT are placed far from the cell to take up a minimum angular space around the cell.

An absorption imaging system is set orthogonal to the optical trapping Bessel beam (Figure 4.4). The image is formed with two sets of achromatic pairs (150mm[2]+300mm[3] and 75mm+150mm[4]) giving a total magnification of 3.3× (Figure 4.5). The image is incident on a Pointgrey Grasshopper3[5] camera, chosen for its high frame rate (up to 3kHz)[101]. The performance of the imaging system was calculated using Zeemax Optic Studio [121] and is shown in Figure 4.6. At a threshold modulation of 5% the modulation transfer function gives a diffraction limited imaging resolution of 3.3 µm. Due to the mu-metal shield aperture, our system achieves a resolution of 5.5 µm. Slightly enlarging the aperture in the shield would improve the performance of the imaging system with potentially a small magnetic field noise increase, although the size of this increase must be checked.

[2]AC508-150-B Ø2" Achromatic Doublet
[3]AC508-300-B Ø2" Achromatic Doublet
[4]MAP1075150-B 1:2 Matched Achromatic Pair
[5]GS3-US-41C6NIR-C

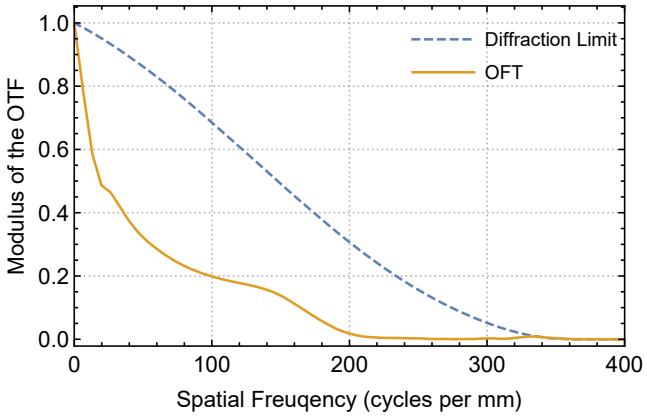

Figure 4.6: Calculated modulation transfer function (MTF) for the imaging system shown in Figure 4.5. The MTF is given by the amplitude of the optical transfer function (OTF). Also shown is the theoretical diffraction limit of the lens system. A threshold modulation of 5% occurs for 180 lines/mm corresponding to an imaging resolution of 5.5 µm.

4.4 Magnetic Field Control

The various cooling techniques used to approach condensation phase space densities are heavily reliant on control over the background magnetic field. Magneto-optical trapping, polarisation gradient cooling and magnetic evaporation require a well defined magnetic zero and magnetic gradient field. In addition, precise control over high magnetic bias fields (∼165G) is required to access the Feshbach resonance of ^{85}Rb with sufficient accuracy over the atom scattering length. This is achieved through a combination of Helmholtz/anti-Helmholtz coils, precise current drivers and passive mu-metal shielding.

The magnetic field at the centre of a coil pair can be found by integrating the Biot–Savart law for a loop of wire carrying a current. The magnetic field at the centre of a Helmholtz coil pair is given by Equation (4.1). For an anti-Helmholtz field the magnetic gradient at the centre is given by Equation (4.2):

$$B = \mu_0 \frac{INa^2}{(d^2/2 + a^2)^{3/2}}, \tag{4.1}$$

$$\frac{\partial B}{\partial z} = \mu_0 \frac{48a^2 dIN}{(4a^2 + d^2)^{5/2}}, \tag{4.2}$$

where μ_0 is the vacuum permeability, I is the current in the coil, N is the number of loops in each coil, a is the radius and d is the separation.

4.4.1 Bias Coils

The background DC magnetic bias field in the apparatus room is approximately 0.3 G. Efficient polarisation gradient cooling requires a well zeroed field. This is achieved with

the use of three large (2m) helmholtz coil pairs, with the main science cell at their centre. The large size of the coils limits the introduction of field gradients and curvature while still reducing the remaining DC field to below 0.05 G, as measured next to the cell (without passive magnetic shielding).

4.4.2 Imaging Coil

An additional Helmholtz coil pair, of diameter 30cm, is placed horizontally on axis with the imaging. The coil pair is used primarily to define a magnetic axis for the atoms along the imaging line. For appropriately chosen imaging light polarisation, the factor of Three-Star (3*) in the atomic susceptibility can be set to 3[90]. With these conditions absorption imaging can be used for accurate atom number measurements.

The coil is also utilised to maximise the magnetic trap loading after Polarisation gradient cooling (PGC) is completed. Due to the zeroed magnetic field, the ^{87}Rb atoms occupy the three MF states in the $|F = 2\rangle$ hyperfine groundstate equally. When loading into the magnetic trap, only the low field seeking state ($|F = 2, m_F = -2\rangle$) is captured. During this transfer, the coil pair applies a bias field of 0.26 G, increasing the captured atoms from 1.4×10^9 to 1.8×10^9. Notably the fraction of atoms captured from the 3.6×10^9 available after PGC MOT is 50%, above the expected 33% if the atoms were simply projected into the three MF states by the trapping field, indicating that the increased load may be due to a small amount of spin-polarising from the coil.

4.4.3 Magnetic Trap

In order to increase optical access around the main science cell, a single pair of coils is used to generate both the quadrupole field for the MOT and magnetic trap, and also the large DC bias field to access the Feshbach resonance of ^{85}Rb. This pair of coils is spaced 51mm apart above and below the science cell (Figure 4.7) with each coil having a central hole diameter of 50mm, outer diameter 96mm, depth 20mm and 120 coil turns. In anti-Helmholtz configuration the magnetic trapping gradient at the trap centre according to Equation (4.2) is 8.6 G/cm/A. The DC bias field generated in Helmholtz configuration (Equation (4.1)) is 23.5 G/A. The particular geometry of coils was chosen to reduce the magnetic curvature at the centre compared to the previous design [122]. The calculated curvature ($-37\,\mathrm{mG/mm^2}$) allows a larger region of constant scattering length when accessing the ^{85}Rb Feshbach resonance.

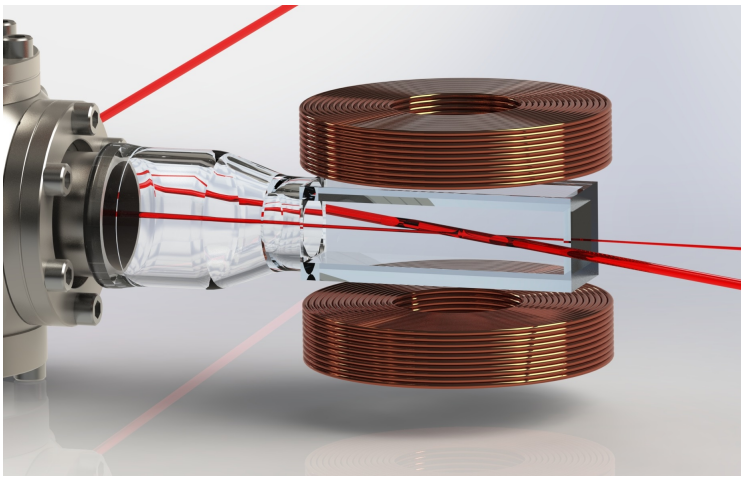

Figure 4.7: 3DMOT cell with magnetic trapping coils. The two optical trapping beams intersect at 30° in the center of the magnetic trap.

4.4.4 H-Bridge

The dual use of the main coil pair requires switching the direction of the current in one of the coils while transferring atoms from the magnetic trap to the optical dipole trap. Rapidly ramping the bias field up to 165G minimises loss due to the large negative scattering length of ^{85}Rb away from the resonance ($-440a_0$).

The large currents (16A), high voltages (140V) and rapid switching times (40A/ms) combined with the required current stability (1ppm) necessitate careful consideration of how this switch is implemented. Figure 4.8 shows a custom designed H-bridge using twin pairs of Crydom D20D40 200V 40A solid state relays. Rapid switching of the current in the coils would result in large reverse bias voltage spikes, well above the damage threshold of the solid-state relays. A usual solution to this problem, consisting of a flyback diode and resistor placed in parallel across each relay, results in lengthy switch off-times. This is mitigated with a tuned flyback protection circuit: for each relay a 200V 20A Schottky diode (D1) allows current to flow backwards without applying a large damaging voltage to the solid state relays. A 5Ω power resister and 130V Zener diode (D2) also allows the voltage to rise at switch off to provide faster power dissipation.

The current in the circuit after switching the H-bridge off can be modelled using Kirchhoff's Law:

$$V = -L\frac{dI}{dt} = I(t)R + V_D + V_z, \tag{4.3}$$

with $V_z(I) = \min\{V_{\text{rev}}, V_{\text{rev}} I / I_z\}$ where V_{rev} is the reverse voltage of the Zener diode, I_z is the Zener reverse current, L is the Coil inductance, R is the resistance of the power resister and V_D is the forward voltage of the Schottky diode.

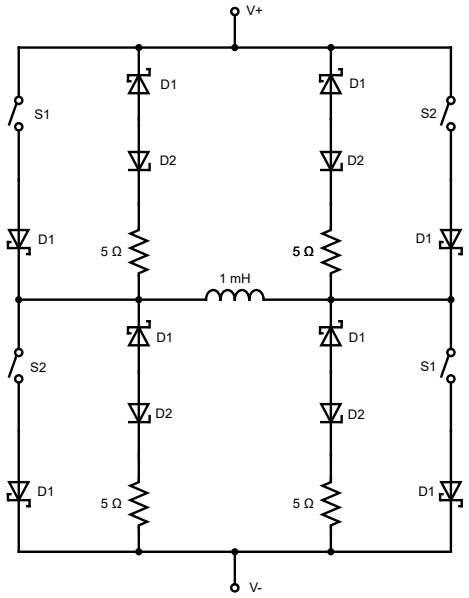

Figure 4.8: Circuit diagram of the H-bridge used to reverse the direction of current in one coil to enable both Helmholtz (S1 relays active) and anti-Helmholtz (S2 relays active) operation. S1/S2: Crydom D2D40 200V 20A solid state relay, D1: B20200G 200V 20A Schottky diode, D2: 1N5381B 130V 5W Zener diode. Due to the high current and voltages applied during rapid switching of the coils, all relays have flyback protection in the form of 5Ω power resister, 130V Zener diode and 200V 20A Schottky diode placed in parallel with the solid state relays. Additional Schottky diodes are placed in series with the relays to prevent current circulating inside the H-bridge out of loop with the precision low noise current driver.

For current monitoring, twin current transducers[6] were wrapped around the supply wire of each coil. Figure 4.9a shows the performance of the tuned H-bridge flyback protection circuit. Rapid switch off from 10A to 0A is achieved within 100 µs while keeping the voltage across the H-Bridge below 120V. Figure 4.9c shows the long dissipation time of a simpler implementation.

4.4.5 Precision Low Noise Current Driver

A custom built precision current driver is used to drive the main pair of coils in both their anti-Helmholtz quadrupole and Helmholtz bias field configurations. Although current drivers exist with either the precision required for our purposes [123], or the fast slew rates [124], achieving both is extremely difficult. Our current driver is capable of providing up to 16A with extremely low noise (1.5 µA) and drift (1 part in 10^6 RMS), while still achieving high slew rates (40A/ms) and fast settling times. The feedback loop is formed by using a current sensing shunt resistor and a series pass regular MOSFET.

The main current sensing element is a 0.1 Ω shunt resistor consisting of a folded

[6] Danfysik Ultrastab 867-60I current transducer.

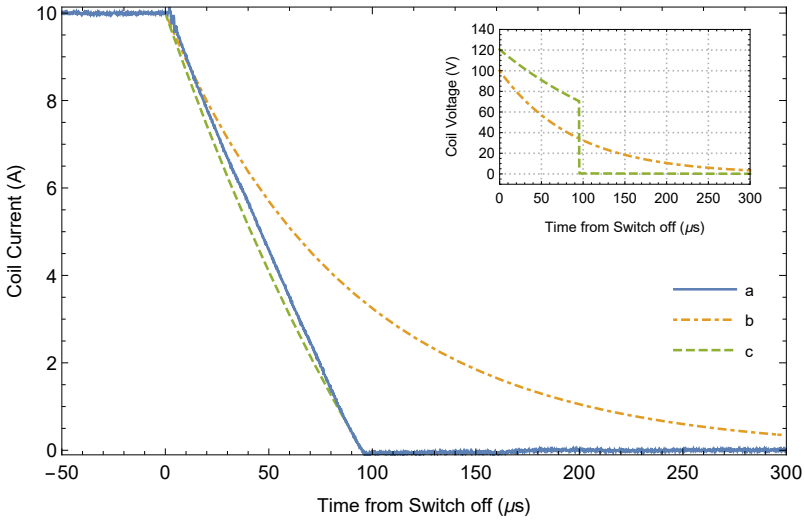

Figure 4.9: Measured current in the main trapping coils after switching off from 10A: a) Measured current, b) Theoretical current with only a power resister 5Ω, c) Theoretical current with power resister and 130V zener diode showing good agreement. Inset: Theoretical voltage across the solid state relays. With the flyback protection the voltage remains below the damage threshold of the Crydom D20D40 while still allowing rapid power dissipation and fast switch off times.

loop of resistive strip bonded to a 250mmx50mm aluminium substrate. Stray AC fields through the loop are cancelled ($<$ 1 in 10^7) with an additional loop on the substrate, wired in series anti-phase with the main loop. The resistor is temperature stabilised at 36 ± 0.1°C, where an inflection point exists in the temperature response of the resistor alloy which minimises $\frac{\partial T}{\partial t}$. The temperature lock is achieved using the aluminium mounting block's thermal mass to suppress fast temperature changes due to step changes in current, while active peltier modules eliminate slower ($>$ 1s) temperature drifts.

Current set points are provided by four digitally selectable analogue voltage inputs (1.6 A/V). In order to maintain stability despite input noise, three of the inputs are low-pass filtered with a 10 kΩ resistor and 5 µF capacitor, giving an RC time constant of 50 ms. The fourth input remains unfiltered, allowing fast changes in current. An additional fifth input, with fine control at 0.16 A/V is summed with the active main input to allow small fast changes in current around each low-pass filtered set point. Optically isolated TTL signals allow switching between each of the four set points, this enables switching between two precise low-pass filtered set points.

Although high current slew rates on the 1.8mH inductive load of the coils are easily achieved by using a high voltage supply (>100V), this would require a 2kW power supply at 16A. At constant driving current, due to the low resistance of the load coils, most of this power would need to be dissipated inside the series pass mosfet. Instead,

a low voltage (19V) supply is combined with a high voltage (140V) capacitive boost circuit. When a large current step is required, the boost circuit activates for a short period (<10ms) providing a current slew rate of 40A/ms.

The rapid switching ability of the combined H-Bridge and precision current driver is shown in Figure 4.10. With the coils operating in anti-Helmholtz configuration at 5 A the direction of one coil is switched using the H-Bridge. Within 130 µs the current in one coil has changed direction and a stable Helmholtz configuration is achieved.

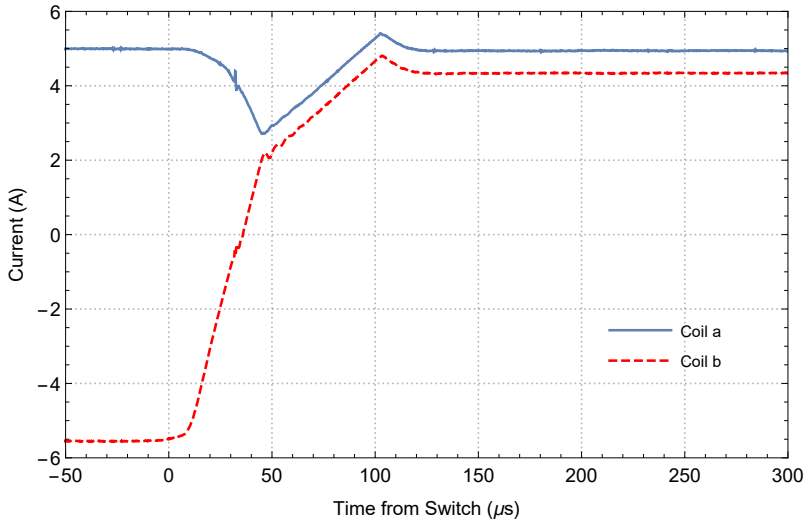

Figure 4.10: Measured current in the individual coils while switching from anti-Helmholtz to Helmholtz configuration at 5A using the custom H-Bridge. The 10A swing in current magnitude is completed and stablised within 130 µs. Note: a -0.5A offset is applied to Coil b for visual acuity.

4.4.6 Magnetic Shielding

The large magnetic compensation coils reduce the DC component of the Earth's magnetic field at the science cell, however no reduction in the time varying component is achieved. Sources such as power distribution lines, transformers, lighting, compressors and air conditioning can all contribute to a building's time-varying magnetic field, usually in the form of 50 Hz AC noise.

Initial attempts at using radio-frequency transitions on the ultra-cold atoms to calibrate the magnetic field in the centre of the optical trap gave large (>100mG) changes in the magnetic field, much larger than the noise expected due to limitations of the current driver. The background magnetic field, with the coils off, was measured by placing a three axis magnetic field sensor with 1.5 kHz bandwidth[7] as close as feasible

[7]Bartington Mag690-100μT three axis magnetic field sensor.

to the main glass cell. Data was logged on a Tektronix DPO 7054C oscilloscope for 500 s at a sample rate of 10 kS/s. The mean magnetic amplitude spectrum of the discrete Fourier transform of 1 s data segments is shown in Figure 4.11. The noise spectrum is dominated by 50 Hz AC noise and its associated harmonics. It is worth noting that if the control system (National Instruments PXI modules) for the experimental timings of each run was always synchronised to the mains AC cycle, then this noise source would be consistent run-to-run. However, this solution would only mask the noise, as the ^{85}Rb atoms would still see a time varying magnetic field, effectively broadening the scattering length control through the Feshbach resonance.

To achieve the necessary resolution for sub a_0 control over the ^{85}Rb scattering length through the Feshbach resonance, a reduction in room AC noise is required. Although active feedback control of the DC compensation coils to reduce AC noise is possible [125], it would require an array of six field sensors placed around the cell. Additionally, it is unclear how the active system would manage large (>100G) step changes in the magnetic field when rapidly switching the coils. A passive Mu-metal shield was instead implemented consisting of a removable Mu-metal box placed over the main coils and science cell. Access holes for optical beams were punched rather than drilled to avoid heating and subsequent reduction in the efficacy of the Mu-metal. Due to the shield being a retrofit to the system, large gaps such as where the pumping section of the vacuum chamber exists, are unavoidable. Nonetheless the shield achieves -9 dB attenuation at 50 Hz (Figure 4.11), sufficient to achieve sub a_0 control in the scattering length.

4.4.7 Feshbach Field Calibration

The accurate calibration of the magnetic field applied to the atoms inside the optical trap is crucial. Due to magnetic gradients across the volume of the glass cell, a field sensor placed nearby is insufficient. Instead, the ultra-cold atoms are themselves used as a probe by using radio-frequency waves to drive transitions between the Zeeman split m_F substates. Since our aim is to address the Feshbach resonance of ^{85}Rb, performing the calibration with this isotope would pose two problems. Firstly, the ^{85}Rb BEC is formed in the $|F = 2, m_F = -2\rangle$ state where inelastic losses are minimised [114]. RF transitions into the $m_f = -1$ state would induce rapid losses and heating. Secondly, at magnetic fields away from the Feshbach resonance, the background scattering length of $-440a_0$ prevents a stable ^{85}Rb condensate. For these reasons the calibration is performed with ^{87}Rb, taking advantage of the large available atom number.

A ^{87}Rb BEC held in the optical trap is driven between the $|F = 1, m_F = -1\rangle$ and

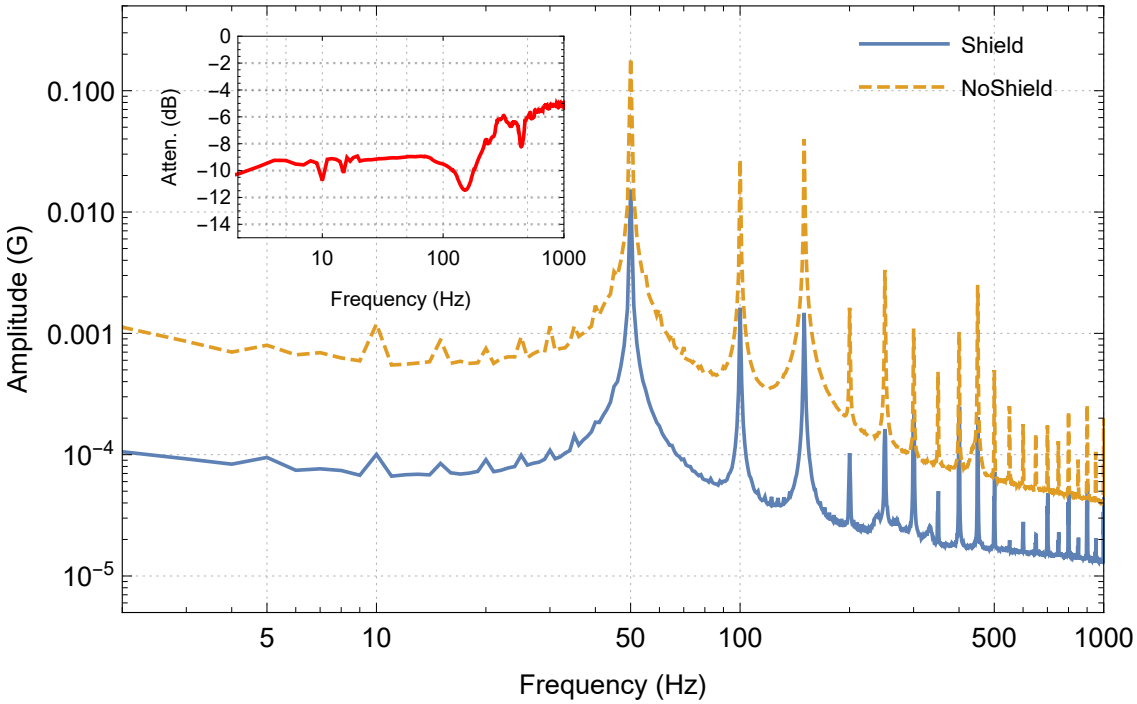

Figure 4.11: Amplitude spectrum of the magnetic noise close to the main science cell with and without the mu-metal shield. The noise floor of the Bartington Mag690-100μT sensor used was $2 \times 10^{-7}\,\mathrm{G}/\sqrt{\mathrm{Hz}}$ rms at 1 Hz. The addition of the shield provides -10 dB attenuation for <100 Hz noise sources, with -6 dB at higher frequencies. The dominant noise source is from 50 Hz mains power hum and it's harmonics; the maximum amplitude of 15mG corresponds to an error in the ^{85}Rb scattering length of $0.3a_0$.

$|F = 1, m_F = 0\rangle$ states by applying Gaussian pulses of RF radiation from a small coil placed inside one of the main magnetic cells. The 2ms long pulses are generated by a Moglabs Agile RF synthesizer providing accurate frequency and pulse shaping. The optical trap is then switched off and the atoms allowed to fall, during which the main coils are switched to anti-Helmholtz configuration. The magnetic gradient produced separates the two m_F states before they are imaged and relative populations measured.

The RF resonance for a particular magnetic coil current is found by sweeping the frequency of the pulse over many runs and fitting the peak transition position. The RF frequency is then related back to the magnetic field using the Breit-Rabi equation (Equation (2.76)) with parameters for ^{87}Rb given in Table 4.2. This is repeated for different current driver voltages, and as in Equation (4.1) a linear trend is found (Figure 4.12). After calibration, the uncertainty in the applied magnetic field is 5 mG corresponding to a scattering length uncertainty of $\pm 0.13a_0$ at the Feshbach zero crossing. The calibration was repeated at different times over a number of days and was found to be stable within the background magnetic noise except for a transient period after the machine began operation each day. This is most likely due to the coil mount heating and expanding while

Property	^{85}Rb	^{87}Rb
I	5/2	3/2
g_J	2.002 331 13(20)	
g_I	−0.000 293 640 00(60)	−0.000 995 141 4(10)
A_{hfs}/h	1.011 910 813 0(20) GHz	3.417 341 305 452 145(45) GHz

Table 4.2: Values for the ^{85}Rb and ^{87}Rb electronic groundstate energy splitting calculation (Equation (2.76)) [102].

reaching an equilibrium temperature. For aluminium, the fractional expansion rate is $24 \times 10^{-6}\,^{\circ}\mathrm{C}^{-1}$, which for a coil spacing of 51 mm in Equation (4.1) gives a change in the field at 165G of 3.8 mG/C, easily accounting for this transient behaviour during warm up.

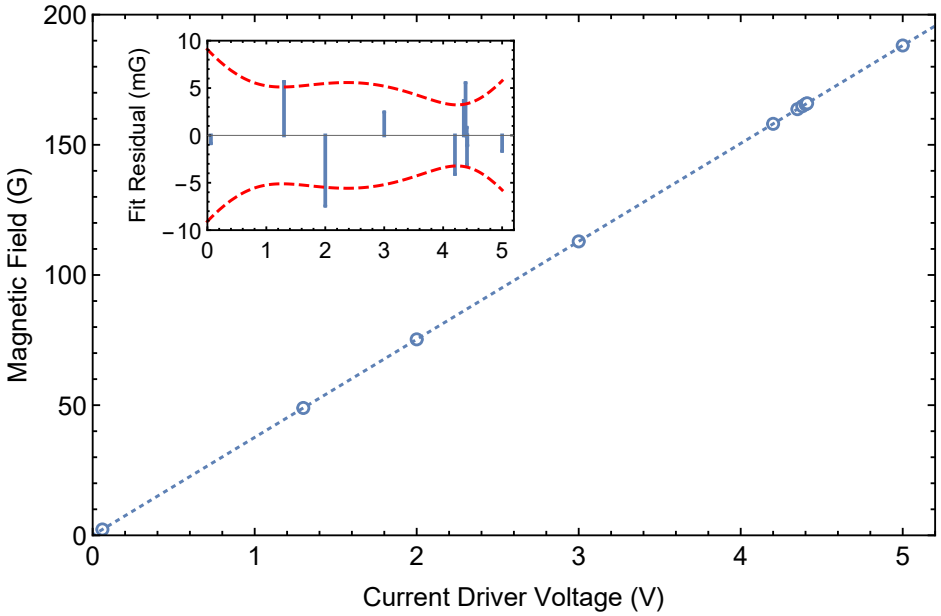

Figure 4.12: Calibration of the current source and magnetic field produced by the Helmholtz coils. Inset: Residue of the fit with 90% confidence bands. Extra data points were taken around the zero crossing of the ^{85}Rb Feshbach resonance to well categorise the scattering length. The ∼5 mG residue corresponds to $0.13a_0$ uncertainty at the zero crossing.

4.5 Optical Trap

The creation of ^{85}Rb condensates with large atom numbers ($> 10^5$) requires a large DC magnetic bias field (165 G) to access the Feshbach resonance and create favourable scattering lengths for evaporation. Although an additional bias field could be applied to the magnetic trap to reach the resonance, the field gradient produced in a magnetic trap would create a region of varying scattering length across the condensate. Instead, the

atoms are loaded into an optical dipole trap. The trap is formed by combining a Gaussian and Bessel laser beam at 1064 nm and 1090 nm, respectively, intersecting at 30° with waists of 90 µm and 150 µm (shown in Figure 4.4). The shallow intersection allows for a greater total trap volume which results in increased mode matching from the magnetic trap.

4.5.1 Optical Potential

Although one of the trapping beams is a non-diffracting Bessel beam (over the length of the glass cell), we can still treat the central lobe as approximately Gaussian for short distances from its waist. The optical potential can be well modelled by the analytical form of the electric field of a Gaussian laser beam given in Equation (2.34).

As our potential is formed from unpolarised lasers with wavelengths differing by 30nm, effects due to interference and phase will not be present so we can simplify this to the intensity profile:

$$I_{\text{Gaus}}(x,y,z) = \frac{2P}{\pi\omega(z)^2}\exp\left(-\frac{2\left(x^2+y^2\right)}{\omega(z)^2}\right). \tag{4.4}$$

Since we have an intersection angle of $\alpha = 30°$, we rotate the coordinate system for one beam $\{x\cos\alpha + z\sin\alpha, y, z\cos\alpha - x\sin\alpha\} \rightarrow \{x', y', z'\}$. The dipole potential for each laser is given by [87]:

$$U_{\text{dip}}(x,y,z) = -\frac{3\Gamma\lambda^2\lambda_0^4}{16c^2\pi^3(\lambda^2-\lambda_0^2)}I(x,y,z), \tag{4.5}$$

where Γ is the spontaneous decay rate of the excited level, λ_0 is the transition wavelength and λ is the laser wavelength.

The total trapping potential, including gravity is:

$$U_{\text{trap}}(x,y,z) = -mgy + U_{1064}(x,y,z) + U_{1090}(x',y',z'). \tag{4.6}$$

Here we have defined $\hat{y}$ to be the direction of gravity in order to remain consistent with the usual coordinates for cigar shaped traps where the axial trapping direction is $\hat{z}$.

The resulting optical trap is shown in Figure 4.13 for the optical powers after condensation to BEC is complete. It is crucial to include the gravitational potential in the full model as the increased sag causes a limit to the depth of the trap. This manifests as a leak at the lowest point in the trap and is dependent on the atomic mass. Depending on the laser parameters, the 2% difference in the mass of ^{85}Rb and ^{87}Rb can result in signif-

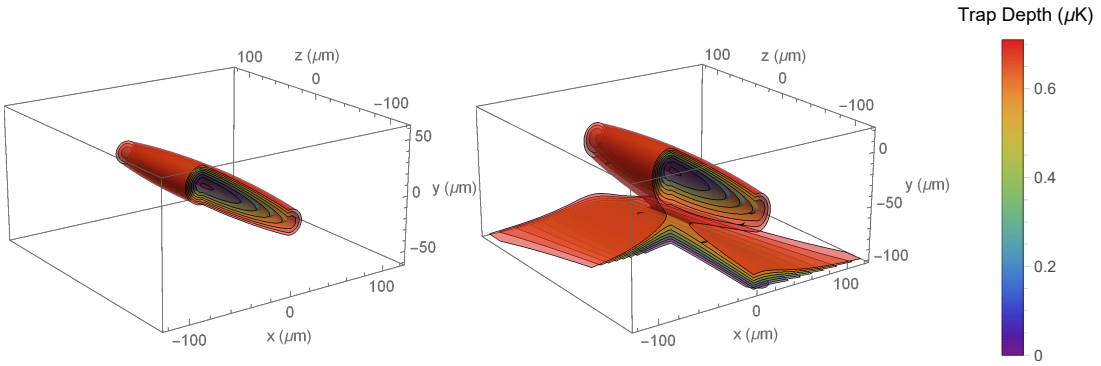

Figure 4.13: Optical trap potential showing the effect of gravity. Each colour is a surface of constant potential. Left: Without gravitational sag. Right: With gravitational sag the trap depth is decreased by a hole through the bottom of the trap, additionally the trap centre is displaced by 27 µm.

icant differences in trap depth, position and trapping frequencies (Figure 4.14). During the final stages of optical evaporation, the lower trap depth of ^{87}Rb allows it to be preferentially removed from the system. Complete removal of ^{87}Rb atoms can be achieved by lowering the trapping power until there is no trapping potential remaining.

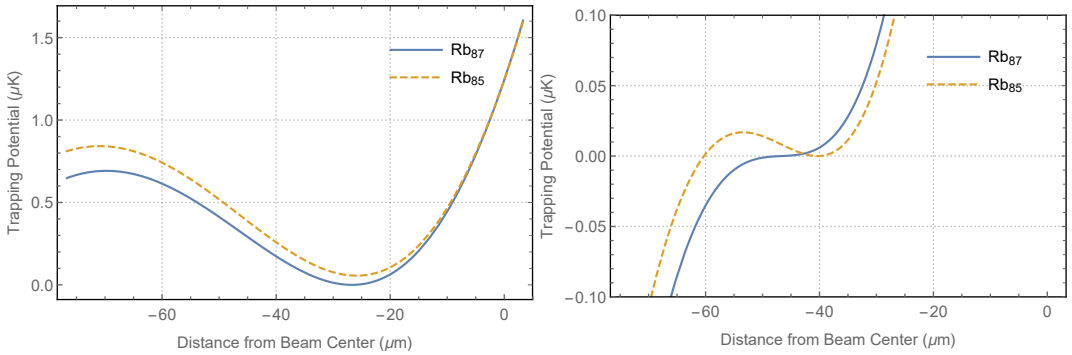

Figure 4.14: Plot of the analytical optical trap potential in the vertical direction. Left: For trapping laser powers 0.76 W and 0.39 W both isotopes are trapped. The gravitational sag creates a trap offset of 27 µm. The trap depth is slightly lower for ^{87}Rb allowing it to be preferentially evaporated from the trap. Right: For sufficiently low trapping powers (0.6 W and 0.39 W), ^{87}Rb is no longer trapped allowing it to be preferentially removed. Under these conditions the trap potential is anharmonic, after evaporation is complete the trap powers are adiabatically increased into the harmonic regime.

4.5.2 Trapping Frequencies

For deep optical traps, the trapping potential can be approximated as harmonic (Equations (2.47) and (2.40)) and the full analytical model in Equation (4.6)) provides numerical estimates of the trapping frequencies for different powers and configurations. An experimental measurement is desirable due to the comparatively large errors in measuring the laser power in the focused Gaussian spot inside the main science cell.

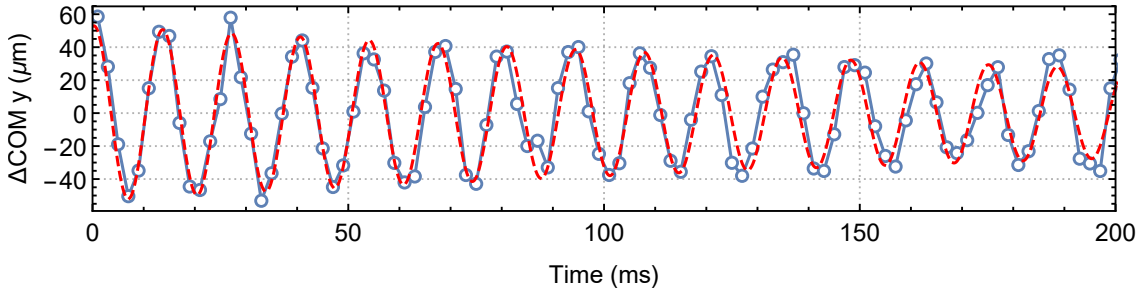

Figure 4.15: Measurement of the vertical COM oscillation for a ^{87}Rb BEC. Open circles are individual experimental runs. The fitted sinusoid gives the trapping frequency of $\omega_x = 2\pi \times (74.6 \pm 0.5)$.

This can be made with several methods such as parametric heating [114], however, here we use the excitation of centre-of-mass (COM) and collective mode oscillations in the BEC to make a direct measurement of the harmonic trap.

To excite these motional modes, a BEC of either pure ^{85}Rb or ^{87}Rb BEC is produced in the optical trap. The optical trap powers are then adiabatically ramped up to ensure the anharmonicty of the optical trap is minimised. The trapping power in the axial beam is then pulsed higher for 1ms and due to the gravitational sag in the trap, this generates an upward force on the BEC exciting the COM mode. The BEC is then allowed to freely oscillate for different times before the trap is switched off and the cloud is imaged. The frequency of the COM oscillation is then fitted to give the trapping frequency (Figure 4.15).

Measuring the trap frequency in the axial direction is more subtle due to the lack of any broken symmetry that can apply a COM kick. Instead, a collective quadrupole oscillation is excited by momentarily switching off the transverse trapping beam. This allows the BEC to expand in the axial direction before the beam is switched back on. This non-equilibrium state then oscillates inside the trap. The frequency of the excited quadrupole mode can be directly related to the trapping frequency. For our cigar-shaped trap geometry this relation is given by [103]:

$$\omega_{\text{quad}} = \sqrt{5/2}\omega_z. \tag{4.7}$$

The quadrupole excitation frequency can be extracted by measuring the width of the condensate for different hold times, however a more robust solution is the use of principal component analysis (PCA) (see Section 3.3). PCA allows different excitation modes to be distinguished as well as the extraction of their frequency and corresponding eigenfunction [110]. Figure 4.16 shows the largest four eigenvectors extracted from PCA when applied to images of different hold times after excitation. The eigenvectors

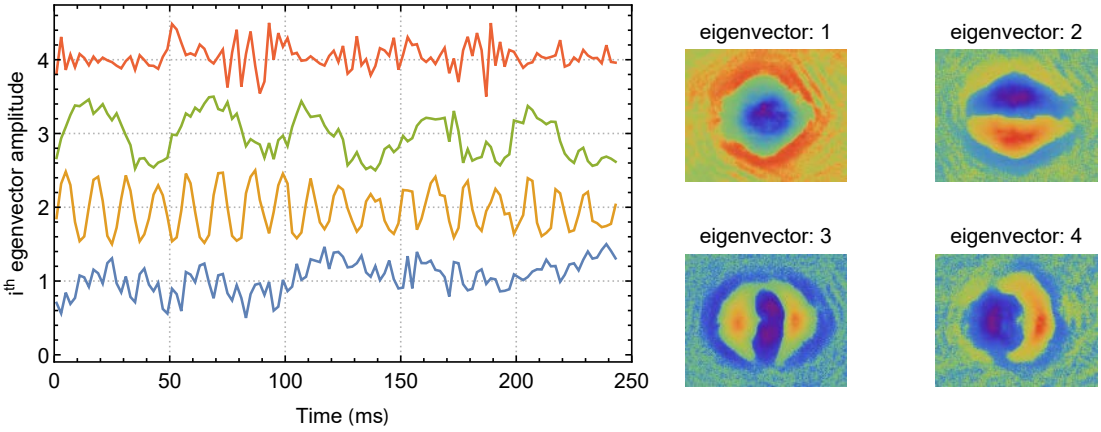

Figure 4.16: The result of principal component analysis of an excited ^{87}Rb BEC. The first four eigenvectors are shown, ordered by decreasing eigenvalue (corresponding to the amount of image variance accountable to each). The normalised amplitude of the projection of each mode onto each experimental image is plotted against the trap hold time (offset vertically for each eigenvector). Eigenvector 1: Atom number variation corresponding run-to-run fluctuations of atom number as well as increasing loss from extended hold times (note that PCA does not presuppose a sign to the eigenvectors, so here loss is indicated by an *increasing* amplitude). Eigenvector 2: Vertical COM oscillation excited as a byproduct of the method used to create the quadrupole mode. The fitted frequency of 74.8(1) Hz is in agreement with the direct measure in Figure 4.15. Eigenvector 3: Quadrupole excitation mode, with fitted frequency 20.7(1) Hz. Eigenvector 4: Axial COM mode, due to a lack of broken symmetry this excitation is too small to directly extract a frequency.

correspond to atom number fluctuations, vertical COM mode, quadrupole collective mode, and axial COM mode. The fitted frequency of $2\pi \times (74.8 \pm 0.1)$Hz for the vertical COM mode is in agreement with the previously measured value. The fitted frequency of the quadrupole excitation mode ($2\pi \times (20.7 \pm 0.1)$Hz) substituted into Equation (4.7) gives a calculated axial trapping frequency of $2\pi \times (13.1 \pm 0.1)$Hz.

Multiple measurements of both the axial COM mode and the quadrupole mode for each isotope were taken, with the final values of the calculated trapping frequencies given in Table 4.3.

While the imaging line (shown in Figure 4.4) is placed horizontal and perpendicular to the axial axis of the optical trap, and can make direct measurements of both the axial and vertical trapping frequencies, there is difficulty in measuring the final trapping axis. Although in principle a breathing mode could be excited in this direction, the resulting signal is small due to the column integrated imaging. Instead the analytical model (Equation (4.6)) of the optical trap is used, along with the previous measurements, to determine this final frequency. This is achieved through a statistical process of bootstrapping.

For most parameters in the analytical model, including laser frequency, waist size

	$\omega_x/2\pi$ (Hz)	$\omega_y/2\pi$ (Hz)	$\omega_z/2\pi$ (Hz)
^{85}Rb	104.4 ± 0.5	78.1 ± 0.5	13.2 ± 0.5
^{87}Rb	103.3 ± 0.5	74.6 ± 0.5	13.1 ± 0.2

Table 4.3: Trapping frequencies of the optical trap for each isotope. The values for ω_y and ω_z were experimentally measured. The values for ω_x were found through a process of bootstrapping the analytical potential model.

and crossing angle, the values are well defined with the largest parameter error entering through the trapping laser powers. To utilise the model we begin by taking a random statistical sample of the axial and vertical trapping frequencies, using the measured error for the variance of their distribution. The power in each modelled trapping beam is then allowed to vary such that the errors between the fitted trapping frequencies from the model (ω^*) and the sampled experimental values are minimised. Specifically, the cost function combining the error in all four measured trapping frequencies is:

$$f(P_{1090}, P_{1064}) = \frac{(\omega^*_{85,z} - \omega_{85,z})^2}{\omega^2_{85,z}} + \frac{(\omega^*_{85,y} - \omega_{85,y})^2}{\omega^2_{85,y}} + \frac{(\omega^*_{87,z} - \omega_{87,z})^2}{\omega^2_{87,z}} + \frac{(\omega^*_{87,y} - \omega_{87,y})^2}{\omega^2_{87,y}}, \tag{4.8}$$

where P_{1090} and P_{1064} are the powers of the two trapping beams. The laser powers which minimise $f(P_{1090}, P_{1064})$ are then used to extract a corresponding value of $\omega_{85,x}$ and $\omega_{87,x}$ from the model. Repeating this process for many samples of the axial and vertical trapping frequencies allows a distribution of possible $\omega_{85,x}$ and $\omega_{87,x}$ trapping frequencies to be calculated. The final mean and variance are given in Table 4.3.

The nature of our optical trap is such that the tight axis beam (90 µm) provides most of the trapping force, while the weaker beam simply closes the axial sides of the trap. Under this model, Equation (2.47) can be used to analytically estimate the effect of gravitational sag on trapping frequencies. These values are commensurate with those found in Table 4.3, but underestimate the error as they do not consider the full parameters of the model.

4.5.3 Bessel Waveguide

Using one Bessel beam to form the crossed optical trapping potential was motivated by its low axial divergence, which creates an ideal optical waveguide. Discussed in Section 2.2, theoretical non-diffracting Bessel beams can only be formed with an infinite amount of energy, however they can be approximated over short distances by passing a Gaussian beam through an axicon lens [89]. The particular choice of input beam diameter and axicon angle gives a trade off between the non-diffracting distance (f_2), the waist of the central lobe (r_0) and the fraction of power in the central lobe (P_0/P). The width of the central Bessel lobe, r_0, is set by the axicon cone angle α, not the waist of the input Gaussian

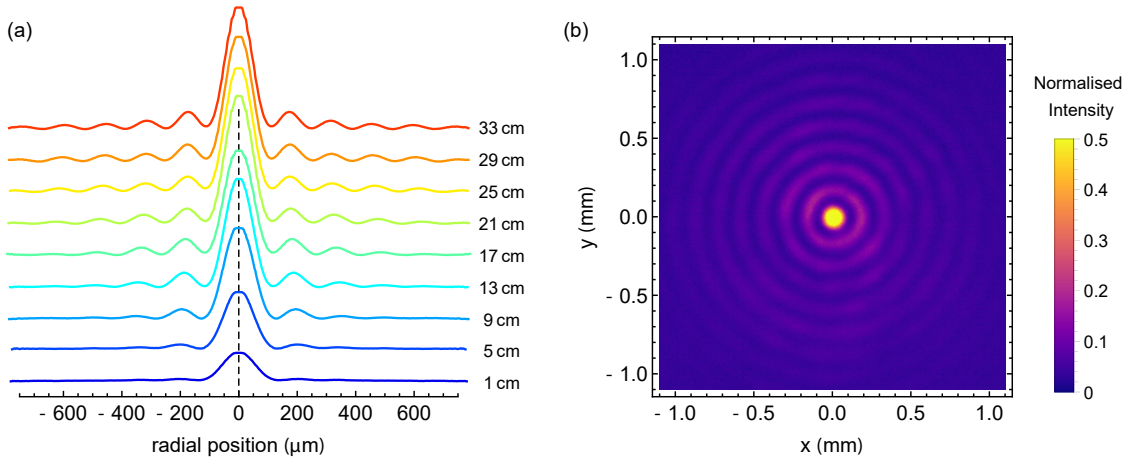

Figure 4.17: Experimental Bessel beam profiles. a) Radial intensity (mirrored around $r = 0$) of the Bessel beam as a function of distance from the axicon. b) Image of Bessel beam intensity at the optical trap center (25 cm from the axicon).

beam. To first order in α:

$$r_0 = 2.4\frac{\lambda}{2(n-1)\pi\alpha}. \tag{4.9}$$

Unintuitively, it is the length of the non-diffracting region (f_2) which is dependent on the input beam size. To first order in α:

$$f_2 = \frac{D}{(n-1)\alpha}. \tag{4.10}$$

For a given choice of α, f_2 can be made arbitrarily large by increasing D. However as D is increased, the intensity of the central lobe decreases with the inverse:

$$I(r = 0, z = f_2) = \frac{4(n-1)\pi\alpha}{D\lambda\sqrt{e}}. \tag{4.11}$$

The Bessel beam here is formed by passing a Gaussian beam with 600 μm waist (D =1200 μm) through an axicon lens with cone angle 0.5° and refractive index $n = 1.458$. The calculated first Bessel zero is $r_0 = 101$μm with non diffracting length $f_2 = 30$cm. Figure 4.17 shows the intensity of the beam as a function of distance from the axicon. The theoretical treatment over-estimates the fitted Bessel waist of 95 μm, most likely due to not including the Gaussian beam propagation and waist location. Figure 4.18 shows a comparison between a theoretical Gaussian beam and the experimental Bessel beam with similar waists. The Bessel beam maintains its waist over a much longer region.

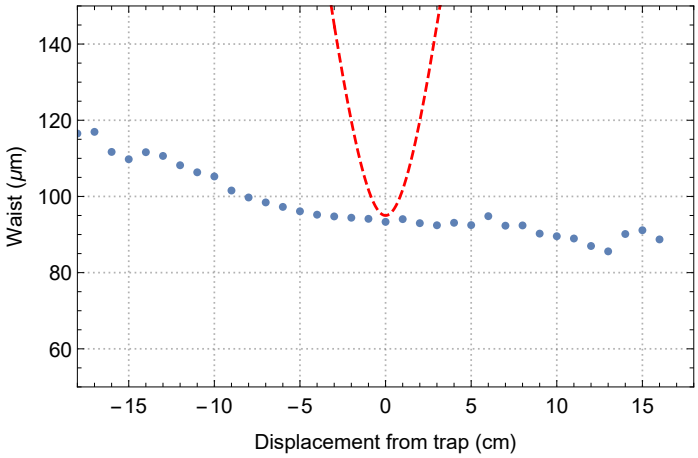

Figure 4.18: Waist of the Bessel beam as a function of axial displacement from the (approximate) optical trap centre. The red dashed line indicates the theoretical waist of a Gaussian beam. The Bessel beam achieves much greater flatness.

4.6 Dual Species BEC

The experimental procedure for creating condensates is similar to previous iterations of the dual species ^{85}Rb/^{87}Rb apparatus given in [115, 116]. Improvements, both in terms of stability and optimisation of each stage of the preparation scheme, have dropped the duty cycle from 23 s down to 13 s. The same optimisations have increased the size of the condensates produced by nearly an order of magnitude compared to [115], creating stable condensates with atom numbers $N_{85} = 2 \times 10^5$ and $N_{87} = 3 \times 10^6$ for ^{85}Rb and ^{87}Rb respectively.

Initially, a red detuned (-9 MHz) push beam loads the 3D MOT through the vacuum impedance from the 2D MOT source. After 5 s of loading the 3D MOT contains up to $N_{85} = 6 \times 10^8$ and $N_{87} = 3.6 \times 10^9$ atoms. Due to the large heat load imposed by the ^{85}Rb atoms the relevant push beam is only switched on for the final 1 s of loading, with shorter times allowing the final BEC mixture to be controlled.

After loading, the 2DMOT magnetic field is switched off to minimise the field gradients across the 3DMOT side of the chamber. Simultaneously, the magnetic gradient from the 3D coils is dropped from 18 G/cm to 12.5 G/cm and the trapping light is detuned further from -15 MHz to -25 MHz. This step compresses the 100 µK cloud over 30 ms, allowing better mode matching when loaded into the tight magnetic quadrupole trap. Polarisation gradient cooling, as described in [126], is then applied. Over 15 ms the trapping light detuning is ramped to -76 MHz while the magnetic gradient is reduced to zero. Due to the laser source setup, the trapping light detuning is common to both isotopes. In order to individually optimise the PGC step, the repumping lights of ^{85}Rb

and ^{87}Rb are detuned to -8 MHz and -3 MHz, respectively. The repumping light is then switched off for 2 ms to allow all atoms to decay into the $|F = 2\rangle$ and $|F = 1\rangle$ dark states of ^{85}Rb and ^{87}Rb, respectively, before all remaining MOT light sources are switched off. At this point the temperature of the cloud is typically 25 µK.

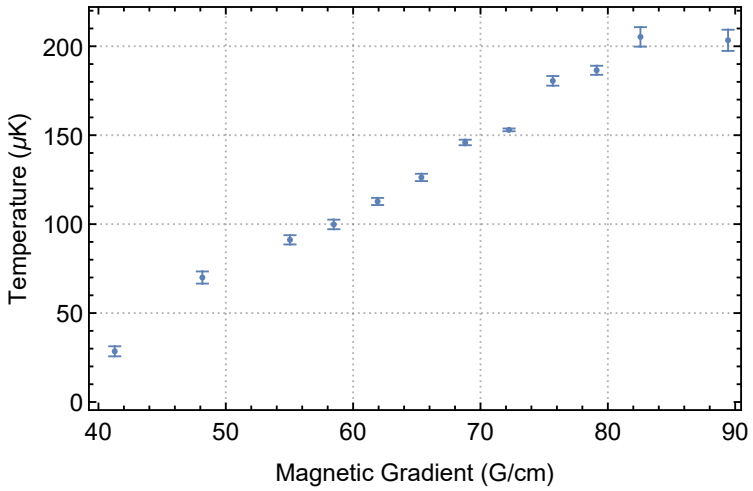

Figure 4.19: Temperature of ^{87}Rb atoms after initially loading the magnetic trap for different magnetic gradients.

The atoms are then caught in the magnetic trap by rapidly (<100 µs) switching on the quadrupole field. The field gradient is initially set to 55 G/cm, which allows maximal capture of atoms ($N_{87} = 1.8 \times 10^9$) while reducing the amount of heating (Figure 4.19). Over 100 ms the gradient is ramped to 110 G/cm, increasing the rethermalisation rate due to collisions, while only heating the cloud to 120 µK. The two optical dipole beams are also ramped on over 200 ms, serving both to increase the collision rate at the centre of the trap, as well as mitigate atom losses due to spin flips in the zero field region [127]. The trapped atoms, now in the trapped Zeeman states ($|F = 2, m_F = -2\rangle$ and $|F = 1, m_F = -1\rangle$ for ^{85}Rb and ^{87}Rb, respectively), undergo forced evaporative cooling by driving RF transitions into the untrapped states. For a quadrupole magnetic field, the trapping frequency can be found from the field curvature:

$$\omega_z^2 = \frac{\mu_B g_F m_F}{m_{85}} \frac{\partial^2 B}{\partial z^2}, \tag{4.12}$$

where μ_B is the Bohr Magneton, g_F is the Landé g factor, m_{85} is the mass of ^{85}Rb and m_F is the Zeeman state. Atoms with higher velocities occupy regions further from the trap centre, and hence experience higher B values in the quadrupole magnetic field. The Zeeman splitting between states is given by:

$$\omega = \frac{\mu_B \left| g_F \right| B}{\hbar}. \tag{4.13}$$

Tuning the RF field allows hot atoms to be preferentially removed with the cloud continually rethermalising due to scattering collisions. Over 5 s, the RF frequency is swept from 18 MHz to 1 MHz. The evaporation is isotope selective, predominantly removing ^{87}Rb as its larger Landé g factor ($g_F = -1/2$ and $g_F = -1/3$ for ^{87}Rb and ^{85}Rb respectively) spatially locates the RF knife closer to the centre of the trap. Additionally, the ^{85}Rb atoms occupy the $m_F = -2$ state compared to $m_F = -1$ for ^{87}Rb, resulting in a tighter trapping frequency ($\omega^2_{z,85} = 1.36\omega^2_{z,87}$) causing the ^{85}Rb atoms to be located at lower magnetic fields for equivalent temperatures. Over the last 1.5 s of RF evaporation, the magnetic field gradient is reduced to 27 G/cm, leaving a cloud of $N_{87} = 5 \times 10^7$ at 10 µK.

Magnetic evaporation could continue, however at these temperatures the sympathetically cooled ^{85}Rb atoms begin to undergo inelastic collision losses due to their large background scattering length. Instead, the atoms are transferred into the optical trap, allowing the scattering length of ^{85}Rb to be set with the Feshbach resonance. The switch from the quadrupole magnetic field to the high field positive scattering regime must be done rapidly to minimise three body recombination through the centre of the Feshbach resonance (Figure 3.2) [128]. The rapid switching is achieved with the custom designed current driver and H-bridge discussed in Section 4.4.

The quadrupole field is first switched off and allowed to dissipate before the H-bridge reverses the direction of current in one coil. The field is then rapidly increased to 165 G, setting the ^{85}Rb self-scattering length to $80a_0$, with the atoms supported in the crossed optical dipole trap. The H-bridge switch process is completed in 130 µs, both reducing the zero-field time where spin flips can occur and minimising three body losses from passing through the 155 G Feshbach resonance.

Typically, the transfer into the optical trap loads a $N_{87} = 3 \times 10^7$ cloud at 5 µK and up to $N_{85} = 5 \times 10^6$, though typically the ^{85}Rb number is set lower by reducing the initial MOT loading time. Although the ^{85}Rb scattering length could be set to zero for optimal sympathetic cooling, as BEC is approached the clouds become immiscible preventing further sympathetic evaporation. Instead we set $a_{85,85} = 80a_0$, below that of ^{87}Rb in order to preferentially rethermalise through inter-isotope collisions while still allowing evaporation once a BEC is formed. To evaporatively cool in the optical trap, the powers in each beam are reduced over 2.5 s following an exponential decay. Pure

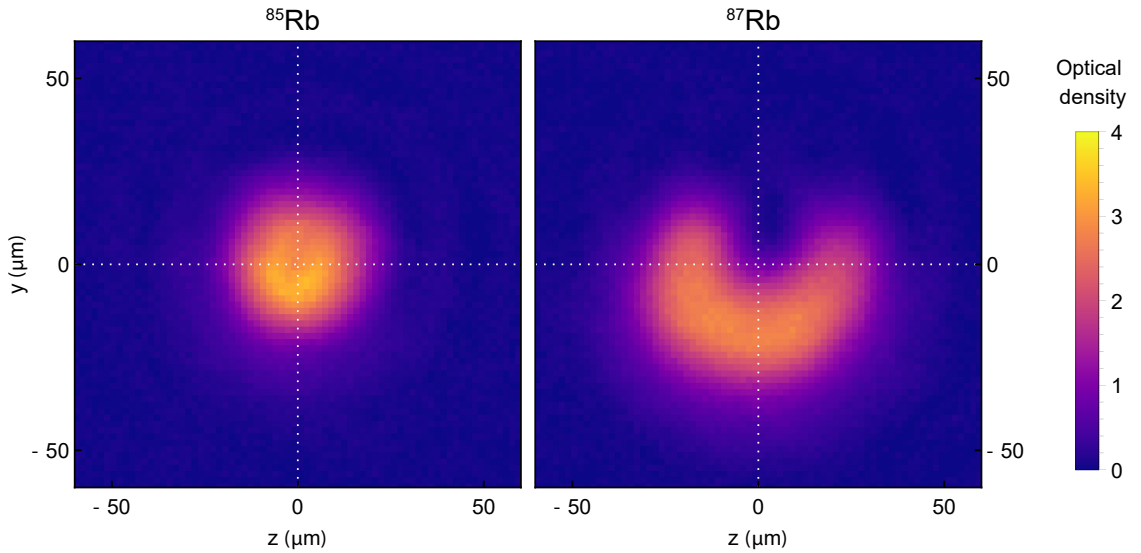

Figure 4.20: Dual species BEC imaged after 20 ms of free expansion. Due to the mass difference between ^{85}Rb and ^{87}Rb, the immiscible clouds separate vertically, a key signature that condensation has been achieved.

BECs are formed with up to 2×10^5 and 5×10^6 ^{85}Rb and ^{87}Rb atoms respectively. Mixed species BECs are formed at lower atom numbers, as the immiscibility of the condensates prevents efficient sympathetic cooling.

Figure 4.20 shows a typical dual species condensate imaged after 20 ms of expansion after the optical trap was switched off. The immiscibilty of the two isotopes is a clear signature of condensation into a BEC. The nature of these mixed BEC groundstates is investigated in detail in Chapter 6.

4.7 Outlook and Future Work

We have presented a dual-species BEC machine capable of creating up to 2×10^5 and 2×10^6 condensates of ^{85}Rb and ^{87}Rb, respectively, as well as isotope mixtures. The apparatus described here was designed to be highly configurable for ongoing single and dual component experiments. Several improvements over previous designs were made, achieving greater stability, more accurate control and larger atom numbers. The repetition rate of the machine was reduced from $\sim$23 s to 13 s while also increasing the size of BECs compared to similar previous designs which incorporated a single, dual-use main coil [115]. The use of an ultra-precise current driver, combined with additional magnetic shielding, allowed the accurate calibration of the Feshbach resonance of ^{85}Rb. We are able to control the intra-species scattering length with an uncertainty of $\pm 0.13 a_0$, suitable for a range of non-linear experiments. An accurate model of the optical potential, with experimental measurements of trapping frequencies allows the system to

be well simulated by numerical GPE simulations.

In Chapter 5 a previous iteration of the dual-species machine is used to make an observation of modulational instability in a BEC. The improvements made to the experimental apparatus allow detailed studies into many new aspects of non-linear phenomena. For instance, the optical system design easily allows the future addition of a reconfigurable potential with a spatial light modulator (SLM) or digital micromirror device (DMD). This will open avenues to investigate seeded instabilities, where applied perturbations seed the growth dynamical instabilities, as well as a range of real time tunnelling experiments [37, 129]. Furthermore, the replacement of the previous Gaussian optical trap with a non-diffracting Bessel beam increases the length over which atoms may be guided, greatly increasing the space-time area of atom interferometers [115, 122].

In Chapter 6 we use the apparatus to make a detailed study of phase separated groundstates. The high degree of calibration and control over the machine allows us to study the shape of the interface between immiscible condensates, and we demonstrate reliable production of a range of interface curvatures. The numerous upgrades to the apparatus in terms of stability, repetition rate, condensate size and imaging access were essential for this work.

This apparatus will act as an indispensable test bed for future experiments in dual component condensates, non-linear stability, optically guided atoms, non-destructive observation of quantum tunnelling and feedback cooling.

Part III

Controlling Atom Interactions

Chapter 5

Modulational Instability in Bose-Einstein Condensates

The following chapter presents work summarised in the following two publications:

- ***P. J. Everitt**, M. A. Sooriyabandara, M. Guasoni, P. B. Wigley, C. H. Wei, G. D. McDonald, K. S. Hardman, P. Manju, J. D. Close, C. C. N. Kuhn, S. S. Szigeti, Y. S. Kivshar, and N. P. Robins. Observation of Modulational Instability in Bose-Einstein Condensates. Physical Review A **96**, 041601 (2017).* DOI*: 10.1103/PhysRevA.96.041601.*

- *P. B. Wigley, **P. J. Everitt**, K. S. Hardman, M. R. Hush, C. H. Wei, M. A. Sooriyabandara, P. Manju, J. D. Close, N. P. Robins, and C. C. N. Kuhn. Non-destructive shadowgraph imaging of ultra-cold atoms. Optics Letters **41**, 4795 (2016). ISSN 1539-4794.* DOI*: 10.1364/OL.41.004795.*

I led the investigation in the first publication, including building the imaging system, performing the experiment and analysing the experimental data; all NPSE simulation data was taken by M. A. Sooriyabandara. In the second publication, I developed the imaging system on the dual-species apparatus, performed dual species evaporation and single species dynamical experiments. The theoretical and experimental analysis techniques were developed jointly with P. B. Wigley.

Intensity-dependent instabilities are a dramatic manifestation of the strong nonlinear effects that can occur in nature, and they are observed throughout physics as the development of spatial or temporal modulations with growing amplitudes. *Modulational instability* (MI) is a well-known phenomenon in optics which manifests itself as a decay of long optical fibre signals into pulse trains [60, 62, 63]. MI is a general wave phenomenon that occurs when a weak perturbation to a waveform is enhanced by nonlinearity, giving rise to sidebands in the spectrum with subsequent modulation growth and the formation of a train of spatially or temporally separated solitary waves [53].

Solitary matter-waves of a different origin have been extensively studied in Bose-Einstein condensates (BECs), where interatomic interactions give rise to strong

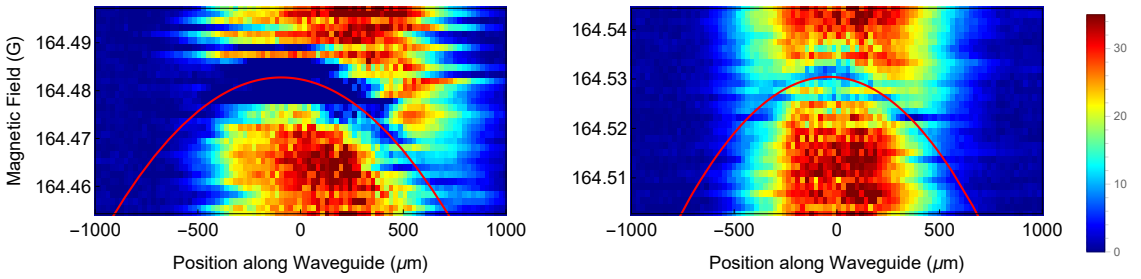

Figure 5.1: RF transition resonance across the waveguide. The fitted magnetic field ($B_{wg}(x)$)is shown in red a) Prior to adjustment the optical trap center is offset from the magnetic minimum. b) Adjusting the dipole trap position along the waveguide allows the optical center and magnetic center to align. The magnetic curvature is measured to be $107(1)\,\mathrm{mG/mm^2}$.

nonlinearities. In particular, soliton trains in BECs have previously been observed in ^{7}Li condensates with attractive interactions loaded into highly anisotropic traps [67]. The formation of multiple solitary waves has also been observed during collapse of Rb condensates [130]. Recently, BEC solitons have been employed for the first realization of a solitonic atom interferometer [122]. Despite theoretical predictions [131, 132], the stochastic nature of many nonlinear processes, combined with traditionally destructive methods of BEC imaging, has impeded the direct observation of more subtle nonlinear effects.

In this chapter, we present real-time observations of MI in BECs. Using nondestructive *in situ* imaging, we are able to image a single BEC placed in an optical waveguide as it undergoes the transformation into a train of spatially localized components. We show that the number of localized components observed after the breakup is consistent with an MI analysis conducted in the framework of the nonpolynomial Schrödinger equation (NPSE) [133], suggesting that MI is the underlying physical mechanism driving the observed breakup. This work was carried out on a previous iteration of the dual species apparatus, best summarised in [115].

5.1 Feshbach Resonance Calibration

The experiments here are conducted in an optical cross trap consisting of intersecting 1090 nm and 1064 nm laser beams with approximate waists of 300 µm and 250 µm (halfwidth at $1/e^2$ intensity), respectively. A bias magnetic field over the extent of the cloud is generated with a pair of Helmholtz coils. This allows the s-wave scattering length of the cloud, a_s, to be tuned utilizing the Feshbach resonance. Crucial to the formation and control of ^{85}Rb clouds is precise knowledge of this applied magnetic field.

In order to calibrate the magnetic field values along the waveguide, a ^{87}Rb BEC is loaded into the optical waveguide and allowed to expand along its length. A 1ms pulse of radio frequency waves is then used to drive a transition between the $m_F = -1$ to $m_F = 0$ states, which are separated due to Zeeman splitting. Sweeping through a range of frequencies allows the magnetic field as a function of space to be precisely probed. Figure 5.1 shows the atoms remaining in the $m_F = -1$ state spatially along the waveguide for each frequency pulse (converted to magnetic field). The atoms remaining as a 2D function of position and magnetic field is given by:

$$f(x, B) = Ae^{\frac{(x-x_0)^2}{(2\sigma^2)}} \left(1 - e^{\frac{-(B-B_{wg}(x))}{2\sigma_B^2}}\right), \tag{5.1}$$

where $B_{wg}(x) = B_0 - \frac{\kappa}{2}(x - x_B)^2)$ is the magnetic field along the waveguide, x_0 is the center of the cloud, σ_0 is the width of the cloud, x_B is the center of the magnetic trap, B_0 is the value at the center of the magnetic trap, σ_B is the width of the rf pulse, A is an arbitrary scale factor and κ is the magnetic curvature ($\frac{\partial^2 B}{\partial x^2}$).

If misaligned, the optical trap, located at the centre of the cloud, and the magnetic trap centre are not co-incident (Figure 5.1a). Careful adjustment of the optical cross beam moves the optical trap into alignment with the magnetic trap (Figure 5.1b). The residual magnetic curvature, $\frac{\partial^2 B}{\partial x^2} = 107(1)\,\mathrm{mG/mm^2}$, results in a repulsive potential along the guide according to the relation $\omega_z^2 = \mu_B g_F m_F / m_{85} \frac{\partial^2 B}{\partial x^2}$, where μ_B is the Bohr Magneton, g_F is the Landé g factor and m_F is the MF state. This gives an imaginary anti-trapping frequency of $\omega_z = 2\pi i \times 3\,\mathrm{Hz}$.

5.2 Imaging

To monitor the cloud dynamics two orthogonal imaging systems are available. Firstly, a horizontal absorption beam allows the cloud to be imaged after 20ms of ballistic expansion ($a_s = 0$) in free space to calibrate absolute atom number. A second vertical, far-detuned imaging beam utilizes nondestructive shadowgraph imaging to take *in situ* images of the condensate [101]. Discussed in Chapter 2, the atomic density can be recovered from the shadowgraph imaging signal using the inverse Laplace operator (Equation (2.69) and Equation (2.70)).

Figure 5.2 shows typical signals for shadowgraph imaging of a ^{85}Rb condensate for different probe detunings. For sufficiently large probe detunings, up to 100 images can be taken in a single run as little as 0.4ms apart with no measurable change in atom number. The imaging laser is offset-beat locked, allowing the beam detuning to be

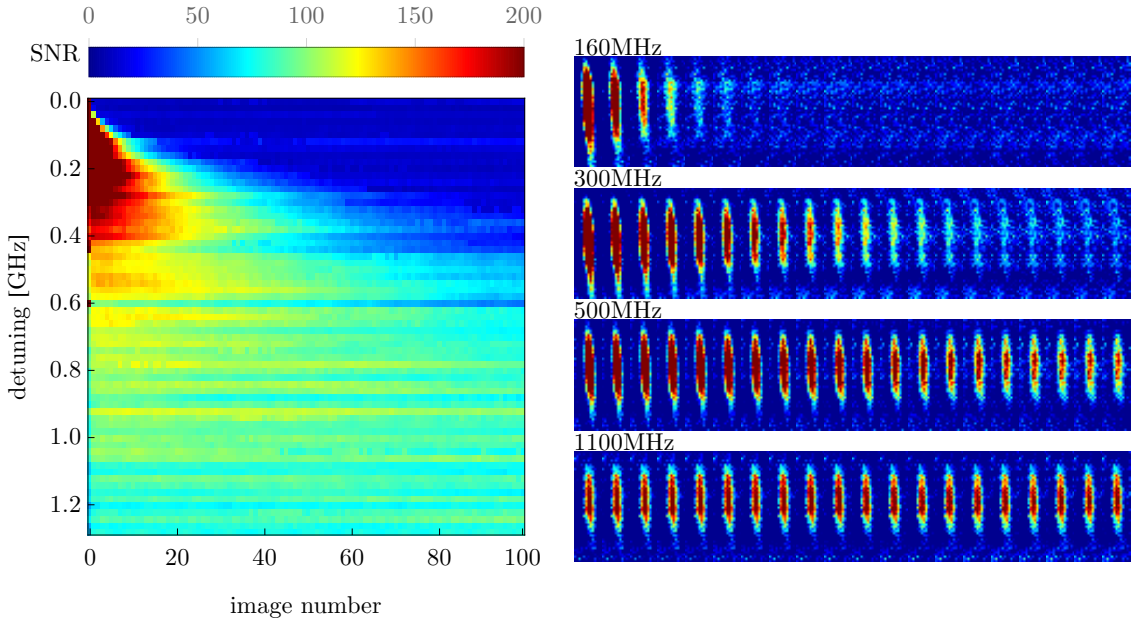

Figure 5.2: Left: density plot of the SNR of the image peak against the nth image number and probe detuning. Right: sequential images from a single run at select detunings. For the initial image, the signal is highest near resonance, however this quickly destroys the BEC. For larger detunings (1 GHz), the SNR is smaller but the signal persists unchanged for up to 100 images.

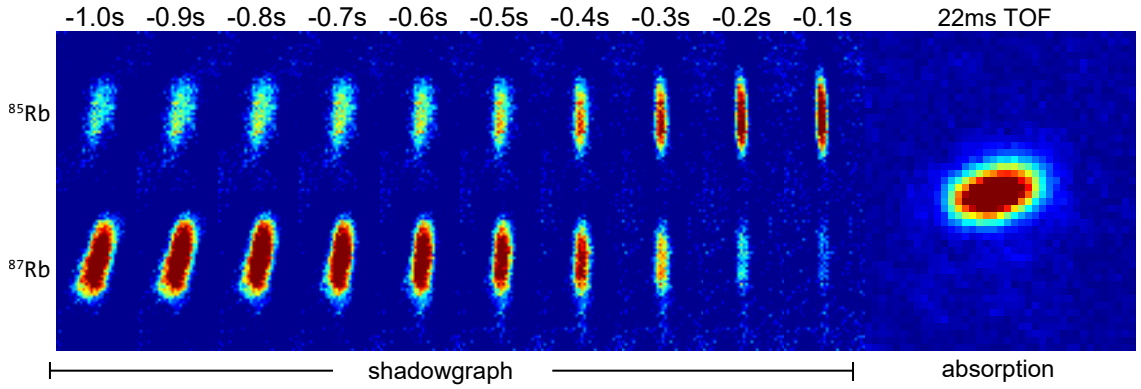

Figure 5.3: Non-destructive shadowgraph images of the sympathetic evaporation process which leads to ^{85}Rb BEC formation. For each isotope, a set of 10 non-destructive images was taken over the last 1 s of evaporative cooling in the optical trap. An absorption image of the final ^{85}Rb BEC with 3×10^4 atoms after 22 ms of ballistic expansion is also shown.

dynamically changed during a run [134]. This allows several nondestructive pictures to be taken before the laser is brought onto resonance and a final destructive, high signal-to-noise ratio (SNR) picture is taken with the same optics. Figure 5.3 shows the use of shadowgraph imaging to image the process of sympathetic evporative cooling of ^{85}Rb with ^{87}Rb.

5.3 Soliton Break Up

The experiment is conducted as follows: a ^{85}Rb condensate of atom number $N = 3 \times 10^4$ is formed at an s-wave scattering length of $a_s \approx 300a_0$ in a harmonic trap ($\omega_z = 2\pi \times 7$ Hz axially, $\omega_r = 2\pi \times 70$ Hz radially) before the axial trapping is turned off creating an optical waveguide for the atoms. The waveguide has a repulsive harmonic potential with frequency $\omega_z = 2\pi \times 3i$ Hz (the complex frequency here forms the anti-trapping potential) due to curvature in the magnetic potential (Section 5.1). Simultaneously, the scattering length is rapidly quenched to another value within the range $[-2.1, 5]a_0$, before the condensate is allowed to evolve in the waveguide for approximately 100ms. In all figures t is the time after this quench, once the condensate is freely propagating in the waveguide. For these initial conditions the chemical potential is $\mu = 6.2\hbar\omega_z$, which is the strongly cigar-shaped regime [135]. The longitudinal shape of the condensate has a width (L_z) on the order of tens of micrometers. Dispersion of the cloud in the waveguide is minimized by careful choice of initial scattering length. Our choice ensures that the dimensions of the axially-trapped cloud prior to quenching a_s are similar to those of an axially-untrapped soliton at the new (necessarily negative) scattering length. This is determined by a variational method [111]. The condensates are then propagated in the waveguide for a range of scattering lengths ($a_s/a_0 \in [-6, 6]$).

For propagation at certain negative scattering lengths the condensate breaks up into a train of similarly sized, spatially-localized components. These are soliton-like, in that they are stable under further propagation beyond 90ms. Three separate exemplar runs are shown in Figure 5.4. These examples demonstrate the typical train formation at $-1.15a_0$, a scattering length for which the condensate is stable up to 60 ms. Moreover, for $a_s > -1.15a_0$, three-body-recombination losses are $< 5\%$ in the first-stage dynamics where train formation occurs.

Ten runs were conducted for each choice of a_s. The number of spatial components formed after each experimental run was quantified using an image processing algorithm (Figure 5.5). The images are firstly de-noised with a discrete cosine transform (DCT) threshold filter. A binary threshold (60% of peak image intensity) is then applied. The number of resulting solitons is then found by counting the morphological components.

Train formation is stochastic in nature – the same experimental conditions resulted in a varying number of constituent components (Figure 5.4). Although the atom number varied shot-to-shot by up to 10%, this variation was shown to be uncorrelated with the final number of components (0.042 correlation co-efficient). Variations in both the spatial

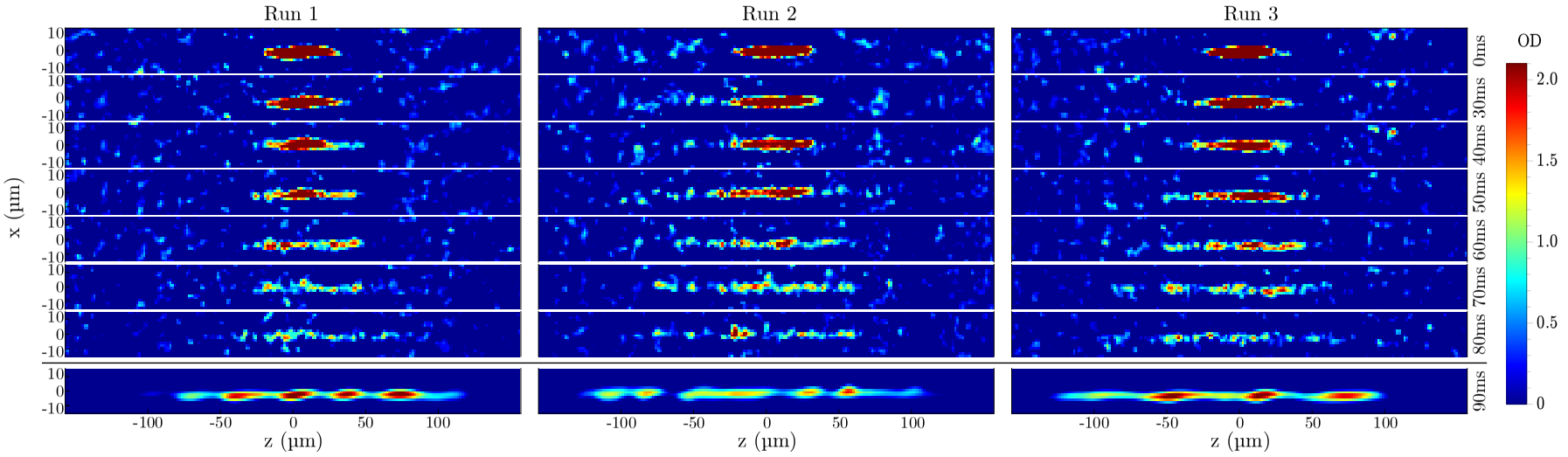

Figure 5.4: Experimental data for three separate runs illustrating the breakup phenomenon after the BEC is released into the waveguide with $a_s = -1.15a_0$. The first seven images were taken with *in situ* non-destructive shadowgraph imaging. The final image was taken with *in situ* destructive absorption imaging. Colour map optical density (OD) values relate to the destructive picture.

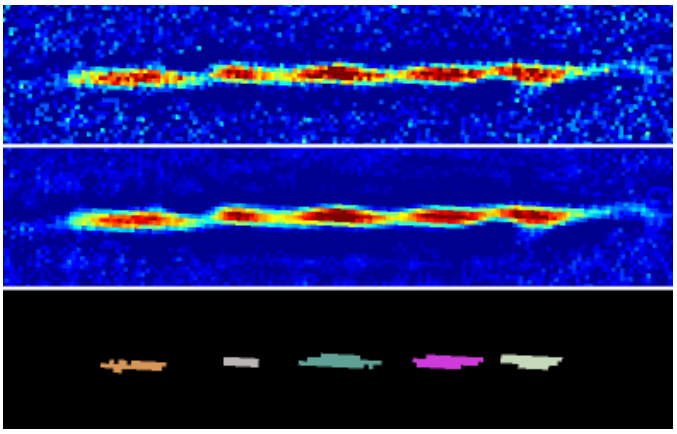

Figure 5.5: Example of post-processing experimental data for soliton enumeration. The top image is the destructive absorption image taken at the end of propagation. The middle image is the noise-reduced absorption image. Noise reduction is performed by DCT thresholding using 16 × 16 pixel blocks. The bottom image shows the connected components of the binarized middle image.

locations of the individual components and the formation onset time were also observed.

5.4 Theoretical Approach

5.4.1 Modulational Instability in the Nonpolynomial Schrödinger equation

The NPSE [133] – an effective 1D model of the Gross-Pitaevskii equation (GPE) – provides a simple and effective theoretical insight into our experimental observations. It well-approximates the full 3D dynamics of the GPE for cigar-shaped condensates whose relevant dynamics occur in the axial direction [131, 133]. According to the NPSE, the 3D condensate wavefunction is factorized into transverse and longitudinal components: $\psi(x,y,z,t) = f(z,t)\phi(x,y,t;f(z,t))$. The axial component $f(z,t)$ is the unique unknown of the model, and its evolution is described by

$$i\frac{\partial f}{\partial t} = \left[-c_1\frac{1}{2}\frac{\partial^2}{\partial z^2} + \frac{c_2}{\sigma^2}|f|^2 + c_3\left(\sigma^2 + \frac{1}{\sigma^2}\right)\right]f, \tag{5.2}$$

where $c_1 = \hbar/(2m)$, $c_2 = UN/(2\pi a_\perp^2\hbar)$, $c_3 = \omega_\perp/2$ and $\sigma^2 = (1 + c_4|f|^2)^{1/2}$, with $c_4 = 2a_sN$. Here $U = 4\pi\hbar^2 a_s/m$, N is the condensate number, and $a_\perp = \sqrt{\hbar/(m\omega_\perp)}$ is the oscillator length in the transverse direction with corresponding trapping frequency $\omega_\perp$.

Following the standard procedure [62], we describe the MI dynamics in the axial coordinate by assuming $f(z,t)$ is the sum of a plane wave and two small perturbations centred at spatial frequencies $\pm k$: $f(z,t) = u\exp(i\beta_u t) + p_+\exp[ikz + i\beta_+(k)t + g(k)t] +$

$p_- \exp[-ikz + i\beta_-(k)t + g(k)t]$, where u and $p_\pm$ are complex, β_u is real, and $\beta_\pm$ and g are real functions of k, with g the temporal growth rate of the perturbations.

Inserting this ansatz into Equation (5.2) and applying a linear stability analysis yields expressions for $\beta_{u,\pm}$ and g. The latter quantity is the gain spectrum of spatial modes with wavenumber k:

$$g(k) = \sqrt{c_1 k^2 (4M - c_1 k^2)}/2, \tag{5.3}$$

$$M = \frac{-(c_2 + c_3 c_4/2)\,|u|^2}{\sigma_0^2} + \frac{(c_2\,|u|^2 + c_3) c_4\,|u|^2}{2\sigma_0^6}, \tag{5.4}$$

where $\sigma_0^2 = (1 + c_4\,|u|^2)^{1/2}$.

Equation (5.4) implies that all spatial frequencies in the MI-band $|k| \leq 2(M/c_1)^{1/2}$ undergo amplification and that the fastest growing sidebands are at $\hat{k} = (2M/c_1)^{1/2}$ with corresponding growth rate $\hat{g} = M$.

In the weakly-interacting limit $c_4\,|f|^2 \ll 1$, Equation (5.2) reduces to the well-known 1D GPE [133], which is less accurate than the NPSE as it fails to describe the condensate dynamics outside the weakly-interacting regime [133]. Therefore, Equation (5.4) accurately describes the growth rate of perturbations in both weak- and strongly-interacting regimes.

In the more general and realistic case where the initial axial function $u_0(z) = f(z, t = 0)$ is not a plane wave but finite-sized, the BEC undergoes both a linear reshaping [first term in RHS of Equation (5.2)] and a nonlinear reshaping [second and third terms in RHS of Equation (5.2)], which are respectively analogous to the diffraction and nonlinear self-phase modulation (SPM) experienced by an optical beam propagating in nonlinear Kerr-media [136].

Linear (diffraction) and nonlinear (SPM and MI) effects interplay with each other and a characteristic time defines the temporal scale over which they become relevant to the dynamics (Appendix A). Exploiting the analogy with optical phenomena in Kerr media, the characteristic time for linear diffraction and nonlinear phenomena can be roughly estimated as $T_\mathrm{D} = L_z/c_1^2$ and $T_\mathrm{NL} = 1/(|c_2|\,u_\mathrm{peak}^2)$, respectively, where L_z is the spatial width of u_0 and $u_\mathrm{peak} = \max\{|u_0|\}$. In our experiment $T_\mathrm{D} \gg T_\mathrm{NL}$, hence the first-stage

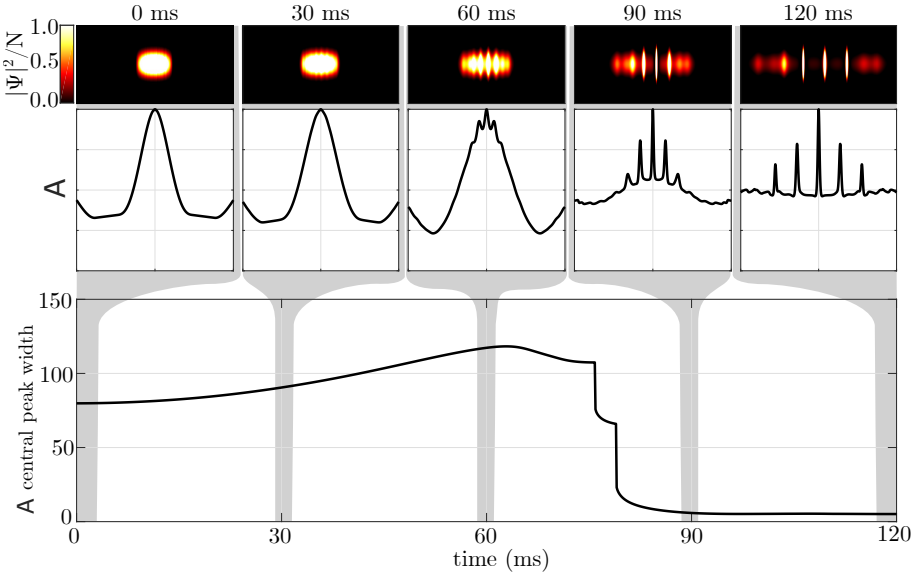

Figure 5.6: Top: Density of a simulated BEC undergoing MI in an antitrapping waveguide. Middle: Autocorrelation traces of axial density: $\mathcal{A}(z) = \int dz' |f(z-z')|^2 |f(z')|^2$. Bottom: Width of central peak of $\mathcal{A}(z)$. This width's sharp decrease at 75 ms corresponds to the time where MI is well-developed.

evolution of the condensate is dominated by MI and can be written as:

$$f(z,t) = u_0 e^{i\beta_u t} + \int dk\, p(k) e^{ikz + i\beta(k)t + g(k)t}, \tag{5.5}$$

where the integration is performed over the whole MI-band and $p(k)$ indicates the initial perturbation at spatial frequency k that is amplified with growth rate $g(k)$ [see Equation (5.4)]. The integral in Equation (5.5) represents a superposition of sinusoidal waves giving rise to the typical components observed in the condensate axial profile. If the condensate is seeded by random noise, then the initial perturbation $p(k)$ is a stochastic variable whose value depends on the particular experimental run. Consequently, for a fixed time t, the position, amplitude, and shape of the components differs between runs. This explains the random nature of the components experimentally observed and represents a truly distinctive signature of the MI regime.

Although the number of morphological components after breakup is random, the average distance $\langle d_z \rangle$ between consecutive components is set by the fastest growing spatial frequency, i.e. $\langle d_z \rangle = 2\pi/\hat{k}$. This allows a simple estimate of the average number of components via $\langle N_{\mathrm{Comp}} \rangle = L_z / \langle d_z \rangle$.

5.4.2 NPSE Simulation

Additional to this analytic theory, we performed NPSE simulations that aimed to reproduce experimental conditions, including the antitrapping waveguide potential and three-body recombination losses, modeled by including $iK_3N^2|f|^4f/(2\pi a_\perp^2\sigma^2)^2$ in the RHS of Equation (5.2) ($K_3 = 4\times10^{-41}$ m^{6}s^{-1} is experimentally determined). The simulations were seeded with Gaussian noise with a minimum spatial correlation width determined by the condensate's healing length, ensuring that the perturbation only contained physical noise. The noise amplitude was approximately 1% of $|\psi|$.

Figure 5.6 displays the evolution of a simulated BEC undergoing MI, resembling the typical evolution observed in experiments (Figure 5.4). Condensate breakup causes the formation of spatial components, which become distinct and separated once MI amplification is well-developed. Furthermore, the final distribution is typically asymmetric as a result of the random seeding noise ($|\Psi|^2$ in Figure 5.6).

SPM induces an axial compression of the condensate, corresponding to a broadening of the condensate's initial axial spectrum (i.e. Fourier transform of u_0). The larger the width Δk of the initial axial spectrum, the faster the spectral broadening and the corresponding spatial compression. When $\Delta k \gtrsim \hat{k}$, the spectral broadening of the axial spectrum overlaps the MI-band and amplification of the seeding noise is negligible. Here, the SPM-induced spatial compression is followed by complex dynamics that could lead to the creation of distinct spatial components (Appendix A). These dynamics are similar to those undergone by short optical pulses in Kerr-media [136]. However, in this circumstance the number, position, and shape of the spatial components are fully deterministic, as they do not depend on the seeding noise.

An intermediate regime exists where neither MI nor SPM are truly dominant, but are equally important to the condensate dynamics. In this instance, the condensate undergoes a partial reshaping followed by the creation of random spatial components related to the MI (Appendix A).

For typical experimental parameters $L_z \sim 50\mu$m and $a_s \sim -a_0$, we estimate $\Delta k \sim 1/L_z \approx 20\text{m}^{-1}$ and $\hat{k} \approx 100\Delta k$, therefore SPM does not dominate over MI. However, for sufficiently negative scattering lengths, simulations show that a fast and strong spectral broadening due to SPM occurs.

5.5 Results

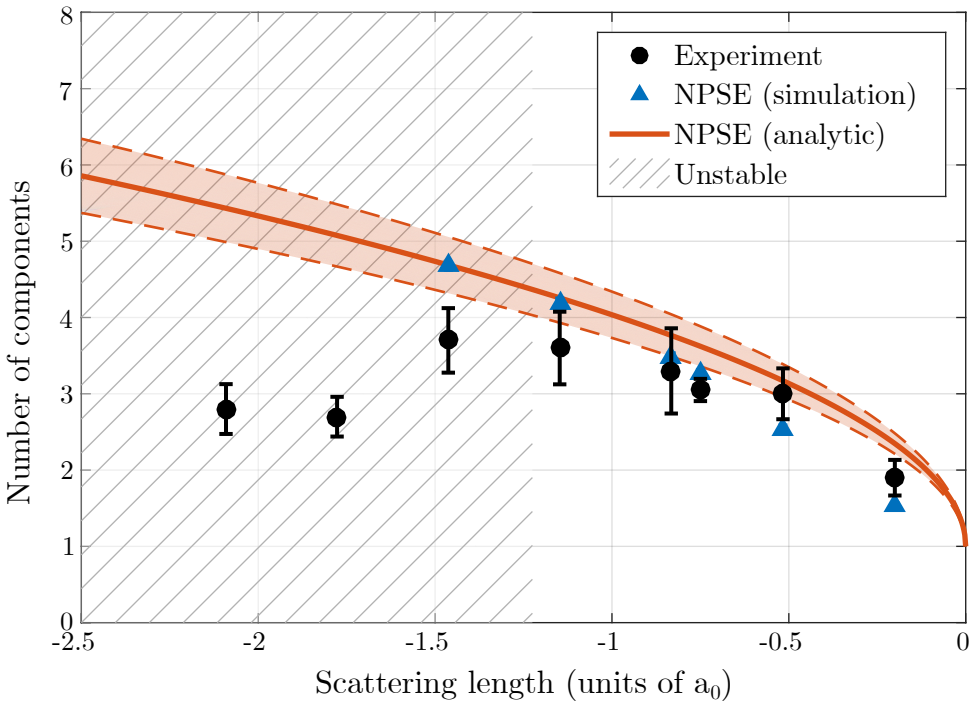

Figure 5.7: Average number of spatial components observed in experiment at t=90ms compared with NPSE simulations and analytic estimation $\langle N_{\mathrm{Comp}} \rangle = L_z / \langle d_z \rangle$ (shading indicates 10% uncertainty in measured L_z). The initial BEC is considered to have one component. Uncertainties are indicated by the standard error in the mean (these are smaller than the point width for simulations). The hatched region indicates the absence of a stable soliton solution.

The average number of spatial components experimentally observed as a function of quenched a_s is shown in Figure 5.7 alongside the predictions from a stability analysis of the NPSE as well as NPSE simulations. The difference between simulations and analytic estimation is expected due to the presence of a partial SPM pulse reshaping as well as the antitrapping potential not accounted for by our analytical model. Nevertheless, after excluding data for $a_s < -1.7a_0$ (where a large thermal population was observed, so mean-field formalism is not applicable), χ^2-tests show that our analytic theory ($\chi^2(6) = 1.512$, $p = .959$) and NPSE simulations ($\chi^2(6) = 0.861$, $p = .990$) agree well with the experimental data. Note also that stable soliton solutions of the initial condensate do not exist below $a_s = -1.2a_0$, as determined by a variational analysis of the GPE energy functional [111].

The *distribution* of measured components was also compared to that predicted by NPSE simulations. We compare the number of spatial components experimentally measured after breakup to 1D NPSE simulations (only in the regime $a_s \leq -1.7a_0$ where a negligible thermal population was observed and mean-field theory is valid).

In order to determine whether the predictions of this theoretical model are in good agreement with the experimental data, we apply the independent samples t-test for unequal variances (i.e. Welch's t-test). This allows us to assess the difference between the theoretically-predicted and experimentally-measured distributions for each quenched scattering length. We did *not* assume equal variance between the two distributions, as we do not have a detailed *a priori* understanding of the technical noise sources within the experiment that lead to the stochastic variation in component breakup.

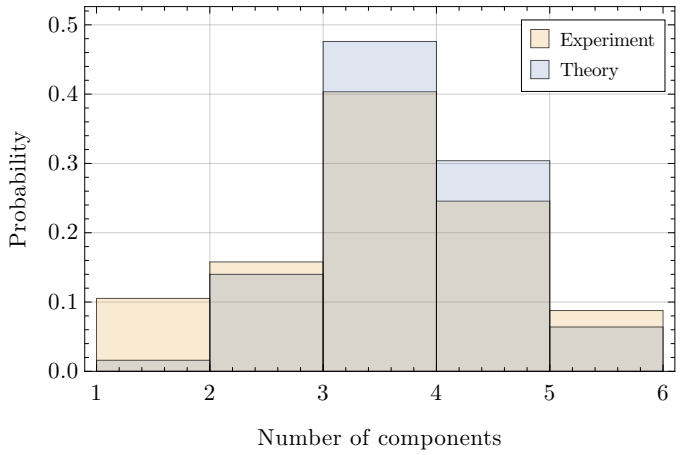

Figure 5.8: Probability of observing a given number of spatial components for both experiment (57 runs) and simulation (250 runs) at quenched scattering length $a_s = -0.75a_0$. Grey regions indicate overlap of both distributions. An independent sample t-test ($t(71.67) = -1.346$, $p = .183$) reveals no significant difference between the two distributions.

The results of our analysis are shown in Table 5.1. Each scattering length was analysed with 250 simulation runs and between 10 and 57 experimental samples. Since all t-tests returned $p > 0.05$, we conclude that the distribution of components in the experiment did not significantly differ from the distribution of components predicted by the NPSE; this agreement is pictorially demonstrated for $a_s = -0.75a_0$ in Figure 5.8.

Scattering length (a_0)	t statistic	df	p value
-0.200	.838	9.318	.423
-0.517	.683	9.344	.511
-0.750	-1.346	71.670	.183
-0.832	-.560	9.226	.589
-1.148	-1.278	9.376	.232
-1.463	-2.241	9.178	.051

Table 5.1: Results of t-tests for each quenched scattering length. For each test, we report the t-statistic, the degrees of freedom (df), and p value.

The observed random position, number, and amplitude of measured components is truly indicative of MI dynamics. Agreement with NPSE simulations of MI is seen in both

the mean and standard deviation of the number of measured components. In contrast, if train formation was seeded by linear effects, its dynamics would be deterministic, similar to what occurs with SPM reshaping. Furthermore, although the mean-field formalism employed here cannot account for fragmentation effects captured by the many-body model, the fragmentation dynamics predicted in an initially symmetric condensate are highly symmetric [137]. Therefore, the stochastic breakup dynamics observed in our experiments are a truly distinctive signature of MI, whereas the observation of symmetric and deterministic behavior would be suggestive of a different underlying mechanism, such as MI seeded by linear effects from fragmentation or SPM reshaping.

Similar work, developed independently, was released after the preparation of the manuscript related to this work, which focuses on MI in Li condensates [71]. The process used to investigate the onset of MI in Li was comparable to that used here for ^{85}Rb, with a Li BEC cloud quenched from a scattering length of $3a_0$ to a negative value. Although [71] was performed in the presence of axial harmonic confinement (an additional effect that needs to be disentangled from MI), the results presented broadly confirm what was observed here.

In summary, we have presented a continuous experimental observation of MI in a BEC. A major advance of our experiment is the ability to nondestructively image stochastic time-dependent nonlinear phenomena with high temporal resolution. Our experimental observations are in good agreement with analytical and numerical predictions provided by the NPSE, and suggest that MI seeded by noise is the key physical mechanism underlying the breakup of elongated condensates into matter-wave solitary waves.

5.6 Future work

The improvements made to the experimental apparatus will allow the detailed study of many new aspects of nonlinear dynamics driven by MI. For MI to occur, an initial perturbation is required that then exponentially grows. Applying a reproducible initial noise profile to seed the condensate (necessarily greater in amplitude than those already present in the system) would remove the stochastic nature of the MI, allowing the timescales and transient dynamics of MI to be closely compared with simulations. Additionally, the solitons here are created by matching the dimensions of the trapped and untrapped clouds when switching off the confining potential and adjusting the scattering length. If, instead, a small mismatch in the radial widths of these two solutions

is created, then a transverse excitation will be present during MI, altering the dynamics in a way not captured by the NPSE. Finally, the role of the relative phase in soliton-soliton interactions, either attractive or repulsive, has previously only been inferred through comparison with GPE simulation [138]. Combining the agile imaging system of the apparatus and the ability to perform Bragg interferometry along the waveguide [122] would allow a direct measurement of this effect. By first nondestructively observing train formation and subsequent soliton interactions, neighboring solitons can then be interfered and their relative phase read out with higher SNR destructive imaging.

Chapter 6

Dual Species Groundstates in an Optical Trap

Single component condensates present a unique system for experimentally probing the non-linear Schrödinger equation (NLSE). Due to the high level of control over both the non-linearity and trapping potential, they have been a useful tool in studying a variety of manifestations of nonlinear physics such as solitons and instabilities.

Specifically, bright solitons, where an attractive non-linearity balances dispersion, have been created in optical waveguides [66, 67]. These solitons, propagating without expanding, have been utilised to enhance fringe visibility in guided atom interferometers [122]. The formation of trains of bright solitons has also been shown to be a manifestation of modulational instability (Chapter 5) [70, 71]. Dark solitons – a non-dispersing dip in the density profile – have also been imprinted directly onto BECs [68]. The ability to actively drive these systems, by way of modulating the non-linearity or the trapping potential, has shown the onset of dynamical instability in a moving optical lattice [72], the creation of pattern-forming Faraday waves [139], as well as the creation of superfluid vortices [140].

Two-component mixtures of condensates, comprised of coupled NLSEs, offer an even richer system and there has been significant recent interest in a wide variety of coupled nonlinear phenomena. The onset and control of a breadth of two-component instabilities have been investigated both in theory and experiment: quantum turbulence and counter superflow instabilities [77, 78], Kelvin-Helmholz instability [79], classical rotation emergence in superfluids [80] and the formation of dark solitons and their subsequent decay to rings [82]. Periodically driven two-component BECs have shown the onset of chaos and allow the crossover from classical to quantum systems to be investigated [83]. Additionally, large non-linear atom-atom interactions in two-component BECs have been used to generate exotic non-Gaussian entangled states [141] which have potential applications in quantum enhanced atom interferometry [142]. Systems with

asymmetric atom densities also give access to impurity physics and may be used for thermometry [143].

All these exotic phenomena require the preparation of varied, yet reproducible ground states. While previous work has focused on experimental observations of immiscible states in ^{85}Rb /^{87}Rb mixtures [144], it has lacked a thorough theoretical investigation through a coupled Gross-Pitaevskii approach.

In this chapter we present a detailed experimental study of phase separated ground states in a ^{85}Rb /^{87}Rb mixture, showing that we can reliably create a variety of ground-state configurations, and provide a comparison to coupled Gross-Pitaevskii simulations. Firstly, a brief introduction to two component BEC theory is presented and an overview of previous experimental work in superfluid mixtures is given. We then describe the experimental procedure for generating, imaging and analysing our mixed states. The apparatus allows us to sensitively tune the energy scales of trapping potential, interaction, and gravitational potential energies, which allows access to a variety of phase separated states for our system. Tuning the intraspecies scattering length of ^{85}Rb (a_s) allows the curvature of the isotope boundary to be tuned with a high reproducibility shot-to-shot. Accompanying theoretical groundstate GPE simulations, done by S.S. Szigeti, are shown to be in good agreement with the measured curvatures. The curvature of this boundary is shown to be a good categorisation of these phase separated states, in contrast to previous uses of shifts in the center-of-mass (COM). The phase-separated groundstates generated open up an avenue to investigate the effect of surface curvature, which can be well controlled, tuned and repeatedly generated in our system, on interface and instability dynamics.

6.1 Two component condensate mixtures

6.1.1 Theory of Mixed BECs

An important property of the mixed BEC system is the components' miscibility. This is a measure of the inclination for the components' to either homogeneously mix or remain separated. In Section 3.6 we derive the usual miscibility criteria $g_{12} > \sqrt{g_{11}g_{22}}$, however under this analysis the atom number difference between the components is inconsequential. Additionally, this criteria gives no information of different immiscible groundstate configurations resulting from the form of the trapping potential, and any effects of gravitational sag.

When considering ground states for single component condensates, a number of exact solutions exist for both 1D and fully 3D cases. For non-interacting BECs, in the ideal gas limit, the condensate takes on the harmonic oscillator ground state [13]. In the strongly interacting regime the kinetic energy term can be neglected in what is known as the Thomas-Fermi limit where the condensate takes on the shape of the trapping potential [13]. Attractively interacting condensates give rise to soliton like solutions where the attractive interactions balance the repulsive kinetic term [122].

While there has been some analytical work on solutions to the two component case [145], these have had limitations. Firstly, for immiscible condensates the boundary between two condensates may limit the applicability of the Thomas-Fermi limit, as the high spatial derivative increases the kinetic energy locally in this area. Secondly and more importantly, the effects of atomic mass difference in a gravitational field have been sidestepped by using highly symmetric Gaussian trapping potentials. These effects are crucial to understanding and controlling experimental two component systems.

6.1.2 Experimental Superfluid Mixtures

Superfluid mixtures have been observed in a variety of inter-atomic and inter-isotope combinations: ^{87}Rb/^{41}K [146], ^{87}Rb/^{133}Cs [147, 148], ^{85}Rb/^{87}Rb [144], ^{168}Yb/^{174}Yb [149], ^{87}Rb/^{84}Sr and ^{87}Rb/^{88}Sr [150]. Although these superfluid mixtures can exist in *miscible* states, where there is no well defined phase separation, additional richness of the system is gained for *immiscible* mixtures. First created with superfluid mixtures of ^{3}He/^{4}He [151], there have now been a number of experimental realisations of these states.

The manifestation of this phase separation is highly dependent on the competing scattering lengths of the system, trapping frequencies and mass difference. While the relation $g_{12}^2 > g_{11}g_{22}$ [114] is typically given as the condition for immiscibility, a number of experimental realisations have shown that other factors can increase the regime where separation occurs [152, 153]. The competing energies from the gravitational and trapping potential give rise to either horizontal phase separation (vertical phase boundaries), or vertical phase separation (horizontal phase boundaries). The horizontally separated case has been experimentally investigated in Bose-Fermi mixtures of ^{40}K/^{87}Rb [154], ^{85}Rb/^{87}Rb [144], and two spin states in ^{87}Rb [147, 155]. Previous work on groundstates with gravitational sag driven separation has shown a variety of possible vertically separated configurations [152, 153, 156, 157] but has lacked a systematic study into the separation boundary between the two components.

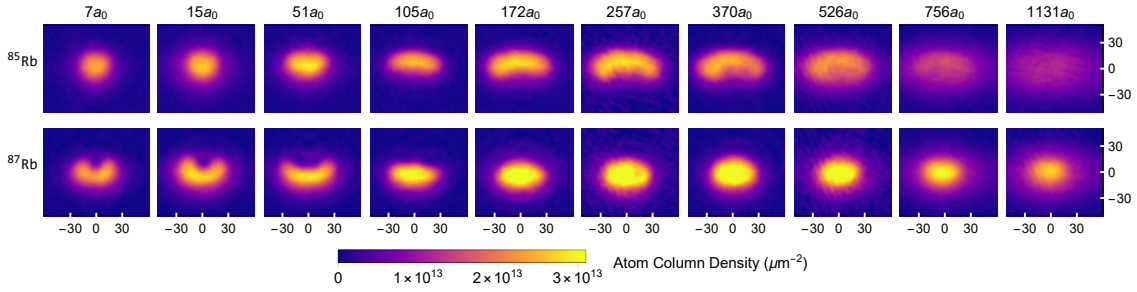

Figure 6.1: Groundstates for the dual species BEC system with $N_{85}/N_{87} = 1$ for increasing ^{85}Rb self scattering length a_s (from left to right), as imaged perpendicular to the prolate optical trap direction. Tick marks are in μm. Each pair of absorption images (^{85}Rb and ^{87}Rb) is a single experimental realisation, taken after 5ms of ballistic expansion. The vertical position shift due to the 1ms delay between the ^{85}Rb and ^{87}Rb images has been removed. For small scattering lengths the ^{85}Rb condensate is partially enveloped by ^{87}Rb. As the ^{85}Rb scattering length increases beyond that of ^{87}Rb ($100a_0$), the curvature of the boundary between them changes sign. For $a_s > 526a_0$ the two clouds begin to enter the miscible regime and become increasingly overlapped.

6.2 Formation of ^{87}Rb and ^{85}Rb condensates

6.2.1 Experimental Procedure

The experimental apparatus is described in Chapter 4 with the experimental procedure as follows: a dual species mixed BEC is formed in the optical dipole trap with the ^{85}Rb scattering length set at $80a_0$. Over 400ms the powers in the optical trap are adiabatically ramped up, increasing the depth of the optical trap and preventing further evaporation. This step also serves to re-enter the harmonically trapped regime in the optical trap (Figure 4.14). Simultaneously, the scattering length of ^{85}Rb is adiabatically ramped to the final value for the desired groundstate. The adiabaticity of these ramps is checked by looking for a lack of collective excitations in the BEC. The optical trap is then rapidly switched off and the atoms undergo 5ms of ballistic expansion before being imaged. The experiment is repeated for ^{85}Rb intra-species scattering lengths from 0 to $1000a_0$. The effect of relative atom number is also investigated. Controlling the initial load time of ^{85}Rb atoms from the 2D MOT we are able to create atom ratios from pure ^{87}Rb to ^{85}Rb.

6.2.2 Dual Species Imaging

Ideally the BEC groundstates would be imaged while still in the optical trap, however this is difficult for two reasons. Firstly the small size of the condensate (a few micrometres) requires the use of high numerical aperture optics with large magnification, and any structure inside the boundary between condensates would be much smaller again.

Secondly, the two isotopes are imaged at slightly different wavelengths, $F = 2 \rightarrow F' = 3$ (780.246 02 nm) and $F = 3 \rightarrow F' = 4$ (780.243 73 nm) for the D_2 line of ^{87}Rb and ^{85}Rb respectively. Although switching between these two frequencies is trivial, the 1.1 GHz detuning between them would cause parasitic lensing of the light which passes through the non-resonant isotope due to the high optical densities in trap. This lensing will distort the isotope boundary in the final image [101].

Instead the clouds are allowed to undergo ballistic expansion, whereby the optical trap is rapidly switched and the clouds free-fall for 5ms. This has the effect of both lowering the optical density and any lensing effects, while also enabling the self-similar expansion to magnify the phase boundary. A fast frame rate camera (Grasshopper 3 GS3-U3-41C6NIR-C) allows separate images of both ^{85}Rb and ^{87}Rb in the same run to be taken with a 1ms delay. The ^{85}Rb atoms are first repumped and imaged on the $F = 3 \rightarrow F' = 4$ transition. After 1ms delay, limited by the camera frame rate, the ^{87}Rb atoms are repumped and imaged on the $F = 2 \rightarrow F' = 3$ transition. No significant change in the characteristics of the BECs, due to either the repumping or extra 1ms of expansion, is shown when the imaging order is swapped. The additional 1ms of fall for ^{87}Rb results in a positional offset of 54 µm, which must be removed from the image to realign the two isotopes. Typical images of the groundstates are shown in Figure 6.1.

6.2.3 Image Processing

Although the centre-of-mass shift is a useful tool for identifying different features of the transition between immiscible and miscible groundstates, it elucidates little information about their geometrical configuration. Alternatively, this categorisation may be done by extracting the nature of the isotope boundary. The boundary is found using an image processing algorithm on the two absorption images (Figure 6.2).

Firstly, the ratio of the two atomic column densities is calculated with regions of low atomic density ($< 5 \times 10^{12} \mu m^{-2}$) removed (Figure 6.2c). The boundary is then along the line where the atomic number ratio is parity. Given the limited image size, optical resolution and noise in the absorption images, this line is non-trivial to calculate immediately. Instead, the region $-0.2 < \mathrm{Log}(N_{85}/N_{87}) < 0.2$ (Figure 6.2d) is found. Small non-contiguous components are removed and then morphological thinning is applied to extract the 1-pixel wide boundary path (Figure 6.2e). The curvature κ along a parametrisation of this path is calculated by the first and second derivatives of the path in the x and y direction:

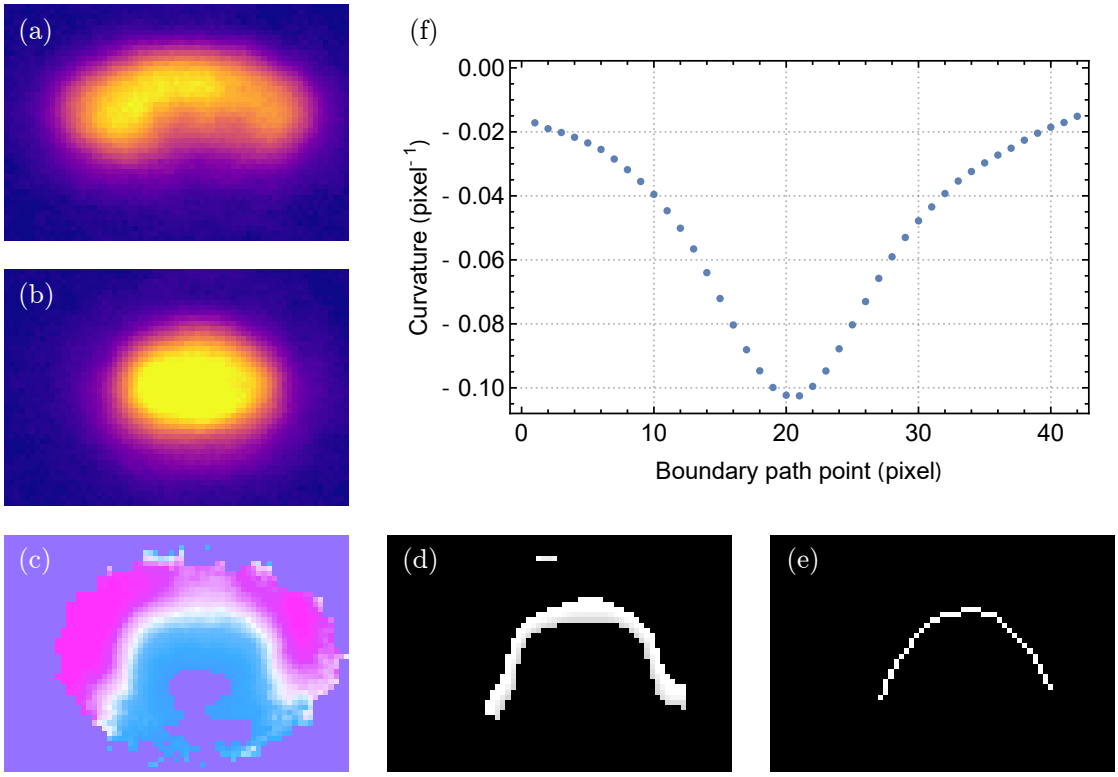

Figure 6.2: Example of the boundary curvature extraction process for a single experimental run at $a_s = 370a_0$. a) Absorption image of ^{85}Rb. b) Absorption image of ^{87}Rb. c) Density plot of the isotope ratio N_{85}/N_{87}; ^{85}Rb and ^{87}Rb are pink and blue respectively with white regions of equal density. d) Region where $-0.2 < \mathrm{Log}(N_{85}/N_{87}) < 0.2$. e) Morphologically thinned phase path giving the isotope boundary. f) Calculated curvature along the boundary path; integrating this curve gives the dimensionless total curvature as -2.1.

$$\kappa = \frac{x'y'' - y'x''}{(x'^2 + y'^2)^{3/2}}. \tag{6.1}$$

The numerical derivatives y', x', y'' and x'' along the path are found by convolution with a Gaussian derivative kernel of radius equal to the diffraction limit of the imaging system, removing sharp steps between pixels due to the discrete sampling. κ is then integrated along the path to give a dimensionless parameter for the phase boundary curvature (Figure 6.2f).

The curvature finding algorithm is applied to both experimental and simulation images identically with no free parameters.

6.3 Simulation Approach

The difficulty in achieving analytical results for this system necessitates the use of numerical simulations. A full 3D two component GPE simulation, while numerically

	$\omega_x/2\pi$ (Hz)	$\omega_y/2\pi$ (Hz)	$\omega_z/2\pi$ (Hz)
^{85}Rb	104.4 ± 0.5	78.1 ± 0.5	13.2 ± 0.5
^{87}Rb	103.3 ± 0.5	74.6 ± 0.5	13.1 ± 0.2

Table 6.1: The values of the trapping Frequencies used for 3D GPE simulations, as found in Section 4.5.

costly to solve, is needed due to the lack of symmetries in the system. Groundstates of our system are found by utilising imaginary time propagation [158, 159], solved using the software package XMDS2 [160].

Ramping the optical trapping powers up after BEC formation minimises the anharmonicty of the optical trap. However, the gravitational sag still induces both a shift in the trap centre and trapping frequency between the two isotopes. The experimentally measured trapping frequencies for each isotope are shown in Table 6.1 and are consistent with the full potential model shown in Section 4.5. Careful attention must be paid to the inclusion of the vertical trapping frequency, as this includes the effect of gravitational sag shifting the trap centre. The expected trapping potential, combining the optical dipole trap with the gravitational potential, is given by:

$$\begin{aligned} V(y) &= \frac{1}{2}m\omega_y^2 z^2 - mgz \\ &= \frac{1}{2}m\omega_y^2 \left(z - \frac{g}{\omega_y^2}\right)^2 - \frac{1}{2}m\frac{g^2}{\omega_y^2}. \end{aligned} \tag{6.2}$$

This is factored to give an analytical estimate ($\frac{g}{\omega_y^2}$) for the trap centre shift given a measured trapping frequency in the vertical direction. The parameters in Table 6.1 give trap offsets of -40.6 ± 0.5μm and -44.6 ± 0.6μm for ^{85}Rb and ^{87}Rb respectively.

Without the inclusion of both the gravitation sag and trapping frequency difference between the isotopes into the simulated groundstates, the geometrical arrangement seen in the experimental results could not be reproduced. Instead, immiscible groundstates with horizontal separation along the weak trapping axis were found. Simulations with the 4 μm trap centre offset were able to show agreement with the experimental configurations found.

The high densities present for the in-trap BEC groundstates will influence the condensate evolution during ballistic expansion due to the inter-species mean field [153]. To account for this, after groundstate convergence from imaginary time propagation the condensates were allowed to freely evolve with no trapping potential for 5ms. Due to the delayed dual species imaging, the ^{87}Rb was also expanded for an additional 1ms.

The 5ms and 6ms expansions showed negligible difference in the final image (except a known COM shift due to free fall under gravity). The experimental absorption images are taken on resonance, necessitating the switch off of the Feshbach resonance generating magnetic coil 500 µs beforehand. During this brief period the ^{85}Rb atoms evolve under the zero-field scattering length $-440a_0$, potentially causing catastrophic collapse [128]. Simulations including this period showed that 4ms of expansion sufficiently lowered the atomic densities such that collapse was avoided and had no significant difference compared to those which omitted this detail.

Simulated groundstates were completed for parameters found from each individual experimental run, N_{85}, N_{87}, and a_s (1108 groundstates in total).

6.4 Results

Figure 6.1 shows experimental dual species groundstates with equal atom numbers of ^{85}Rb and ^{87}Rb. The horizontal prolate trapping potential (Figure 4.13) gives a large preference for groundstates with vertical separation between the species. This consistent separation allows for a variety of immiscible groundstates to be accessible simply by varying the scattering length of ^{85}Rb.

6.4.1 Miscible to Immiscible Transition

As the scattering length increases, the condensates transition from the immiscible to miscible regime. The cross scattering length $a_{85,87} = 213a_0$ and the self scattering length $a_{87,87} = 100.4a_0$ [161], along with the immiscibility criteria ($g_{12}^2 > g_{11}g_{22}$), gives $a_s = 452a_0$ as an estimate of the point at which the phase separation occurs. Figure 6.1 shows this transition beginning to occur at $a_s = 526a_0$, with fully miscible states at $a_s = 1131a_0$. In contrast for an unequal mixture where $N_{85}/N_{87} = 0.35$ the immiscible states persist into higher scattering lengths (Figure 6.3).

6.4.2 Centre of Mass

Previous works on phase separated BEC mixtures have predominantly focused on the use of centre-of-mass (COM) differences between the two components to identify phase separated groundstates [144]. Figure 6.4 shows the measured vertical COM separation (ΔCOM) of the ^{85}Rb and ^{87}Rb condensates for 1108 different experimental runs. The

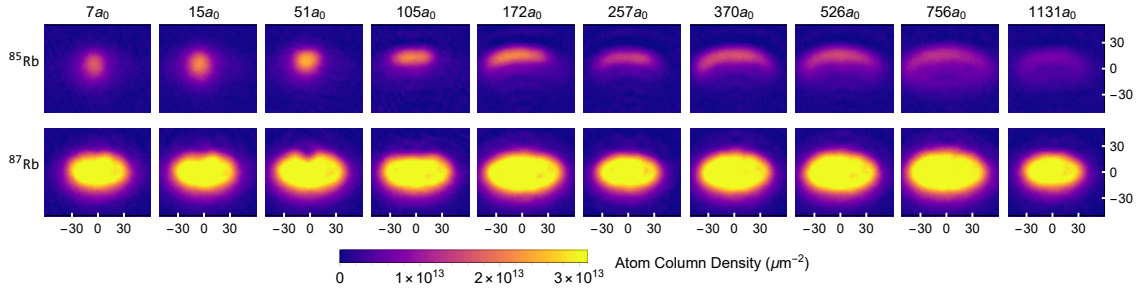

Figure 6.3: Groundstates for the dual species BEC system with $N_{85}/N_{87} = 0.35$ similarly as for Figure 6.1. Tick marks are in μm. For small scattering lengths the ^{85}Rb condensate is almost fully enveloped by ^{87}Rb, with much smaller COM shift compared to the $N_{85}/N_{87} = 0.5$ case. As the ^{85}Rb scattering length increases beyond that of ^{87}Rb ($100a_0$), the curvature of the boundary similarly changes sign. For these ^{85}Rb depleted cases the phase separation between the isotopes persists at higher scattering lengths.

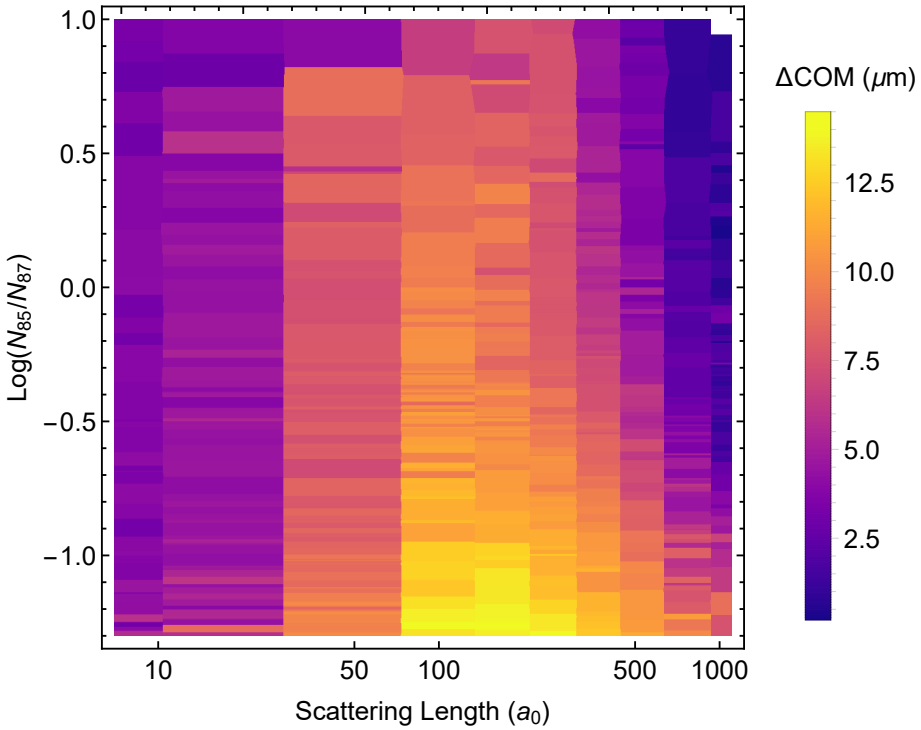

Figure 6.4: Density plot of the centre-of-mass separation between the ^{85}Rb and ^{87}Rb condensates for different atomic ratios and ^{85}Rb intra-scattering lengths. The scattering length has been plotted with a logarithmic axis. The logarithm of the atom ratio has been taken to equally distribute around a y-axis value of 0 which corresponds to $N_{85}/N_{87} = 1$. Each rectangle corresponds to one experimental realisation (1108 total groundstates). Maximum separation between the isotopes is achieved when a_s is close to parity with $a_{87,87}$; this separation is increased for ^{85}Rb depleted cases (-1 on the y-axis). The separation reduces towards zero for increasing scattering lengths above the predicted immiscible/miscible boundary of $a_s = 452a_0$. This boundary is atom ratio dependent with isotope separation (immiscible states) persisting for larger a_s for smaller ^{85}Rb clouds. For small values of a_s the COM decreases due to the ^{85}Rb condensate becoming enveloped by ^{87}Rb.

separations measured are significantly greater than the gravitational sag in the optical trapping minimum between the two isotopes. Above the predicted immiscible/miscible

boundary of $a_s = 452a_0$, ΔCOM decreases towards the in trap gravitional sag given by Equation (6.2) (4.0(8) µm) indicating overlapping condensates. The separation decreases to as little as 1.5 µm, most likely due to a small potential difference between the two isotopes (such as from a magnetic gradient) during the time of flight. The transition is gradual, consistent with previous investigations into the immiscible/miscible transition [153]. This is extended for mixed BECs which are depleted in ^{85}Rb, with immiscible states persisting up to $a_s = 1131a_0$ for $N_{85}/N_{87} = 0.37$ (corresponding to -1 on the y-axis of Figure 6.4).

The largest separation between the isotopes is achieved when a_s is close to parity with $a_{87,87}$ with a maximum reached for small ^{85}Rb condensates. Scattering lengths below this, although well into the immiscible regime, are seen to reduce the isotope separation (Figure 6.5). The lower mean field energy allows the spatially small ^{85}Rb BEC to sag into the large ^{87}Rb condensate.

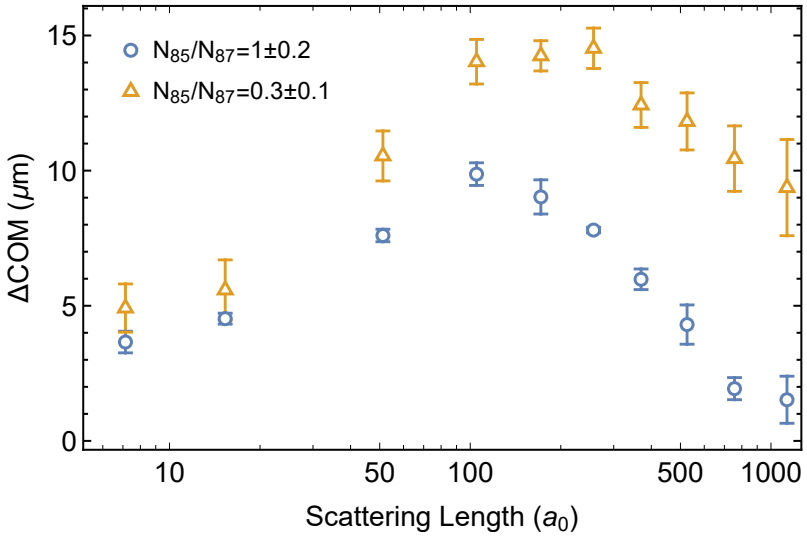

Figure 6.5: ΔCOM as plotted against a_s. Individual points indicate the mean and standard deviation of all experimental runs which fall within the atom ratio bins $N_{85}/N_{87} = 1 \pm 0.2$ and 0.3 ± 0.1.

6.4.3 Isotope Boundary

The curvature of the isotope boundary for equal mixtures ($N_{85}/N_{87} = 1 \pm 0.2$), integrated over the length of each path, is plotted in Figure 6.6 against the ^{85}Rb scattering length. A clear trend from convex to concave isotope boundary is seen, with good agreement to theoretical simulation. Several fitting functions were trialled, with an arc-tangent found to well identify the zero crossing point. For both simulation and experiment this occurs where the ^{85}Rb intra-scattering length is equal to the ^{87}Rb intra-scattering length, with

values of $99 \pm 3a_0$ and $107 \pm 9a_0$ for the experiment and simulation, respectively.

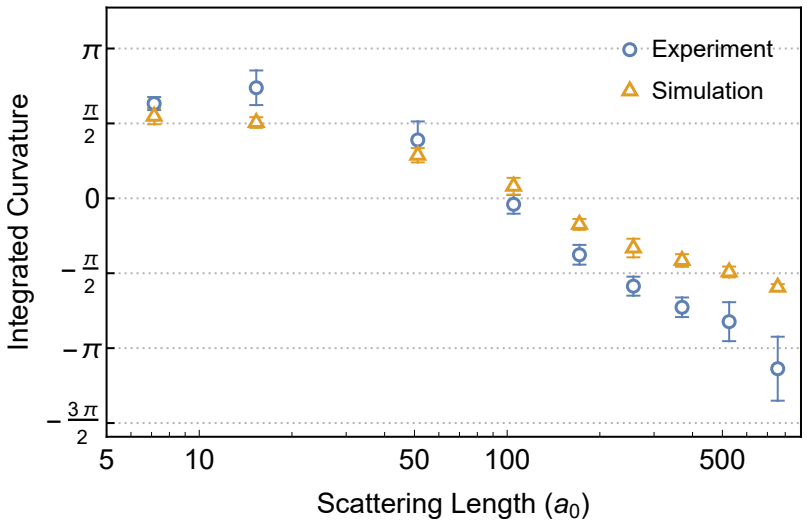

Figure 6.6: Curvature of the isotope boundary for equal mixture immiscible ground states at different ^{85}Rb scattering lengths. Individual points indicate the mean and standard deviation of all experimental and simulation runs which fall within the atom ratio bin $N_{85}/N_{87} = 1 \pm 0.2$. As the ^{85}Rb scattering length reaches that of ^{87}Rb the curvature tends to zero. The zero crossing point is correctly predicted by theoretical simulations of the full 3D GPE. For larger scattering lengths the experiment tends towards larger negative curvatures than simulation. This is most likely caused by the curvature finding algorithm becoming unstable due to experimental noise as the cloud begins to transition into a miscible arrangement.

The curvature was additionally found for non-equal mixtures of atoms. Individual realisations of experiment or simulation were gathered by $\log(N_{85}/N_{87})$ with a bin width of 0.2. The range of ratios over which curvature values could be found for experimental runs is smaller than simulation, primarily due to limitations of the imaging system. For each bin the curvature as a function of a_s was fitted with an arc-tangent function. The fitted curvature zero crossing points in terms of a_s are plotted against the bin centres in Figure 6.7. As the ratio of ^{85}Rb to ^{87}Rb increases, the scattering length at which there is a flat isotope boundary decreases. The linear trend in the logarithmic plot shown in Figure 6.7 was fitted with the line in Equation (6.3):

$$\log a_s = b_1 + b_2 \log\left(\frac{N_{85}}{N_{87}}\right) \tag{6.3}$$

$$\frac{N_{85}}{N_{87}} = \left(\frac{c}{a_s}\right)^d. \tag{6.4}$$

With the substitution $b_1 = \log c$ and $b_2 = -\frac{1}{d}$ Equation (6.3) can be rewritten as Equation (6.4). The fit parameters of $c = 100.4 \pm 2.2$, $d = 1.9 \pm 0.3$ and $c = 100.1 \pm 2.3$, $d = 1.9 \pm 0.1$ for experiment and simulation respectively, are both in good agreement

(see Figure 6.7). The parameter c, defining the scattering length at which an equal isotope ratio achieves a flat boundary curvature, is equal to the ^{87}Rb scattering length.

This somewhat surprising result suggests the idea that there may be a balance in the interaction energies of the two isotopes at this point. Under inspection of Equation (3.37), we can equate the self interaction energy terms $N_1^2 g_{11}$ and $N_2^2 g_{22}$ to attempt an energetic explanation for this balance:

$$\frac{N_1}{N_2} = \left(\frac{g_{22}}{g_{11}}\right)^{1/2}. \tag{6.5}$$

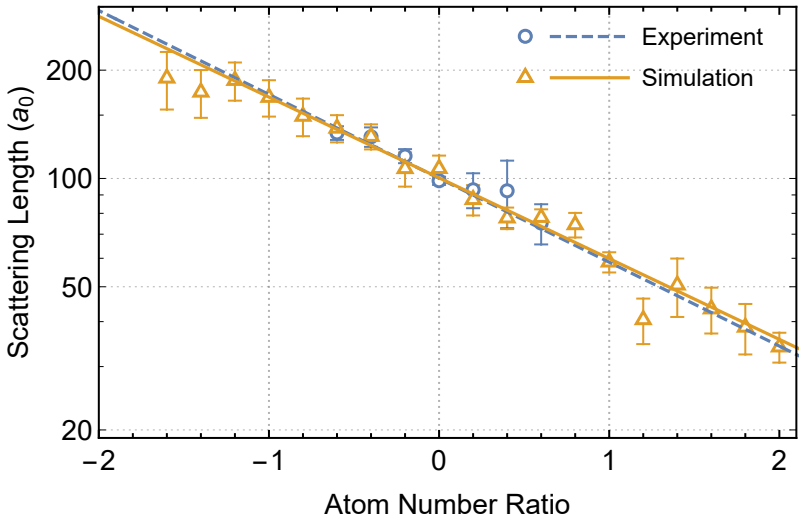

Figure 6.7: Logarithmic plot of the scattering length where the boundary curvature crosses zero for different atom number ratios (plotted as $\mathrm{Log}(N_{85}/N_{87})$ for clarity), with lines of best fit for experiment and simulation. The fit lines are of the form $\frac{N_{85}}{N_{87}} = \left(\frac{c}{a_s}\right)^d$ which are linearised by fitting in logarithmic space. Fit parameters are $c = 100.4 \pm 2.2$, $d = 1.9 \pm 0.3$ and $c = 100.1 \pm 2.3$, $d = 1.9 \pm 0.1$ for experiment and simulation respectively.

However, the resulting equation does not agree with the fitted value for the exponent d. Given the disagreement already discussed with this simple homogeneous model, this is no surprise. Conveniently, the GPE groundstate simulations allow the contribution of different energies to be extracted. The self-interaction energy for each isotope ($E_{\mathrm{int},85}$ and $E_{\mathrm{int},87}$) in each ground state is calculated by integrating the terms in Equation (3.34). Figure 6.8 shows the variation of the ratio of the per atom interaction energy over the ground state sampling domain. A clear linear trend is seen where the energy per particle is equal. Similar to Figure 6.7, the data was binned and a line of fit $\frac{N_{85}}{N_{87}} = \left(\frac{c}{a_s}\right)^d$ found for these regions. A line of fit for both the interaction energy and interaction per atom is shown in Figure 6.9. The resulting fit parameters do not agree with the trend found for the boundary curvature zero crossing points. As of yet the theoretical nature of the line of zero curvature is still an open question.

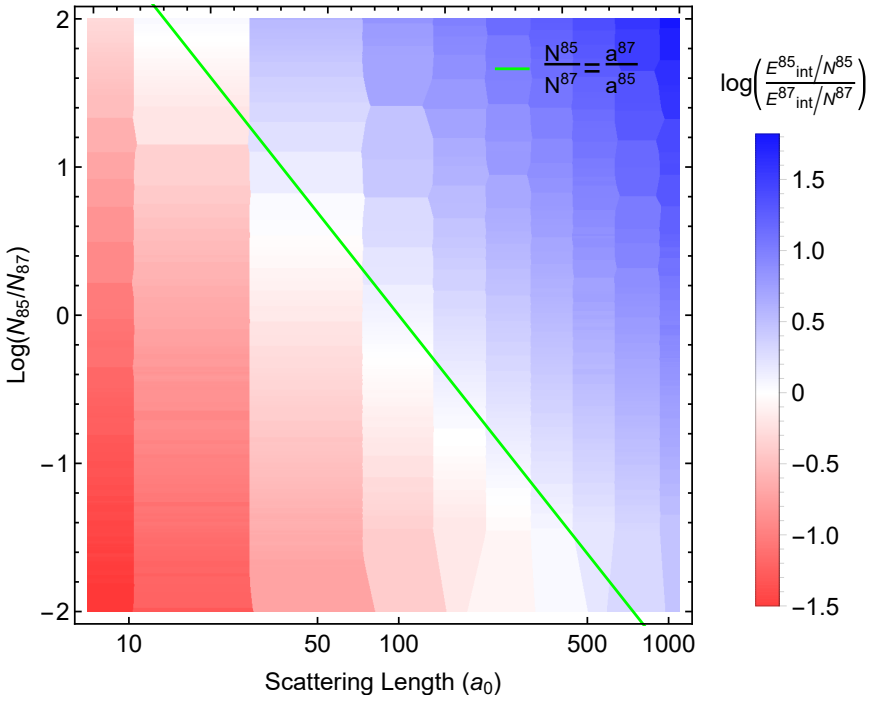

Figure 6.8: Density plot of the ratio of the interaction energy per atom for both ^{85}Rb and ^{87}Rb, respectively. The line $N_{85}a_{85} = N_{87}a_{87}$ is shown in green.

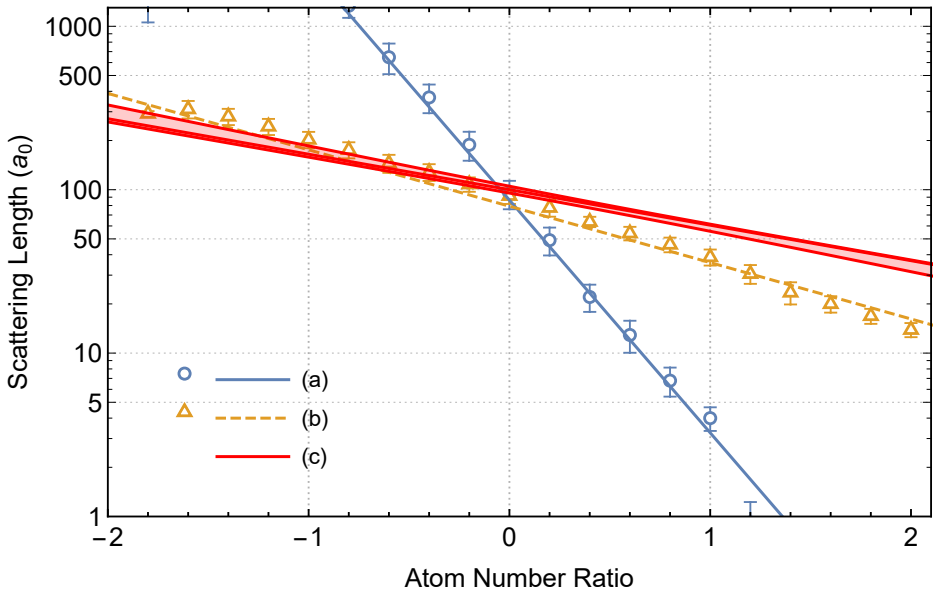

Figure 6.9: Logarithmic plot of the scattering length where the energy ratio between the isotopes is equal for different atom number ratios (plotted as Log(N_{85}/N_{87}) for clarity), with lines of best fit. The fit lines are of the form $\frac{N_{85}}{N_{87}} = \left(\frac{c}{a_s}\right)^d$ which are linearised by fitting in logarithmic space. a) Interaction energy ratio ($E_{\text{int},85}/E_{\text{int},87}$), with fitted parameters $c = 87 \pm 6$, $d = 0.30 \pm 0.01$. b) Interaction energy per atom ratio $(E_{\text{int},85}/N_{85})/(E_{\text{int},87}/N_{87})$, with fitted parameters $c = 79 \pm 2$, $d = 1.26 \pm 0.03$. c) 95% confidence band for the fit to the simulated groundstate curvatures shown in Figure 6.7.

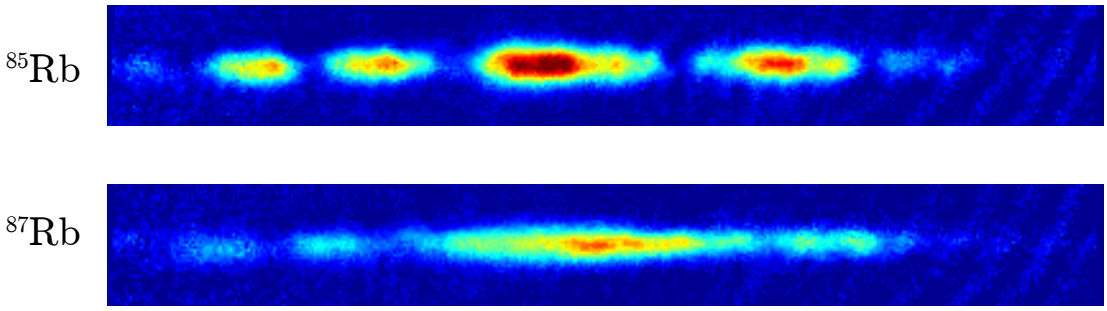

Figure 6.10: A single experimental run of a dual component ^{85}Rb/^{87}Rb condensate released into an optical waveguide at $a_s = 2.8a_0$. Spatially separated clouds are formed in a stochastic manner run-to-run. As the scattering length is positive, the breakup mechanism cannot be modulational instability, however the data is too preliminary to classify it as capillary instability.

6.5 Applications and Future Work

The breadth of theoretical investigations for two-component physics [77–81, 84] prompts a desire for experimental investigation. These experiments require both the ability to prepare a variety of groundstates in a controllable manner and high confidence that the preparation procedure produces the desired groundstate with high fidelity from shot-to-shot. Quantum turbulence and counter superflow and the resulting manifestations of instability require exquisite control of the component boundary. We have shown a unique ability to manipulate the initial ground state into a number of reliable configurations, and given a robust method of classifying these states. The region where the interface between two BEC components is flat, shown to be of the form $\frac{N_{85}}{N_{87}} = \left(\frac{c}{a_s}\right)^d$, is of particular interest when considering velocity shear experiments.

The states we have shown thus far are simply prepared in an optical trap. However, our ability to create an optical waveguide by switching off one of the confining beams as in the case of Chapter 5, allows the investigation of further dynamical instabilities for two-component condensates. Of particular interest in this system is the capillary instability, whereby an elongated two component BEC undergoes spontaneous droplet formation [162]. Unlike the case of modulational instability which causes a single component BEC to form spatially localised clouds due to self focusing from an attractive scattering length, a capillary instability will still occur for repulsive interactions. Figure 6.10 shows the result of releasing a dual component ^{85}Rb and ^{87}Rb BEC into an optical waveguide with $a_s = 2.8a_0$. Although preliminary, the stochastic formation of spatially localised clouds is promising for the investigation of dual component instabilities.

The ability to control the formation of groundstates through a_s is an ideal mechanism to investigate the onset of critical wetting, first-order wetting and prewetting phase transitions in dual component condensates [163]. A steep potential wall is required to observe this transition and could be achieved with a blue detuned light sheet. This experimental addition would be straightforward with the current optical setup.

Chapter 7

Conclusions and outlook

This thesis has presented experimental work on the creation of an entirely new dual-species ^{85}Rb/^{87}Rb BEC apparatus and the use of atom interactions to investigate non-linear phenomena. The new apparatus, presented in Chapter 4, is a significant improvement on previous designs, both in terms of the size of condensates and duty cycle, as well as experimental simplicity [115]. BECs of atom number up to 2×10^5 and 2×10^6 of ^{85}Rb and ^{87}Rb, respectively, can be created in 13 s. Accurate control over the intra-species scattering length of ^{85}Rb is achieved with a combination of an ultra precise current driver and passive mu-metal shielding. Combined with a well calibrated model of the optical potential, the apparatus is well suited for investigating a range of non-linear phenomena.

In Chapter 5 we presented the first real time observation of the non-linear process known as modulational instability (MI) in a BEC. A novel non-destructive imaging technique called "shadowgraph imaging" was used to image the break-up of soliton-like BECs into a train of spatially localised components. Utilising a statistical comparison to both analytical and simulated results from the nonpolynomial Schrödinger equation, the underlying mechanism of the instability was demonstrated to be MI.

Chapter 6 presented an experimental study of the dual-component ground states of the ^{85}Rb/^{87}Rb system. We demonstrated the ability to reliably generate a range of configurations, utilising control over both the intra-species scattering length and the atom ratio in the BEC. The interface between two components was shown to be well categorised by the curvature of the boundary, with good agreement between experimental and simulated ground states. The dependence of the interface curvature on the scattering length and isotope ratio is shown to obey a power law, of which the origin remains an open question.

7.1 Future Work

The fundamental design principle of the apparatus – one of simplicity and high optical access – was guided by the future introduction of experimental hardware necessary to investigate a range of phenomena. The non-diffracting Bessel waveguide will allow a large increase in the space-time area and hence sensitivity of a guided atom interferometer compared to previous experiments [115, 122]. The addition of either acousto-optically steered optical tweezers [164], or a DMD or SLM generated reconfigurable potential [165] transverse to the waveguide, combined with easy to implement non-destructive shadowgraph imaging, will allow a breadth of new experiments to be undertaken. Immediate avenues include the investigation of real time tunnelling and the effects of interactions on transmission [129] and the construction of atomic Fabrey-Perot cavities [39].

The free on-axis beam path, given by the internal mirror mounts of the vacuum system, gives access to extremely high optical densities (OD). For typical ^{87}Rb BECs, ODs of up to 1000 could be achieved. These high OD clouds would be ideal for the implementation of quantum memory schemes such as electromagnetically induced transparency, achieving unprecedented phase shifts [117–119], as well as quantum non-demolition squeezing with an application to atom-interferometers [166].

The ability to accurately engineer a range of two-component ground states allows the study of a range of novel non-linear effects in superfluids [79–81, 84]. The creation of a velocity shear across the isotope interface may generate quantum turbulence and counter-flow instabilities [77, 78, 167]. Loading a suitably prepared dual-component BEC into the Bessel waveguide will allow the onset of a capillary instability to be observed [162]. Controlling the formation of ground states through a_s, combined with a steep potential wall generated by a DMD or SLM, is an ideal mechanism to investigate the onset of critical wetting, first-order wetting and pre-wetting phase transitions in dual component condensates [163].

The reliance of these phenomena on the non-linear parameter (the collision scattering length) may necessitate a more accurate calibration scheme than current methods which utilise Feshbach resonance properties. Applying a known spatial perturbation across a BEC with an optical potential transverse to the waveguide will generate seeded instabilities [168]. Monitoring the onset of instability and measuring the timescale for development gives another method for calibration of the non-linear parameter in the GPE [169]. An alternative method is the direct measurement of mean-field shifts in atom interferometers. Utilising spatial-fringe readout [170] would allow the mean field energy

to be read out as a function of atomic density, thereby calibrating the interaction strength.

The dual-species apparatus at ANU has provided new insights into non-linear phenomena. Its upgraded, flexible and robust design will ensure a continued contribution to the field in the future.

Appendix A

Interplay between reshaping and modulational instability

In this appendix we analyze in more detail the role played by condensate reshaping (linear and nonlinear) as well as its mutual interplay with MI. We show the existence of two distinct regimes that are dominated by reshaping and MI, respectively. We finally discuss an intermediate regime where reshaping and MI are both important to the condensate dynamics. These theoretical calculations are published as supplemental material in [70], and were performed by M. Guasoni. They have been included as an appendix for completeness.

Numerical simulations discussed below are related to the solution of the 1D NPSE (Equation (5.2)), where the system parameters are those of the experiment: $N = 3 \times 10^4$ is the number of ^{85}Rb bosons in the condensate; $m \approx 85\,u$ is the corresponding atomic mass; $\omega_\perp = 2\pi \times 70$ Hz is the trapping frequency in the transverse direction. We set the s-wave scattering length $a_s = -a_0$ (a_0 is the Bohr radius). The initial axial function $f(z, t = 0)$ is described by a supergaussian of order 2: $f(z, t = 0) = ne^{-z^4/L_z^4}$, n being a normalization factor such that the integral $\int |f(z,0)|^2 dz = 1$. We analyze the axial spectrum of the condensate, that is, the intensity of the Fourier transform in z of $f(z,t)$. Moreover, we vary the axial width L_z of the condensate in order to enter the different aforementioned regimes.

A.0.1 MI REGIME

When we fix $L_z = 1500\mu$m the condensate undergoes a strong MI effect that determines its dynamics. In this case, reshaping induced by diffraction is negligible because its characteristic timescale T_{D} is much longer than that related to nonlinear effects, T_{NL}. Moreover, SPM is also negligible because the width Δk of the initial axial spectrum is much smaller than the MI peak frequency $\hat{k}$ (see Figure A.1b). In order to demonstrate that the condensate dynamics are unaffected by diffraction and SPM, we simply run the simulation without seeding noise. Results in Figure A.1a,b clearly show that at $t = 7$s the shape of the density distribution $|f|^2$ and the corresponding spectrum are practically un-

changed, confirming that the presence of diffraction and SPM do not play any relevant role. On the contrary, when a seeding noise is employed in the simulation, the condensate axial shape is strongly modified by MI. Figure A.1c,e show that running two simulations with different seeding noise yields a different pattern of separated components. Therefore, the random position, shape, and number of components is actually a clear signature of MI in the spatial domain. Another interesting MI-feature comes from the spectra in Figure A.1d,f; we clearly observe the raising of MI-bands that are in full agreement with the theoretical MI-bands calculated from Equation (5.4). To conclude: both in the spatial and in the spectral domain we have a strong signature of an MI regime.

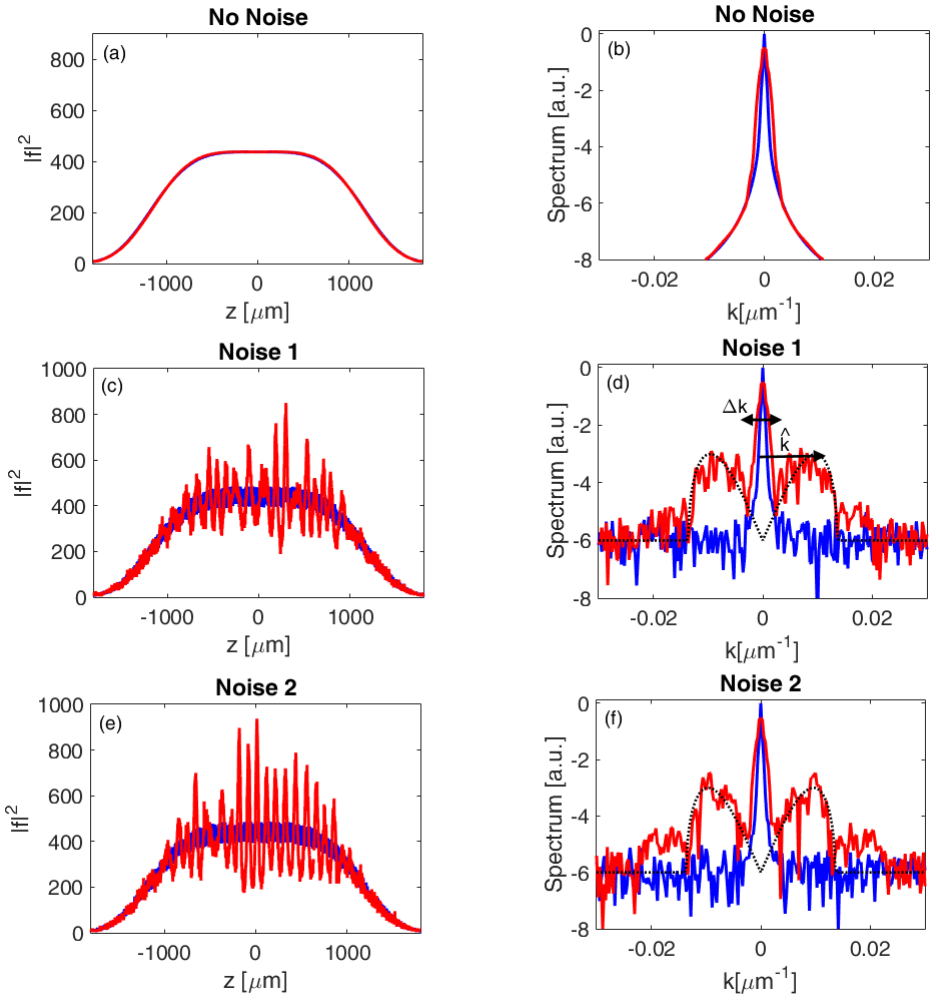

Figure A.1: Input (blue) and output (red) density functions (panels a,c,e) and corresponding spectra (panels b,d,f) when $L_z = 1500\mu$m and $t = 7$s. Panels a,b: no seeding noise. Panels c,d: seeding with noise 1. Panels e,f: seeding with noise 2. Noise 1 and 2 are different but possess the same statistics. Dotted black line in panels d and f represent the theoretical MI-band. Spectra are in dB.

A.0.2 RESHAPING REGIME

If we strongly shrink the initial condensate in the axial direction, then the perturbed plane wave approach typically employed in the description of MI cannot capture the true condensate dynamics, which is actually dominated by the reshaping due to both diffraction and SPM. Figure A.2 displays (at $t = 0.2$s) the input and output density distributions of the condensate and their corresponding spectra when $L_z = 5\mu$m. Panels a,b refer to the instance in which no seeding noise is applied, whereas panels c,d to the instance where a seeding noise is applied whose statistics is the same as the seeding noise used to produce Figure A.1c-f. As shown in Figure A.2d, in this case the initial spectrum width Δk is large enough to completely overlap the MI-band. Therefore, the SPM causes a strong spectral broadening which is totally independent of the underlying seeding noise. Contrary to the case of Figure A.1, here panels b,d clearly show that the output spectrum is practically unaffected by seeding noise and the same applies to the output density distributions (panels a,c). The dynamics are then fully deterministic and, at a fixed time t, we observe almost the same density distribution whatever the seeding noise is.

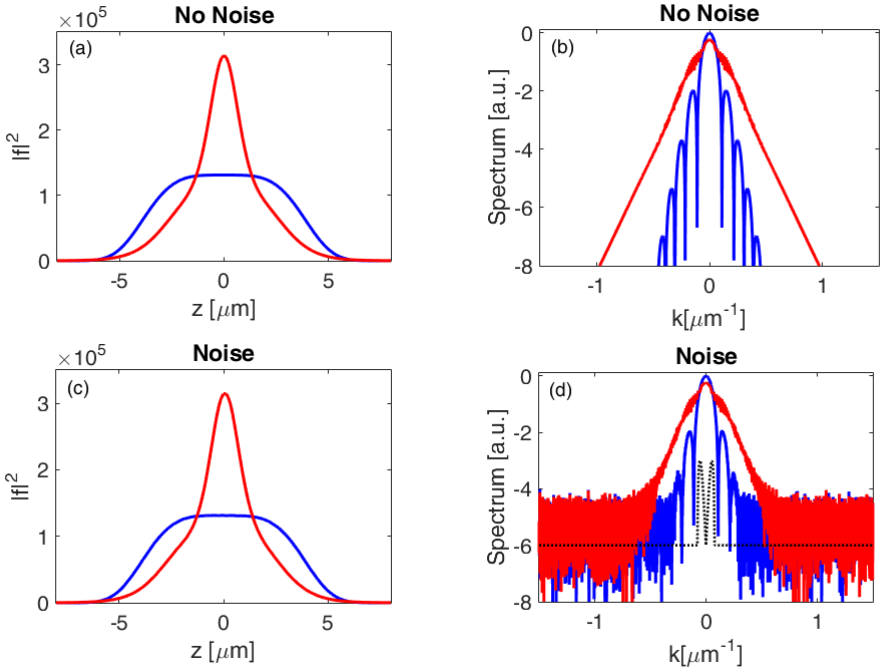

Figure A.2: Same as Figure A.1, but for $L_z = 5\mu$m and $t = 0.2$s. Panels a,b: no seeding noise. Panels c,d: seeding with noise.

It is worth examining the full spatio-temporal evolution of the density distribution, which is shown in Figure A.3. We see that the condensate alternately experiences a compression and broadening in the axial direction, which is due to the mutual interplay between SPM and diffraction. The first induces a strong compression, that is the spatial counterpart of the spectral broadening, whereas the second counterbalances the SPM

and tends to widen the condensate once it has been compressed. As a result, the full dynamics is almost periodic and resembles the dynamics experienced by short optical pulses in Kerr-media. On the other hand, several different spatio-temporal evolutions can be observed depending on the particular shape of the input condensate as well as on the linear and nonlinear coefficients of the system ($c_{1,2,3,4}$ in Equation (5.2)).

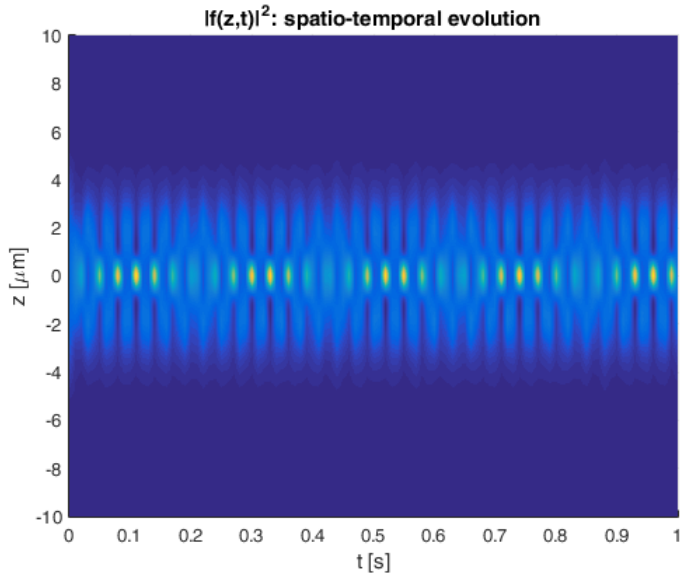

Figure A.3: Spatio-temporal evolution of the density distribution $|f|^2$ for $L_z = 5\mu$m and $t = 0.2$s. In this instance the evolution, which is dominated by reshaping, is quasi-periodic.

A.0.3 INTERMEDIATE REGIME

From the above considerations, we may expect that an intermediate regime exists where neither MI nor reshaping are dominant. In order to explore such a regime, we fix $t = 0.2$s and $L_z = 45\mu$m, which is similar to the input axial width in our experiments (Figure 5.4). Following the same procedure employed for the MI regime and the reshaping regime, we first run the simulation in the absence of seeding noise. We see in Figure A.4a,b that if the noise is absent then the dynamics is driven by a strong reshaping. On the other hand, when noise is introduced, MI also plays a non-negligible role and gives rise to the formation of components, similarly to the case of a pure MI regime (see Figure A.4c-f). Most importantly, the output density distribution exhibits the typical MI-signature which is represented by a random position and shape of the components. However, in this case a partial correlation among components (i.e. 'humps') in different runs is present (see humps-A,B in panels c and e), which is due to the interplaying deterministic reshaping.

Note also that the creation of well-defined and separated components occurs on a timescale $\lesssim 90$ms, in agreement with experimental results (Figure 5.4).

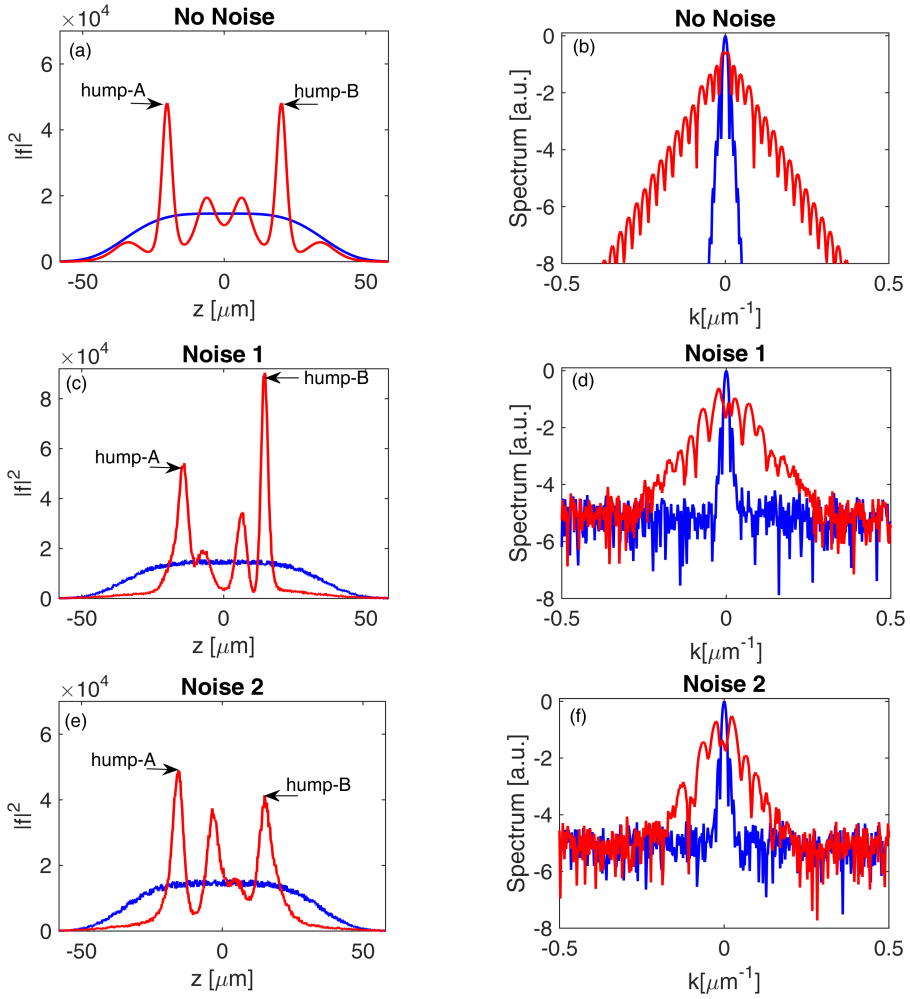

Figure A.4: Same as Figure A.1, but for $L_z = 45\mu$m and $t = 0.2$s. Lateral humps (i.e. components) in the output density function are highlighted in panels a,c,e, showing the partial correlation between their position in the absence and presence of noise, respectively.

References

[1] H. Poincare. *New Methods of Celestial Mechanics*, volume 13 of *History of Modern Physics and Astronomy*. AIP-Press ([1892] 1993). [p 1]

[2] A. M. Lyapunov. *The general problem of the stability of motion*. International Journal of Control **55**, 531 (March 1, 1992 [1892]). ISSN 0020-7179. DOI: 10.1080/00207179208934253. [p 1]

[3] E. N. Lorenz. *Deterministic Nonperiodic Flow*. Journal of the Atmospheric Sciences **20**, 130 (1963). ISSN 0022-4928. DOI: 10.1175/1520-0469(1963)020<0130:DNF>2.0.CO;2. [p 1]

[4] E. Bress and J. M. Gruber. *The Butterfly Effect* (2004). IMDb ID: tt0289879 event-location: USA. [p 2]

[5] B. Eckhardt. *Turbulence transition in pipe flow: Some open questions*. Nonlinearity **21**, T1 (2007). ISSN 0951-7715. DOI: 10.1088/0951-7715/21/1/T01. [p 2]

[6] M. V. Berry. *Three quantum obsessions*. Nonlinearity **21**, T19 (2008). ISSN 0951-7715. DOI: 10.1088/0951-7715/21/2/T02. [p 2]

[7] E. Knobloch. *Spatially localized structures in dissipative systems: Open problems*. Nonlinearity **21**, T45 (2008). ISSN 0951-7715. DOI: 10.1088/0951-7715/21/4/T02. [p 2]

[8] E. Cancès, C. L. Bris, and P.-L. Lions. *Molecular simulation and related topics: Some open mathematical problems*. Nonlinearity **21**, T165 (2008). ISSN 0951-7715. DOI: 10.1088/0951-7715/21/9/T03. [p 2]

[9] F. Mosconi, T. Julou, N. Desprat, D. K. Sinha, J.-F. Allemand, V. Croquette, and D. Bensimon. *Some nonlinear challenges in biology*. Nonlinearity **21**, T131 (2008). ISSN 0951-7715. DOI: 10.1088/0951-7715/21/8/T03. [p 2]

[10] C. L. Fefferman. *Existence and Smoothness of the Navier-Stokes Equation*. Clay Mathematics Institute page 6. [p 2]

[11] A. Einstein. *Quantentheorie des einatomigen idealen Gases*. In *Sitzungsberichte der Preußischen Akademie der Wissenschaften*, volume 1 (1924). [p 2]

[12] Bose, S.N. *Plancks Gesetz und Lichtquantenhypothese*. Zeitschrift für Physik **26**, 178 (1924). ISSN 0044-3328. DOI: 10.1007/BF01327326. [p 2]

[13] W. Ketterle, D. S. Durfee, and D. M. Stamper-Kurn. *Making, probing and understanding Bose-Einstein condensates*. arXiv:cond-mat/9904034 (1999). [pp 2, 25, and 85]

[14] M. H. Anderson, J. R. Ensher, M. R. Matthews, C. E. Wieman, and E. A. Cornell. *Observation of Bose-Einstein Condensation in a Dilute Atomic Vapor*. Science **269**, 198 (1995). ISSN 0036-8075, 1095-9203. DOI: 10.1126/science.269.5221.198. [p 2]

[15] W. D. Phillips. *Nobel Lecture: Laser cooling and trapping of neutral atoms*. Reviews of Modern Physics **70**, 721 (1998). DOI: 10.1103/RevModPhys.70.721. [p 2]

[16] W. Ketterle. *Nobel lecture: When atoms behave as waves: Bose-Einstein condensation and the atom laser*. Reviews of Modern Physics **74**, 1131 (2002). DOI: 10.1103/RevModPhys.74.1131. [p 2]

[17] E. A. Cornell and C. E. Wieman. *Nobel Lecture: Bose-Einstein condensation in a dilute gas, the first 70 years and some recent experiments*. Reviews of Modern Physics **74**, 875 (2002). DOI: 10.1103/RevModPhys.74.875. [p 2]

[18] C. C. Bradley, C. A. Sackett, J. J. Tollett, and R. G. Hulet. *Evidence of Bose-Einstein Condensation in an Atomic Gas with Attractive Interactions*. Physical Review Letters **75**, 1687 (1995). DOI: 10.1103/PhysRevLett.75.1687. [p 2]

[19] K. B. Davis, M. O. Mewes, M. R. Andrews, N. J. van Druten, D. S. Durfee, D. M. Kurn, and W. Ketterle. *Bose-Einstein Condensation in a Gas of Sodium Atoms*. Physical Review Letters **75**, 3969 (1995). DOI: 10.1103/PhysRevLett.75.3969. [p 2]

[20] G. Modugno, G. Ferrari, G. Roati, R. J. Brecha, A. Simoni, and M. Inguscio. *Bose-Einstein Condensation of Potassium Atoms by Sympathetic Cooling*. Science **294**, 1320 (2001). ISSN 0036-8075, 1095-9203. DOI: 10.1126/science.1066687. [p 2]

[21] G. Roati, M. Zaccanti, C. D'Errico, J. Catani, M. Modugno, A. Simoni, M. Inguscio, and G. Modugno. ^{39}K *Bose-Einstein Condensate with Tunable Interactions*. Physical Review Letters **99**, 010403 (2007). DOI: 10.1103/PhysRevLett.99.010403. [p 2]

[22] T. Weber, J. Herbig, M. Mark, H.-C. Nägerl, and R. Grimm. *Bose-Einstein Condensation of Cesium*. Science **299**, 232 (2003). ISSN 0036-8075, 1095-9203. DOI: 10.1126/science.1079699. [p 2]

[23] S. L. Cornish, N. R. Claussen, J. L. Roberts, E. A. Cornell, and C. E. Wieman. *Stable* ^{85} *rb Bose-Einstein Condensates with Widely Tunable Interactions*. Physical Review Letters **85**, 1795 (2000). DOI: 10.1103/PhysRevLett.85.1795. [pp 2, 3]

[24] S. Kraft, F. Vogt, O. Appel, F. Riehle, and U. Sterr. *Bose-Einstein Condensation of Alkaline Earth Atoms:* ^{40}Ca. Physical Review Letters **103**, 130401 (2009). DOI: 10.1103/PhysRevLett.103.130401. [p 2]

[25] S. Stellmer, M. K. Tey, B. Huang, R. Grimm, and F. Schreck. *Bose-Einstein Condensation of Strontium*. Physical Review Letters **103**, 200401 (2009). DOI: 10.1103/PhysRevLett.103.200401. [p 2]

[26] Y. Takasu, K. Maki, K. Komori, T. Takano, K. Honda, M. Kumakura, T. Yabuzaki, and Y. Takahashi. *Spin-Singlet Bose-Einstein Condensation of Two-Electron Atoms*. Physical Review Letters **91**, 040404 (2003). DOI: 10.1103/PhysRevLett.91.040404. [p 2]

[27] A. Griesmaier, J. Werner, S. Hensler, J. Stuhler, and T. Pfau. *Bose-Einstein Condensation of Chromium*. Physical Review Letters **94**, 160401 (2005). DOI: 10.1103/PhysRevLett.94.160401. [p 2]

[28] M. Lu, N. Q. Burdick, S. H. Youn, and B. L. Lev. *Strongly Dipolar Bose-Einstein Condensate of Dysprosium*. Physical Review Letters **107**, 190401 (2011). DOI: 10.1103/PhysRevLett.107.190401. [p 2]

[29] J. Ulitzsch, D. Babik, R. Roell, and M. Weitz. *Bose-Einstein condensation of erbium atoms in a quasielectrostatic optical dipole trap*. Physical Review A **95**, 043614 (2017). DOI: 10.1103/PhysRevA.95.043614. [p 2]

[30] D. G. Fried, T. C. Killian, L. Willmann, D. Landhuis, S. C. Moss, D. Kleppner, and T. J. Greytak. *Bose-Einstein Condensation of Atomic Hydrogen*. Physical Review Letters **81**, 3811 (1998). DOI: 10.1103/PhysRevLett.81.3811. [p 2]

[31] A. Robert, O. Sirjean, A. Browaeys, J. Poupard, S. Nowak, D. Boiron, C. I. Westbrook, and A. Aspect. *A Bose-Einstein Condensate of Metastable Atoms*. Science **292**, 461 (2001). ISSN 0036-8075, 1095-9203. DOI: 10.1126/science.1060622. [p 2]

[32] M. R. Andrews, C. G. Townsend, H.-J. Miesner, D. S. Durfee, D. M. Kurn, and W. Ketterle. *Observation of Interference Between Two Bose Condensates*. Science **275**, 637 (1997). ISSN 0036-8075, 1095-9203. DOI: 10.1126/science.275.5300.637. [p 3]

[33] T. Kovachy, P. Asenbaum, C. Overstreet, C. A. Donnelly, S. M. Dickerson, A. Sugarbaker, J. M. Hogan, and M. A. Kasevich. *Quantum superposition at the half-metre scale*. Nature **528**, 530 (2015). ISSN 1476-4687. DOI: 10.1038/nature16155. [p 3]

[34] S. Gao, ed. *Collapse of the Wave Function: Models, Ontology, Origin, and Implications*. Cambridge University Press, Cambridge (2018). ISBN 978-1-108-42898-9. DOI: 10.1017/9781316995457. [p 3]

[35] T. A. Pasquini, Y. Shin, C. Sanner, M. Saba, A. Schirotzek, D. E. Pritchard, and W. Ketterle. *Quantum Reflection from a Solid Surface at Normal Incidence*. Physical Review Letters **93**, 223201 (2004). DOI: 10.1103/PhysRevLett.93.223201. [p 3]

[36] T. A. Pasquini, M. Saba, G.-B. Jo, Y. Shin, W. Ketterle, D. E. Pritchard, T. A. Savas, and N. Mulders. *Low Velocity Quantum Reflection of Bose-Einstein Condensates*. Physical Review Letters **97**, 093201 (2006). DOI: 10.1103/PhysRevLett.97.093201. [p 3]

[37] S. Potnis, R. Ramos, K. Maeda, L. D. Carr, and A. M. Steinberg. *Interaction-Assisted Quantum Tunneling of a Bose-Einstein Condensate Out of a Single Trapping Well*. Physical Review Letters **118**, 060402 (2017). DOI: 10.1103/PhysRevLett.118.060402. [pp 3, 65]

[38] P. Cheiney, F. Damon, G. Condon, B. Georgeot, and D. Guéry-Odelin. *Realization of tunnel barriers for matter waves using spatial gaps*. EPL (Europhysics Letters) **103**, 50006 (2013). ISSN 0295-5075. DOI: 10.1209/0295-5075/103/50006. [p 3]

[39] J. Billy, V. Josse, Z. Zuo, W. Guerin, A. Aspect, and P. Bouyer. *Guided atom laser: A new tool for guided atom optics*. Annales de Physique **32**, 17 (2007). ISSN 0003-4169, 1286-4838. DOI: 10.1051/anphys:2008001. [pp 3, 100]

[40] D. Becker, M. D. Lachmann, S. T. Seidel, H. Ahlers, A. N. Dinkelaker, J. Grosse, O. Hellmig, H. Müntinga, V. Schkolnik, T. Wendrich, A. Wenzlawski, B. Weps, R. Corgier, T. Franz, N. Gaaloul, W. Herr, D. Lüdtke, M. Popp, S. Amri, H. Duncker, M. Erbe, A. Kohfeldt, A. Kubelka-Lange, C. Braxmaier, E. Charron, W. Ertmer, M. Krutzik, C. Lämmerzahl, A. Peters, W. P. Schleich, K. Sengstock, R. Walser, A. Wicht, P. Windpassinger, and E. M. Rasel. *Space-borne Bose–Einstein condensation for precision interferometry*. Nature **562**, 391 (2018). ISSN 1476-4687. DOI: 10.1038/s41586-018-0605-1. [p 3]

[41] K. S. Hardman, P. J. Everitt, G. D. McDonald, P. Manju, P. B. Wigley, M. A. Sooriyabandara, C. C. N. Kuhn, J. E. Debs, J. D. Close, and N. P. Robins. *Simultaneous Precision Gravimetry and Magnetic Gradiometry with a Bose-Einstein Condensate: A High Precision, Quantum Sensor*. Physical Review Letters **117**, 138501 (2016). DOI: 10.1103/PhysRevLett.117.138501. [p 3]

[42] N. P. Robins, P. A. Altin, J. E. Debs, and J. D. Close. *Atom lasers: Production, properties and prospects for precision inertial measurement*. Physics Reports **529**, 265 (2013). ISSN 0370-1573. DOI: 10.1016/j.physrep.2013.03.006. [p 3]

[43] M. Zych and Č. Brukner. *Quantum formulation of the Einstein equivalence principle*. Nature Physics **14**, 1027 (2018). ISSN 1745-2481. DOI: 10.1038/s41567-018-0197-6. [p 3]

[44] H. Müntinga, H. Ahlers, M. Krutzik, A. Wenzlawski, S. Arnold, D. Becker, K. Bongs, H. Dittus, H. Duncker, N. Gaaloul, C. Gherasim, E. Giese, C. Grzeschik, T. W. Hänsch, O. Hellmig, W. Herr, S. Herrmann, E. Kajari, S. Kleinert, C. Lämmerzahl, W. Lewoczko-Adamczyk, J. Malcolm, N. Meyer, R. Nolte, A. Peters, M. Popp, J. Reichel, A. Roura, J. Rudolph, M. Schiemangk, M. Schneider, S. T. Seidel, K. Sengstock, V. Tamma, T. Valenzuela, A. Vogel, R. Walser, T. Wendrich, P. Windpassinger, W. Zeller, T. van Zoest, W. Ertmer, W. P. Schleich, and E. M. Rasel. *Interferometry with Bose-Einstein Condensates in Microgravity*. Physical Review Letters **110**, 093602 (2013). DOI: 10.1103/PhysRevLett.110.093602. [p 3]

[45] M. P. G. Robbins, N. Afshordi, and R. B. Mann. *Bose-Einstein condensates as gravitational wave detectors*. Journal of Cosmology and Astroparticle Physics **2019**, 032 (2019). ISSN 1475-7516. DOI: 10.1088/1475-7516/2019/07/032. [p 3]

[46] C. Barceló, S. Liberati, and M. Visser. *Analogue gravity from Bose-Einstein condensates*. Classical and Quantum Gravity **18**, 1137 (2001). ISSN 0264-9381. DOI: 10.1088/0264-9381/18/6/312. [p 3]

[47] S. Fagnocchi, S. Finazzi, S. Liberati, M. Kormos, and A. Trombettoni. *Relativistic Bose–Einstein condensates: A new system for analogue models of gravity*. New Journal of Physics **12**, 095012 (2010). ISSN 1367-2630. DOI: 10.1088/1367-2630/12/9/095012. [p 3]

[48] M. G. Richarte, I. G. Salako, J. P. M. Graça, H. Moradpour, and A. Övgün. *Relativistic Bose-Einstein condensates thin-shell wormholes*. Physical Review D **96**, 084022 (2017). DOI: 10.1103/PhysRevD.96.084022. [p 3]

[49] R. Howl, R. Penrose, and I. Fuentes. *Exploring the unification of quantum theory and general relativity with a Bose–Einstein condensate*. New Journal of Physics **21**, 043047 (2019). ISSN 1367-2630. DOI: 10.1088/1367-2630/ab104a. [p 3]

[50] N. T. Phuc, Y. Kawaguchi, and M. Ueda. *Quantum Mass Acquisition in Spinor Bose-Einstein Condensates*. Physical Review Letters **113**, 230401 (2014). DOI: 10.1103/PhysRevLett.113.230401. [p 3]

[51] J. R. Muñoz de Nova, K. Golubkov, V. I. Kolobov, and J. Steinhauer. *Observation of thermal Hawking radiation and its temperature in an analogue black hole*. Nature **569**, 688 (2019). ISSN 1476-4687. DOI: 10.1038/s41586-019-1241-0. [p 3]

[52] I. Bloch, J. Dalibard, and S. Nascimbène. *Quantum simulations with ultracold quantum gases*. Nature Physics **8**, 267 (2012). ISSN 1745-2481. DOI: 10.1038/nphys2259. [p 3]

[53] Y. Kivshar and G. Agrawal. *Optical Solitons: From Fibers to Photonic Crystals*. In *Optical Solitons: From Fibers to Photonic Crystals*, page 108 (2003). [pp 3, 31, and 69]

[54] M. S. Ruderman. *Propagation of solitons of the Derivative Nonlinear Schrödinger equation in a plasma with fluctuating density*. Physics of Plasmas **9**, 2940 (2002). ISSN 1070-664X. DOI: 10.1063/1.1482764. [p 3]

[55] D. H. Peregrine. *Water waves, nonlinear Schrödinger equations and their solutions*. The ANZIAM Journal **25**, 16 (1983). ISSN 1839-4078, 0334-2700. DOI: 10.1017/S0334270000003891. [p 3]

[56] A. V. Gurevich and L. Stenflo. *Nonlinear defocusing of radio wave beams in the ionosphere*. Physica Scripta **38**, 855 (1988). ISSN 1402-4896. DOI: 10.1088/0031-8949/38/6/017. [p 3]

[57] J. M. Dudley, F. Dias, M. Erkintalo, and G. Genty. *Instabilities, breathers and rogue waves in optics*. Nature Photonics **8**, 755 (2014). ISSN 1749-4893. DOI: 10.1038/nphoton.2014.220. [p 3]

[58] A. Chabchoub, N. Hoffmann, M. Onorato, and N. Akhmediev. *Super Rogue Waves: Observation of a Higher-Order Breather in Water Waves*. Physical Review X **2**, 011015 (2012). DOI: 10.1103/PhysRevX.2.011015. [p 3]

[59] G. Xu, K. Hammani, A. Chabchoub, J. M. Dudley, B. Kibler, and C. Finot. *Phase evolution of Peregrine-like breathers in optics and hydrodynamics*. Physical Review E **99**, 012207 (2019). DOI: 10.1103/PhysRevE.99.012207. [p 3]

[60] V. Bespalov and V. Talanov. *Filamentation structure of light beams in nonlinear liquids*. JETP Lett. **3** (1966). [pp 3, 69]

[61] W. Wan, S. Jia, and J. W. Fleischer. *Dispersive superfluid-like shock waves in nonlinear optics*. Nature Physics **3**, 46 (2007). ISSN 1745-2481. DOI: 10.1038/nphys486. [p 3]

[62] A. Hasegawa and W. Brinkman. *Tunable coherent IR and FIR sources utilizing modulational instability*. IEEE Journal of Quantum Electronics **16**, 694 (1980). ISSN 0018-9197. DOI: 10.1109/JQE.1980.1070554. [pp 3, 69, and 75]

[63] G. P. Agrawal. *Modulation instability induced by cross-phase modulation*. Physical Review Letters **59**, 880 (1987). DOI: 10.1103/PhysRevLett.59.880. [pp 3, 69]

[64] H. C. Yuen and B. M. Lake. *Nonlinear Dynamics of Deep-Water Gravity Waves*. In C.-S. Yih, ed., *Advances in Applied Mechanics*, volume 22, pages 67–229. Elsevier (1982). DOI: 10.1016/S0065-2156(08)70066-8. [p 3]

[65] F. Baronio, B. Frisquet, S. Chen, G. Millot, S. Wabnitz, and B. Kibler. *Observation of a group of dark rogue waves in a telecommunication optical fiber*. Physical Review A **97**, 013852 (2018). DOI: 10.1103/PhysRevA.97.013852. [p 3]

[66] K. E. Strecker, G. B. Partridge, A. G. Truscott, and R. G. Hulet. *Bright matter wave solitons in Bose–Einstein condensates*. New Journal of Physics **5**, 73 (2003). ISSN 1367-2630. DOI: 10.1088/1367-2630/5/1/373. [pp 4, 83]

[67] K. E. Strecker, G. B. Partridge, A. G. Truscott, and R. G. Hulet. *Formation and propagation of matter-wave soliton trains*. Nature **417**, 150 (2002). ISSN 0028-0836. DOI: 10.1038/nature747. [pp 4, 70, and 83]

[68] J. Denschlag, J. E. Simsarian, D. L. Feder, C. W. Clark, L. A. Collins, J. Cubizolles, L. Deng, E. W. Hagley, K. Helmerson, W. P. Reinhardt, S. L. Rolston, B. I. Schneider, and W. D. Phillips. *Generating Solitons by Phase Engineering of a Bose-Einstein Condensate*. Science **287**, 97 (2000). ISSN 0036-8075, 1095-9203. DOI: 10.1126/science.287.5450.97. [pp 4, 83]

[69] A. Di Carli, C. D. Colquhoun, G. Henderson, S. Flannigan, G.-L. Oppo, A. J. Daley, S. Kuhr, and E. Haller. *Excitation Modes of Bright Matter-Wave Solitons*. Physical Review Letters **123**, 123602 (2019). DOI: 10.1103/PhysRevLett.123.123602. [p 4]

[70] P. J. Everitt, M. A. Sooriyabandara, M. Guasoni, P. B. Wigley, C. H. Wei, G. D. McDonald, K. S. Hardman, P. Manju, J. D. Close, C. C. N. Kuhn, S. S. Szigeti, Y. S. Kivshar, and N. P. Robins. *Observation of a modulational instability in Bose-Einstein condensates*. Physical Review A **96**, 041601 (2017). DOI: 10.1103/PhysRevA.96.041601. [pp 4, 83, and 103]

[71] J. H. V. Nguyen, D. Luo, and R. G. Hulet. *Formation of matter-wave soliton trains by modulational instability*. Science **356**, 422 (2017). ISSN 0036-8075, 1095-9203. DOI: 10.1126/science.aal3220. [pp 4, 81, and 83]

[72] L. Fallani, L. De Sarlo, J. E. Lye, M. Modugno, R. Saers, C. Fort, and M. Inguscio. *Observation of Dynamical Instability for a Bose-Einstein Condensate in a Moving 1D Optical Lattice*. Physical Review Letters **93**, 140406 (2004). DOI: 10.1103/PhysRevLett.93.140406. [pp 4, 83]

[73] R. Meppelink, S. B. Koller, J. M. Vogels, P. van der Straten, E. D. van Ooijen, N. R. Heckenberg, H. Rubinsztein-Dunlop, S. A. Haine, and M. J. Davis. *Observation of shock waves in a large Bose-Einstein condensate*. Physical Review A **80**, 043606 (2009). DOI: 10.1103/PhysRevA.80.043606. [p 4]

[74] E. A. L. Henn, J. A. Seman, G. Roati, K. M. F. Magalhães, and V. S. Bagnato. *Emergence of Turbulence in an Oscillating Bose-Einstein Condensate*. Physical Review Letters **103**, 045301 (2009). DOI: 10.1103/PhysRevLett.103.045301. [p 4]

[75] N. G. Parker and C. S. Adams. *Emergence and Decay of Turbulence in Stirred Atomic Bose-Einstein Condensates*. Physical Review Letters **95**, 145301 (2005). DOI: 10.1103/PhysRevLett.95.145301. [p 4]

[76] J. A. Seman, E. a. L. Henn, R. F. Shiozaki, G. Roati, F. J. Poveda-Cuevas, K. M. F. Magalhães, V. I. Yukalov, M. Tsubota, M. Kobayashi, K. Kasamatsu, and V. S. Bagnato. *Route to turbulence in a trapped Bose-Einstein condensate*. Laser Physics Letters **8**, 691 (2011). ISSN 1612-202X. DOI: 10.1002/lapl.201110052. [p 4]

[77] M. Abad, A. Recati, S. Stringari, and F. Chevy. *Counter-flow instability of a quantum mixture of two superfluids*. The European Physical Journal D **69**, 126 (2015). ISSN 1434-6079. DOI: 10.1140/epjd/e2015-50851-y. [pp 4, 83, 96, and 100]

[78] S. Ishino, H. Takeuchi, and M. Tsubota. *Counterflow Quantum Turbulence and the Instability in Two-component Bose-Einstein Condensates*. Journal of Low Temperature Physics **162**, 361 (2011). ISSN 1573-7357. DOI: 10.1007/s10909-010-0324-y. [pp 4, 83, 96, and 100]

[79] N. Suzuki, H. Takeuchi, K. Kasamatsu, M. Tsubota, and H. Saito. *Crossover between Kelvin-Helmholtz and counter-superflow instabilities in two-component Bose-Einstein condensates*. Physical Review A **82**, 063604 (2010). DOI: 10.1103/PhysRevA.82.063604. [pp 4, 83, 96, and 100]

[80] A. White, T. Hennessy, and T. Busch. *Emergence of classical rotation in superfluid Bose-Einstein condensates*. Physical Review A **93**, 033601 (2016). DOI: 10.1103/PhysRevA.93.033601. [pp 4, 83, 96, and 100]

[81] D. Kobyakov, V. Bychkov, E. Lundh, A. Bezett, and M. Marklund. *Parametric resonance of capillary waves at the interface between two immiscible Bose-Einstein condensates*. Physical Review A **86**, 023614 (2012). DOI: 10.1103/PhysRevA.86.023614. [pp 4, 96, and 100]

[82] B. P. Anderson, P. C. Haljan, C. A. Regal, D. L. Feder, L. A. Collins, C. W. Clark, and E. A. Cornell. *Watching Dark Solitons Decay into Vortex Rings in a Bose-Einstein Condensate*. Physical Review Letters **86**, 2926 (2001). DOI: 10.1103/PhysRevLett.86.2926. [pp 4, 83]

[83] J. Tomkovič, W. Muessel, H. Strobel, S. Löck, P. Schlagheck, R. Ketzmerick, and M. K. Oberthaler. *Experimental observation of the Poincare-Birkhoff scenario in a driven many-body quantum system*. Physical Review A **95**, 011602 (2017). DOI: 10.1103/PhysRevA.95.011602. [pp 4, 83]

[84] T. Kaneda and H. Saito. *Collision dynamics of skyrmions in a two-component Bose-Einstein condensate*. Physical Review A **93**, 033611 (2016). DOI: 10.1103/PhysRevA.93.033611. [pp 4, 96, and 100]

[85] C. J. Foot. *Atomic Physics*. Oxford Master Series in Physics. Oxford University Press, Oxford, New York (2004). ISBN 978-0-19-850696-6. [p 9]

[86] D. Budker, D. Kimball, and D. DeMille. *Atomic Physics: An Exploration through Problems and Solutions*. Oxford University Press, Oxford ; New York, 2 edition edition (2008). ISBN 978-0-19-953241-4. [pp 9, 18]

[87] R. Grimm, M. Weidemüller, and Y. B. Ovchinnikov. *Optical Dipole Traps for Neutral Atoms*. In B. Bederson and H. Walther, eds., *Advances In Atomic, Molecular, and Optical Physics*, volume 42, pages 95–170. Academic Press (2000). DOI: 10.1016/S1049-250X(08)60186-X. [pp 14, 55]

[88] J. Durnin. *Exact solutions for nondiffracting beams. I. The scalar theory*. JOSA A **4**, 651 (1987). ISSN 1520-8532. DOI: 10.1364/JOSAA.4.000651. [p 17]

[89] D. McGloin and K. Dholakia. *Bessel beams: Diffraction in a new light* (2005). DOI: 10.1080/0010751042000275259. [pp 18, 59]

[90] A. E. Siegman. *Lasers*. University Science Books (1986). ISBN 978-0-935702-11-8. [pp 19, 47]

[91] M. R. Andrews, M.-O. Mewes, N. J. van Druten, D. S. Durfee, D. M. Kurn, and W. Ketterle. *Direct, Nondestructive Observation of a Bose Condensate*. Science **273**, 84 (1996). ISSN 0036-8075, 1095-9203. DOI: 10.1126/science.273.5271.84. [p 20]

[92] A. Reinhard, J.-F. Riou, L. A. Zundel, and D. S. Weiss. *Dark-ground imaging of high optical thickness atom clouds*. Optics Communications **324**, 30 (2014). ISSN 0030-4018. DOI: 10.1016/j.optcom.2014.02.070. [p 20]

[93] M. Pappa, P. C. Condylis, G. O. Konstantinidis, V. Bolpasi, A. Lazoudis, O. Morizot, D. Sahagun, M. Baker, and W. von Klitzing. *Ultra-sensitive atom imaging for matter-wave optics*. New Journal of Physics **13**, 115012 (2011). ISSN 1367-2630. DOI: 10.1088/1367-2630/13/11/115012. [p 20]

[94] R. Meppelink, R. A. Rozendaal, S. B. Koller, J. M. Vogels, and P. van der Straten. *Thermodynamics of Bose-Einstein-condensed clouds using phase-contrast imaging*. Physical Review A **81**, 053632 (2010). DOI: 10.1103/PhysRevA.81.053632. [p 20]

[95] M. R. Andrews, D. M. Kurn, H.-J. Miesner, D. S. Durfee, C. G. Townsend, S. Inouye, and W. Ketterle. *Propagation of Sound in a Bose-Einstein Condensate*. Physical Review Letters **79**, 553 (1997). DOI: 10.1103/PhysRevLett.79.553. [p 20]

[96] C. C. Bradley, C. A. Sackett, and R. G. Hulet. *Bose-Einstein Condensation of Lithium: Observation of Limited Condensate Number*. Physical Review Letters **78**, 985 (1997). DOI: 10.1103/PhysRevLett.78.985. [p 21]

[97] F. Kaminski, N. S. Kampel, M. P. H. Steenstrup, A. Griesmaier, E. S. Polzik, and J. H. Müller. *In-situ dual-port polarization contrast imaging of Faraday rotation in a high optical depth ultracold 87Rb atomic ensemble*. The European Physical Journal D **66**, 227 (2012). ISSN 1434-6079. DOI: 10.1140/epjd/e2012-30038-0. [p 21]

[98] M. Gajdacz, P. L. Pedersen, T. Mørch, A. J. Hilliard, J. Arlt, and J. F. Sherson. *Non-destructive Faraday imaging of dynamically controlled ultracold atoms*. Review of Scientific Instruments **84**, 083105 (2013). ISSN 0034-6748. DOI: 10.1063/1.4818913. [p 21]

[99] J. Smits, A. Mosk, and P. van der Straten. *Imaging trapped quantum gases by off-axis holography*. Optics Letters (2020). ISSN 1539-4794. DOI: 10.1364/OL.384120. [p 21]

[100] G. S. Settles. *Smartphone schlieren and shadowgraph imaging*. Optics and Lasers in Engineering **104**, 9 (2018). ISSN 0143-8166. DOI: 10.1016/j.optlaseng.2017.07.002. [p 21]

[101] P. B. Wigley, P. J. Everitt, K. S. Hardman, M. R. Hush, C. H. Wei, M. A. Sooriyabandara, P. Manju, J. D. Close, N. P. Robins, and C. C. N. Kuhn. *Non-destructive shadowgraph imaging of ultra-cold atoms*. Optics Letters **41**, 4795 (2016). ISSN 1539-4794. DOI: 10.1364/OL.41.004795. [pp 21, 45, 71, and 87]

[102] D. A. Steck. *Alkali D Line Data*. https://steck.us/alkalidata/ (2019). [pp 22, 54]

[103] F. Dalfovo, S. Giorgini, L. P. Pitaevskii, and S. Stringari. *Theory of Bose-Einstein condensation in trapped gases*. Reviews of Modern Physics **71**, 463 (1999). DOI: 10.1103/RevModPhys.71.463. [pp 26, 27, and 57]

[104] K. Enomoto, K. Kasa, M. Kitagawa, and Y. Takahashi. *Optical Feshbach Resonance Using the Intercombination Transition*. Physical Review Letters **101**, 203201 (2008). DOI: 10.1103/PhysRevLett.101.203201. [p 27]

[105] M. Theis, G. Thalhammer, K. Winkler, M. Hellwig, G. Ruff, R. Grimm, and J. H. Denschlag. *Tuning the Scattering Length with an Optically Induced Feshbach Resonance*. Physical Review Letters **93**, 123001 (2004). DOI: 10.1103/PhysRevLett.93.123001. [p 27]

[106] N. Claussen, S. Kokkelmans, S. Thompson, E. Donley, E. Hodby, and C. Wieman. *Very-high-precision bound-state spectroscopy near a 85Rb Feshbach resonance*. Physical Review A **67** (2003). DOI: 10.1103/PhysRevA.67.060701. [p 27]

[107] V. M. Pérez-García, H. Michinel, J. I. Cirac, M. Lewenstein, and P. Zoller. *Low Energy Excitations of a Bose-Einstein Condensate: A Time-Dependent Variational Analysis*. Physical Review Letters **77**, 5320 (1996). DOI: 10.1103/PhysRevLett.77.5320. [p 27]

[108] H. Al-Jibbouri, I. Vidanović, A. Balaž, and A. Pelster. *Geometric resonances in Bose–Einstein condensates with two- and three-body interactions*. Journal of Physics B: Atomic, Molecular and Optical Physics **46**, 065303 (2013). ISSN 0953-4075. DOI: 10.1088/0953-4075/46/6/065303. [p 27]

[109] S. Stringari. *Collective Excitations of a Trapped Bose-Condensed Gas*. Physical Review Letters **77**, 2360 (1996). DOI: 10.1103/PhysRevLett.77.2360. [pp 27, 28, and 29]

[110] R. Dubessy, C. D. Rossi, T. Badr, L. Longchambon, and H. Perrin. *Imaging the collective excitations of an ultracold gas using statistical correlations*. New Journal of Physics **16**, 122001 (2014). ISSN 1367-2630. DOI: 10.1088/1367-2630/16/12/122001. [pp 30, 57]

[111] L. D. Carr and Y. Castin. *Dynamics of a matter-wave bright soliton in an expulsive potential*. Physical Review A **66**, 063602 (2002). DOI: 10.1103/PhysRevA.66.063602. [pp 31, 73, and 79]

[112] G. P. Agrawal. *Nonlinear Fiber Optics*. In P. L. Christiansen, M. P. Sorensen, and A. C. Scott, eds., *Nonlinear Science at the Dawn of the 21st Century*, Lecture Notes in Physics, pages 195–211. Springer, Berlin, Heidelberg (2000). ISBN 978-3-540-46629-1. [p 33]

[113] R. Anderson. *Nonequilibrium dynamics and relative phase evolution of two-component Bose-Einstein condensates*. Ph.D. thesis, Swinburne University of Technology (2010). [p 34]

[114] P. A. Altin. *The role of interactions in interferometry with Bose-condesned atoms*. PhD, Australian National University (2012). [pp 35, 39, 52, 57, and 85]

[115] C. C. N. Kuhn, G. D. McDonald, K. S. Hardman, S. Bennetts, P. J. Everitt, P. A. Altin, J. E. Debs, J. D. Close, and N. P. Robins. *A Bose-condensed, simultaneous dual-species Mach–Zehnder atom interferometer*. New Journal of Physics **16**, 073035 (2014). ISSN 1367-2630. DOI: 10.1088/1367-2630/16/7/073035. [pp 39, 40, 61, 64, 65, 70, 99, and 100]

[116] G. McDonald. *Cold atom interferometry in optical potentials*. Ph.D. thesis (2015). [pp 39, 61]

[117] S. Riedl, M. Lettner, C. Vo, S. Baur, G. Rempe, and S. Dürr. *Bose-Einstein condensate as a quantum memory for a photonic polarization qubit*. Physical Review A **85**, 022318 (2012). DOI: 10.1103/PhysRevA.85.022318. [pp 41, 100]

[118] M. Lettner, M. Mücke, S. Riedl, C. Vo, C. Hahn, S. Baur, J. Bochmann, S. Ritter, S. Dürr, and G. Rempe. *Remote Entanglement between a Single Atom and a Bose-Einstein Condensate*. Physical Review Letters **106**, 210503 (2011). DOI: 10.1103/PhysRevLett.106.210503. [pp 41, 100]

[119] R. Zhang, S. R. Garner, and L. V. Hau. *Creation of Long-Term Coherent Optical Memory via Controlled Nonlinear Interactions in Bose-Einstein Condensates*. Physical Review Letters **103**, 233602 (2009). DOI: 10.1103/PhysRevLett.103.233602. [pp 41, 100]

[120] *Cateye Diode Laser*. https://www.moglabs.com/cel. [p 41]

[121] *OpticStudio Homepage - Zemax*. https://www.zemax.com/products/opticstudio. [p 45]

[122] G. McDonald, C. C. N. Kuhn, K. S. Hardman, S. Bennetts, P. J. Everitt, P. A. Altin, J. E. Debs, J. D. Close, and N. P. Robins. *Bright Solitonic Matter-Wave Interferometer*. Physical Review Letters **113** (2014). [pp 47, 65, 70, 82, 83, 85, and 100]

[123] R. Thomas and N. Kjærgaard. *A digital feedback controller for stabilizing large electric currents to the ppm level for Feshbach resonance studies*. Review of Scientific Instruments **91**, 034705 (2020). ISSN 0034-6748. DOI: 10.1063/1.5128935. [p 49]

[124] *Alan - BEC Coil Driver*. https://www.physics.utoronto.ca/~astummer/Archives/2004%20BEC%20Coil%20Driver%20%27Mag-O-Matic%27/BEC_coils.html. [p 49]

[125] C. J. Dedman, R. G. Dall, L. J. Byron, and A. G. Truscott. *Active cancellation of stray magnetic fields in a Bose-Einstein condensation experiment*. Review of Scientific Instruments **78**, 024703 (2007). ISSN 0034-6748. DOI: 10.1063/1.2472600. [p 52]

[126] K. S. Hardman. *A BEC Based Precision Gravimeter and Magnetic Gradiometer: Design and Implementation* (2016). DOI: 10.25911/5d723b873573a. [p 61]

[127] Y.-J. Lin, A. R. Perry, R. L. Compton, I. B. Spielman, and J. V. Porto. *Rapid production of ^{87} Rb Bose-Einstein condensates in a combined magnetic and optical potential*. Physical Review A **79**, 063631 (2009). DOI: 10.1103/PhysRevA.79.063631. [p 62]

[128] P. A. Altin, G. R. Dennis, G. D. McDonald, D. Döring, J. E. Debs, J. D. Close, C. M. Savage, and N. P. Robins. *Collapse and three-body loss in a ^{85} Rb Bose-Einstein condensate*. Physical Review A **84**, 033632 (2011). DOI: 10.1103/PhysRevA.84.033632. [pp 63, 90]

[129] P. Manju, K. S. Hardman, M. A. Sooriyabandara, P. B. Wigley, J. D. Close, N. P. Robins, M. R. Hush, and S. S. Szigeti. *Quantum tunneling dynamics of an interacting Bose-Einstein condensate through a Gaussian barrier*. Physical Review A **98**, 053629 (2018). DOI: 10.1103/PhysRevA.98.053629. [pp 65, 100]

[130] S. L. Cornish, S. T. Thompson, and C. E. Wieman. *Formation of Bright Matter-Wave Solitons during the Collapse of Attractive Bose-Einstein Condensates*. Physical Review Letters **96**, 170401 (2006). DOI: 10.1103/PhysRevLett.96.170401. [p 70]

[131] L. Salasnich, A. Parola, and L. Reatto. *Modulational Instability and Complex Dynamics of Confined Matter-Wave Solitons*. Physical Review Letters **91**, 080405 (2003). ISSN 0031-9007, 1079-7114. DOI: 10.1103/PhysRevLett.91.080405. [pp 70, 75]

[132] L. D. Carr and J. Brand. *Spontaneous Soliton Formation and Modulational Instability in Bose-Einstein Condensates*. Physical Review Letters **92**, 040401 (2004). ISSN 0031-9007, 1079-7114. DOI: 10.1103/PhysRevLett.92.040401. [p 70]

[133] L. Salasnich, A. Parola, and L. Reatto. *Effective wave equations for the dynamics of cigar-shaped and disk-shaped Bose condensates*. Physical Review A **65**, 043614 (2002). ISSN 1050-2947, 1094-1622. DOI: 10.1103/PhysRevA.65.043614. [pp 70, 75, and 76]

[134] C. Wei, S. Yan, A. Jia, Y. Luo, Q. Hu, and Z. Li. *Compact phase-lock loop for external cavity diode lasers*. Chinese Optics Letters **14**, 051403 (2016). [p 72]

[135] D. S. Petrov, G. V. Shlyapnikov, and J. T. M. Walraven. *Regimes of Quantum Degeneracy in Trapped 1D Gases*. Physical Review Letters **85**, 3745 (2000). DOI: 10.1103/PhysRevLett.85.3745. [p 73]

[136] J. M. Dudley, G. Genty, and S. Coen. *Supercontinuum generation in photonic crystal fiber*. Reviews of Modern Physics **78**, 1135 (2006). DOI: 10.1103/RevModPhys.78.1135. [pp 76, 78]

[137] L. S. Cederbaum, A. I. Streltsov, and O. E. Alon. *Fragmented Metastable States Exist in an Attractive Bose-Einstein Condensate for Atom Numbers Well above the Critical Number of the Gross-Pitaevskii Theory*. Physical Review Letters **100**, 040402 (2008). DOI: 10.1103/PhysRevLett.100.040402. [p 81]

[138] J. H. V. Nguyen, P. Dyke, D. Luo, B. A. Malomed, and R. G. Hulet. *Collisions of matter-wave solitons*. Nature Physics **10**, 918 (2014). ISSN 1745-2473. DOI: 10.1038/nphys3135. [p 82]

[139] P. Engels, C. Atherton, and M. A. Hoefer. *Observation of Faraday Waves in a Bose-Einstein Condensate*. Physical Review Letters **98**, 095301 (2007). DOI: 10.1103/PhysRevLett.98.095301. [p 83]

[140] K. W. Madison, F. Chevy, W. Wohlleben, and J. Dalibard. *Vortex Formation in a Stirred Bose-Einstein Condensate*. Physical Review Letters **84**, 806 (2000). DOI: 10.1103/PhysRevLett.84.806. [p 83]

[141] H. Strobel, W. Muessel, D. Linnemann, T. Zibold, D. B. Hume, L. Pezzè, A. Smerzi, and M. K. Oberthaler. *Fisher information and entanglement of non-Gaussian spin states*. Science **345**, 424 (2014). ISSN 0036-8075, 1095-9203. DOI: 10.1126/science.1250147. [p 83]

[142] L. Pezzè, A. Smerzi, M. K. Oberthaler, R. Schmied, and P. Treutlein. *Quantum metrology with nonclassical states of atomic ensembles*. Reviews of Modern Physics **90**, 035005 (2018). DOI: 10.1103/RevModPhys.90.035005. [p 83]

[143] C. Sabín, A. White, L. Hackermuller, and I. Fuentes. *Impurities as a quantum thermometer for a Bose-Einstein condensate*. Scientific Reports **4**, 6436 (2014). ISSN 2045-2322. DOI: 10.1038/srep06436. [p 84]

[144] S. B. Papp, J. M. Pino, and C. E. Wieman. *Tunable Miscibility in a Dual-Species Bose-Einstein Condensate*. Physical Review Letters **101**, 040402 (2008). DOI: 10.1103/PhysRevLett.101.040402. [pp 84, 85, and 90]

[145] P. Mason. *Ground states of two-component condensates in a harmonic plus Gaussian trap*. The European Physical Journal B **86**, 453 (2013). ISSN 1434-6036. DOI: 10.1140/epjb/e2013-40665-2. [p 85]

[146] G. Thalhammer, G. Barontini, L. De Sarlo, J. Catani, F. Minardi, and M. Inguscio. *Double Species Bose-Einstein Condensate with Tunable Interspecies Interactions*. Physical Review Letters **100**, 210402 (2008). DOI: 10.1103/PhysRevLett.100.210402. [p 85]

[147] D. J. McCarron, H. W. Cho, D. L. Jenkin, M. P. Köppinger, and S. L. Cornish. *Dual-species Bose-Einstein condensate of ^{87}Rb and ^{133}Cs*. Physical Review A **84**, 011603 (2011). DOI: 10.1103/PhysRevA.84.011603. [p 85]

[148] A. D. Lercher, T. Takekoshi, M. Debatin, B. Schuster, R. Rameshan, F. Ferlaino, R. Grimm, and H. C. Nägerl. *Production of a dual-species Bose-Einstein condensate of Rb and Cs atoms*. The European Physical Journal D **65**, 3 (2011). ISSN 1434-6079. DOI: 10.1140/epjd/e2011-20015-6. [p 85]

[149] S. Sugawa, R. Yamazaki, S. Taie, and Y. Takahashi. *Bose-Einstein condensate in gases of rare atomic species*. Physical Review A **84**, 011610 (2011). DOI: 10.1103/PhysRevA.84.011610. [p 85]

[150] B. Pasquiou, A. Bayerle, S. M. Tzanova, S. Stellmer, J. Szczepkowski, M. Parigger, R. Grimm, and F. Schreck. *Quantum degenerate mixtures of strontium and rubidium atoms*. Physical Review A **88**, 023601 (2013). DOI: 10.1103/PhysRevA.88.023601. [p 85]

[151] G. K. Walters and W. M. Fairbank. *Phase Separation in ^{3} He— ^{4}He Solutions*. Physical Review **103**, 262 (1956). DOI: 10.1103/PhysRev.103.262.2. [p 85]

[152] F. Wang, X. Li, D. Xiong, and D. Wang. *A double species ^{23}Na and ^{87}Rb Bose–Einstein condensate with tunable miscibility via an interspecies Feshbach resonance*. Journal of Physics B: Atomic, Molecular and Optical Physics **49**, 015302 (2015). ISSN 0953-4075. DOI: 10.1088/0953-4075/49/1/015302. [p 85]

[153] K. L. Lee, N. B. Jørgensen, L. J. Wacker, M. G. Skou, K. T. Skalmstang, J. J. Arlt, and N. P. Proukakis. *Time-of-flight expansion of binary Bose–Einstein condensates at finite temperature*. New Journal of Physics **20**, 053004 (2018). ISSN 1367-2630. DOI: 10.1088/1367-2630/aaba39. [pp 85, 89, and 92]

[154] S. Ospelkaus, C. Ospelkaus, L. Humbert, K. Sengstock, and K. Bongs. *Tuning of Heteronuclear Interactions in a Degenerate Fermi-Bose Mixture*. Physical Review Letters **97**, 120403 (2006). DOI: 10.1103/PhysRevLett.97.120403. [p 85]

[155] R. W. Pattinson, T. P. Billam, S. A. Gardiner, D. J. McCarron, H. W. Cho, S. L. Cornish, N. G. Parker, and N. P. Proukakis. *Equilibrium solutions for immiscible two-species Bose-Einstein condensates in perturbed harmonic traps*. Physical Review A **87**, 013625 (2013). DOI: 10.1103/PhysRevA.87.013625. [p 85]

[156] A. Burchianti, C. D'Errico, S. Rosi, A. Simoni, M. Modugno, C. Fort, and F. Minardi. *Dual-species Bose-Einstein condensate of ^{41} K and ^{87} Rb in a hybrid trap*. Physical Review A **98**, 063616 (2018). DOI: 10.1103/PhysRevA.98.063616. [p 85]

[157] K. L. Lee, N. B. Jørgensen, I.-K. Liu, L. Wacker, J. J. Arlt, and N. P. Proukakis. *Phase separation and dynamics of two-component Bose-Einstein condensates*. Physical Review A **94**, 013602 (2016). DOI: 10.1103/PhysRevA.94.013602. [p 85]

[158] M. L. Chiofalo, S. Succi, and M. P. Tosi. *Ground state of trapped interacting Bose-Einstein condensates by an explicit imaginary-time algorithm*. Physical Review E **62**, 7438 (2000). DOI: 10.1103/PhysRevE.62.7438. [p 89]

[159] W. Bao and Q. Du. *Computing the Ground State Solution of Bose–Einstein Condensates by a Normalized Gradient Flow*. SIAM Journal on Scientific Computing **25**, 1674 (2004). ISSN 1064-8275. DOI: 10.1137/S1064827503422956. [p 89]

[160] G. R. Dennis, J. J. Hope, and M. T. Johnsson. *XMDS2: Fast, scalable simulation of coupled stochastic partial differential equations*. Computer Physics Communications **184**, 201 (2013). ISSN 0010-4655. DOI: 10.1016/j.cpc.2012.08.016. [p 89]

[161] J. P. Burke and J. L. Bohn. *Ultracold scattering properties of the short-lived Rb isotopes*. Physical Review A **59**, 1303 (1999). DOI: 10.1103/PhysRevA.59.1303. [p 90]

[162] K. Sasaki, N. Suzuki, and H. Saito. *Capillary instability in a two-component Bose-Einstein condensate*. Physical Review A **83**, 053606 (2011). DOI: 10.1103/PhysRevA.83.053606. [pp 96, 100]

[163] B. Van Schaeybroeck and J. O. Indekeu. *Critical wetting, first-order wetting, and prewetting phase transitions in binary mixtures of Bose-Einstein condensates*. Physical Review A **91**, 013626 (2015). DOI: 10.1103/PhysRevA.91.013626. [pp 97, 100]

[164] K. O. Roberts, T. McKellar, J. Fekete, A. Rakonjac, A. B. Deb, and N. Kjærgaard. *Steerable optical tweezers for ultracold atom studies*. Optics Letters **39**, 2012 (2014). ISSN 1539-4794. DOI: 10.1364/OL.39.002012. [p 100]

[165] T. A. Haase, D. H. White, D. J. Brown, I. Herrera, and M. D. Hoogerland. *A versatile apparatus for two-dimensional atomtronic quantum simulation*. Review of Scientific Instruments **88**, 113102 (2017). ISSN 0034-6748. DOI: 10.1063/1.5009584. [p 100]

[166] A. Kuzmich, N. P. Bigelow, and L. Mandel. *Atomic quantum non-demolition measurements and squeezing*. EPL (Europhysics Letters) **42**, 481 (1998). ISSN 0295-5075. DOI: 10.1209/epl/i1998-00277-9. [p 100]

[167] S. Hayashi, M. Tsubota, and H. Takeuchi. *Instability crossover of helical shear flow in segregated Bose-Einstein condensates*. Physical Review A **87**, 063628 (2013). DOI: 10.1103/PhysRevA.87.063628. [p 100]

[168] R. R. Malendevich, H. Fang, R. Schiek, and G. I. Stegeman. *Experiments on Seeded and Noise Initiated Modulational Instability in LiNbO3 Slab Waveguides*. In A. D. Boardman and A. P. Sukhorukov, eds., *Soliton-Driven Photonics*, NATO Science Series, pages 219–222. Springer Netherlands, Dordrecht (2001). ISBN 978-94-010-0682-8. [p 100]

[169] M. Nesrallah, A. Hakami, G. Bart, C. R. McDonald, C. Varin, and T. Brabec. *Measuring the Kerr nonlinearity via seeded Kerr instability amplification: Conceptual analysis*. Optics Express **26**, 7646 (2018). ISSN 1094-4087. DOI: 10.1364/OE.26.007646. [p 100]

[170] P. B. Wigley, K. S. Hardman, C. Freier, P. J. Everitt, S. Legge, P. Manju, J. D. Close, and N. P. Robins. *Readout-delay-free Bragg atom interferometry using overlapped spatial fringes*. Physical Review A **99**, 023615 (2019). DOI: 10.1103/PhysRevA.99.023615. [p 100]